USING LIGHT TO CONTROL AND INVESTIGATE CELL BIOLOGY

BY

JOHN S. KHAMO

DISSERTATION

Submitted in partial fulfillment of the requirements
for the degree of Doctor of Philosophy in Biochemistry
in the Graduate College of the
University of Illinois at Urbana-Champaign, 2019

Urbana, Illinois

Doctoral Committee:

Assistant Professor Kai Zhang, Chair
Assistant Professor Erik Procko
Professor David J. Shapiro
Professor Jing Yang

ABSTRACT

It is no surprise that light plays an important role in life. With the development of modern technologies, light has also proven to be a powerful tool for the interrogation of molecular and cellular biology. Beyond its use in microscopic applications, light has emerged as an attractive modulator of cellular function. Within the last two decades, scientists have begun to harness the power of light and light-sensitive moieties to synthetically alter molecular processes in living cells. In combination with more conventional experimental techniques, this approach has allowed for the precise elucidation of many biological mechanisms that underpin development and disease. Here, I report on recent advances in optobiological techniques and their application in cell biology. I also include a novel study on the optogenetic delineation of growth factor signaling in neuronal development. Finally, I report on the spectroscopic analysis of fluorescent nanoparticles with potential biological utility.

ACKNOWLEDGEMENTS

I would like to offer my deepest appreciation to Dr. Kai Zhang, my mentor and friend. Your leadership is exemplary and inspirational. It was an honor and privilege to establish the Zhang lab with you. I would also like to thank the Zhang lab members for helping to create a collegial and productive learning environment, which has enriched my development as a scientist and educator. Additionally, I would like to thank Dr. Keith Westcott and the Department of Biochemistry for financial support throughout my graduate education.

To Mom and Uncle Al.

Thank you for your unconditional and unwavering support.

TABLE OF CONTENTS

CHAPTER 1: APPLICATIONS OF OPTOBIOLOGY IN INTACT CELLS AND MULTI-CELLULAR ORGANISMS

This work contains previously published material.[*]

Abstract

Temporal kinetics and spatial coordination of signal transduction in cells are vital for cell fate determination. Tools that allow for precise modulation of spatiotemporal regulation of intracellular signaling in intact cells and multicellular organisms remain limited. The emerging optobiological approaches use light to control protein-protein interaction in live cells and multicellular organisms. Optobiology empowers light-mediated control of diverse cellular and organismal functions such as neuronal activity, intracellular signaling, gene expression, cell proliferation, differentiation, migration, and apoptosis. In this review, we highlight recent developments in optobiology, focusing on new features of second-generation optobiological tools. We cover applications of optobiological approaches in the study of cellular and organismal functions, discuss current challenges, and present our outlook. Taking advantage of the high spatial and temporal resolution of light control, optobiology promises to provide new insights into the coordination of signaling circuits in intact cells and multicellular organisms.

[*] **Khamo, J.S.** et al. (2017). Applications of Optobiology in Intact Cells and Multicellular Organisms. J Mol Biol 429, 2999-3017. Reference 200.

Introduction

Spatiotemporal coordination of gene expression and signal transduction during developmental processes

Despite the variety of cellular processes occurring during embryonic development, only a handful of signaling pathways, namely the Notch, Wnt/β-catenin, Sonic Hedgehog (SHH), transforming growth factor β (TGFβ), bone morphogenetic protein (BMP), and fibroblast growth factor (FGF) signaling pathways, are repeatedly used to regulate early embryonic development and differentiation [1]. How can a limited number of signaling pathways regulate such diverse cell behavior? Mounting evidence suggests that spatial and temporal regulation of these signaling pathways is crucial to cell fate determination during development. The same pathways can be turned on or off at different times and locations to regulate distinct cell functions.

Circadian oscillators play a critical role in coordinating temporal kinetics of gene expression and signal transduction, responding to signals with a periodicity of 10-24 h. In contrast, oscillation with a shorter periodicity, referred to as ultradian oscillation, determines many biological events at shorter timescales [2]. Temporal coordination of ultradian oscillation often correlates with the formation of spatial patterns of tissue structures during development. For instance, cyclical activation of the Notch pathway is crucial for the formation of a "salt and pepper" pattern of ciliated cells during ciliogenesis [3]. Similarly, oscillation of Notch activation is required for the formation of somites, the precursors to a variety of segmental structures such as the peripheral spinal nerves, vertebrae, axial muscles and early blood vessels [4,5]. The period of the ultradian oscillations in somitogenesis varies from 20 min in zebrafish to 4-6 hours in humans [6]. Besides oscillation, variations in the duration of signals can also lead to distinct cell fates. For instance, transient and sustained activation of the extracellular signal-regulated kinase

(ERK) pathway leads to PC12 cell proliferation and differentiation, respectively [7,8]. In pairs of genetically identical MCF-10A sister cells treated with EGF, cells entering S phase experience sustained ERK activity, whereas the lagging sister cells exhibit pulsatile ERK activity [9]. In cultured rat hippocampal neurons, acute delivery of brain-derived neurotrophic factor (BDNF) elicits transient TrkB signaling and promotes neurite elongation, whereas gradual delivery of BDNF elicits sustained TrkB signaling and promotes neurite branching [10]. Interestingly, high-frequency neuronal stimulation can convert a transient BDNF-TrkB activity into a sustained one [11]. Thus, spatiotemporal coordination of gene expression and signal transduction provides a fundamental molecular mechanism to regulate cell fates.

Both biochemical feedback and molecular stability influence signal oscillation and duration. For instance, negative feedback between the Hes1 protein and its mRNA leads to oscillatory or sustained Hes1 protein expression, resulting in the proliferation and differentiation of neural progenitor cells, respectively [12,13]. Negative feedback loops in the mitogen-activated protein kinase pathway can lead to sustained oscillation in kinase activity [14-16]. In the case of molecular stability, an increase in the half-life of *Hes1* mRNA leads to an extension of the Hes1 protein oscillation period [17]. Unraveling such intricate signaling mechanisms demands tools to probe these dynamic regulatory processes with spatiotemporal precision.

Challenges in spatiotemporal control of signal transduction and gene expression

Our current understanding of gene expression and signaling mechanisms has primarily relied on conventional genetic and pharmacological approaches. Commonly used genetic approaches such as gain- and loss-of-function mutagenesis often lead to constitutive activation or inactivation of signaling activity. To address this issue, alternative chemical and genetic tools

have been developed. For instance, several inducible systems are available to activate or repress protein expression in yeast [18]. Chemical regulation of gene expression has been achieved using promoters that respond to molecules such as galactose, methionine, and copper. Alternatively, engineered gene regulatory systems that employ estrogen or doxycycline can be utilized for orthogonal gene transcription control. While these inducible systems have greatly facilitated the control of gene expression, their off-target effects, ineffective delivery, and limited reversibility have restricted their use in live cells and multicellular organisms [19-21]. Moreover, it remains challenging for these conventional approaches to precisely perturb gene expression and signal transduction at a resolution that matches the spatial and temporal scales of endogenous developmental events, which can occur in minutes within space of several microns.

Emerging optobiological approaches

Light can be confined to a sub-micron space and precisely tuned in time, with minimal invasiveness to biological organisms. These advantages initially enabled the interrogation of neuronal firing by light-sensitive synthetic ion channels [22] and channelrhodopsin [23,24] in genetically dissected circuits, which led to the coining of the term "optogenetics" [25]. By modulating neuronal firing, optogenetics has provided a new way to investigate neuronal circuits and to establish causal relationships between brain activity and health and disease [26,27]. These powerful tools not only help researchers in basic science understand signaling circuits in brain functions such as learning and memory, but also show promising preclinical and clinical potential for rewiring neuronal circuits to amplify or override specific neuronal phenotypes. Indeed, optogenetics has been extended to basic and preclinical research on a wide spectrum of topics such as Parkinson's disease [28], sleep [29], cardiac function [30,31], neuropsychiatric diseases [32],

epilepsy [33], and sight-restoring therapy [34,35]. This new modality provided by light has been transforming neuroscience research, as evidenced by its explosive growth in recent years.

The power of light to interrogate cell functions, however, is not limited to the modulation of the membrane potential of excitable cells [36]. Light has also been used to control a variety of signaling processes [37-43]. As pointed out earlier by Lin et al., we believe it is more appropriate to refer to this broader emerging field as optobiology, in which light enables new modalities to study biological processes in intact cells and multicellular organisms, including in situations where genetic dissection is not essential [44]. In optobiology, light not only serves as an observational tool to follow biological events, but also as a manipulative device to modulate activation states of signaling components with high spatial and temporal resolution.

Over the past decade, a portfolio of optobiological tools has emerged to regulate protein-protein interactions in live cells. The core components of optobiology are photoactivatable proteins, which respond to visible or infrared light stimulation by changing their conformations [45]. These light-triggered conformational changes can induce inter- or intra-molecular interactions. When linked to specific signaling components, photoactivatable proteins allow for light-controlled activation or inactivation of target signal transduction. To date, light has been used to control cellular processes such as gene transcription, translation, protein degradation, differentiation, apoptosis, and migration, as discussed in the following sections. Photocaged small molecules or amino acids also enable light-mediated control of cell functions, a process often referred to as photopharmacological or optochemical control.

Recent optobiological work has expanded its host system from cultured cells to multicellular organisms. Compared to cultured cells, multicellular organisms require better quality control in genetic and protein engineering, as well as material and light delivery. In this

review, we outline recent advances in optobiology, focusing primarily on accomplishments made in the past three years. For earlier work, interested readers are encouraged to refer to previous reviews [46-54]. In the following sections, we describe optobiological tools with new photophysical properties, update new optobiological applications in intact cells and multicellular organisms, discuss challenges in optobiology, and present our outlook. Because many reviews have covered optogenetic control of neuronal activity based on channelrhodopsin and their derivatives [55-61], we will not repeat that aspect of optobiology in this work.

New features of second-generation optobiological tools

Optobiology offers a repertoire of light responsive modules. Because the commonly used phytochrome, cryptochrome, and light-oxygen-voltage (LOV) domains have been extensively reviewed [45-49], we only list new members of photoactivatable proteins discovered within the past three years (Table 1). We summarize key characteristics of these proteins, including their sizes and photophysical properties, namely the excitation wavelength, association and dissociation kinetics, and binding affinity. Most of these new members evolved from their first-generation parental proteins. Like their parental proteins, these new photoactivatable proteins alter their intra- or inter-molecular interactions upon light illumination. Their mechanisms of action and new features are depicted in Figure 1.

Table 1: Collection of photoactivatable proteins and their photophysical properties.

Photoactivatable protein	**Parental protein**	**Excitation λ (nm)**	**Size (a.a.)**	**Asso. time**	**Disso. time**	**Kd**	**Ref.**
pdDronpa1 variants[1]	Dronpa K145N	500/400	224	3 s[2]	8 s	4 μM	69
CRY2-CIB1 variants[3]	CRY2wt	450-490	535/81 or 170	ms	2.5-24 min	Not reported	70

Table 1 (cont.)

Photoactivatable protein	Parental protein	Excitation λ (nm)	Size (a.a.)	Asso. time	Disso. time	Kd	Ref.
CRY2E490G	CRY2wt	450-490	498	ms	23.1 min	Not reported	71
CRY2clust	CRY2wt	450-490	507	<1 s	~220 s	Not reported	72
iLID nano & micro	*As*LOV2-SsrA SspB	450-490	149/112	<30 s	<30 s	0.1 - 47.0 µM[4]	63
LOVTRAP	*As*LOV2 Zdk	450-490	146/65	<30 s	1.7-496 s	17 nM – >4 µM[5]	65
Magnets	VVD	450-490	150	1.5 s	6.8 s - 4.7 h	Not reported	68
CBD	CarH	545	200	Not reported	Not reported	Not reported	73
VfAU1-LOV	n/a	470	150	<1 min	625 s	Not reported	67
CPH1S	CPH1	660/720	513	Not reported	Not reported	Not reported	77
BphP1-PpsR2	BphP1 & RpPpsR2	740/636	731/464	3.5-28 s[6]	3-21 s[7] and 170 s[8]	Not reported	75

[1]pdDronpa1: Dronpa M40I V60A E121R V123T K145N N158V; pdDronpa1.2: pdDronpa1 V158I

[2] Kinetics based on fluorescence readout in live cells.

[3] CRY2 535 (a.a. 1-535 of CRY2), tighter light control than CRY2PHR; CIB81 (a.a. 1-81 of CIB1) smaller fragment that retains interaction with CRY2; CRY2(L348F), prolonged dissociation half-life of 24 min; CRY2(W349R), shortened dissociation half-life of 2.5 min.

[4] iLID nano, blue light lit affinity 132 nM, dark affinity 4.7 µM; iLID micro, blue light lit affinity 800 nM, dark affinity 47 µM.

[5] Zdk1 blue light lit affinity > 4 µM, dark affinity 26.2 nM; Zdk2 blue light lit affinity 761 nM, dark affinity 17 nM; Zdk3 blue light lit affinity 537 nM, dark affinity 11.4 nM.

[6] Exact association kinetics depends on the power of 740-nm light. Stronger excitation light reduces the half-time.

[7] Exact dissociation kinetics depends on the power of 636-nm light. Stronger excitation light reduces the half-time.

[8] Values are based on dark-conversion kinetics. Irradiation with 636-nm light restores 80% Pfr absorbance, the rest 20% depends on dark conversion.

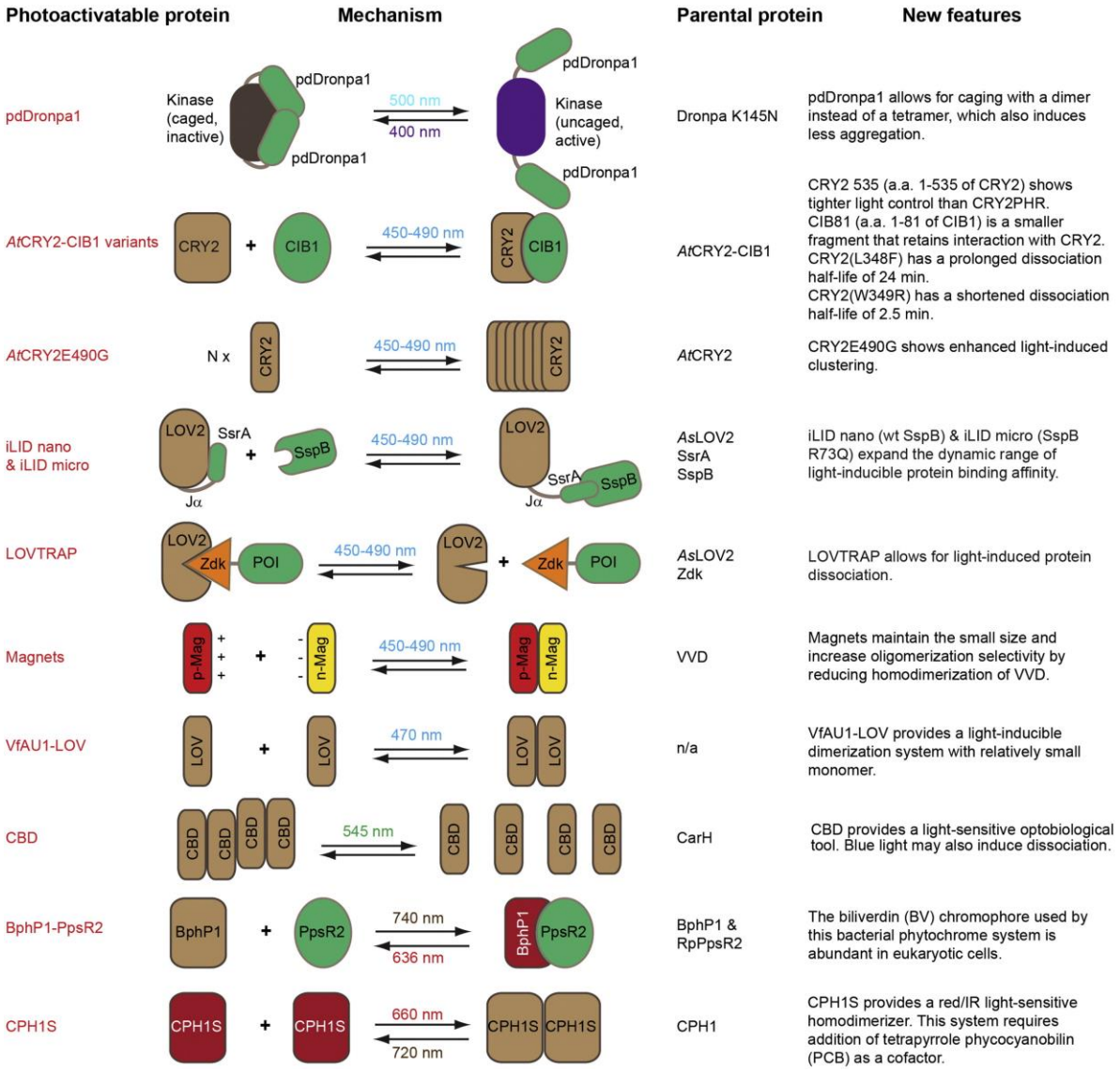

Figure 1. Mechanism of action and new features of various newly developed photoactivatable proteins. Engineered through their parental proteins, these new optobiological tools retain their responses to visible and near IR light stimulation.

New members of LOV-based tools

Avena sativa light-oxygen-voltage 2 (AsLOV2), a photoactivatable protein commonly used in caging a protein of interest, has been engineered to create light-inducible dimerizers, including (1) the tunable light-controlled interacting protein tags (TULIPs) [43] and (2) light-inducible dimers (LIDs). Both utilize the blue light-induced uncaging of a peptide concealed in

the C-terminal Jα helix of AsLOV2. TULIPs consist of a peptide epitope attached to serial truncations of the Jα helix (LOVpep), which binds to an engineered Erbin PDZ domain (ePDZ) upon blue light illumination. Binding affinity between LOVpep and ePDZ can be tuned by AsLOV2 mutants that either increase or decrease helix docking. The original LID (oLID) [62] utilized the similarity between a bacterial peptide, SsrA, and the Jα helix in AsLOV2 to cage SsrA from its binding partner protein, SspB. Blue light-induced conformational changes in AsLOV2 exposed SsrA, which was then free to interact with SspB. The oLID system is limited by a relatively small dynamic range (8-fold change in affinity between lit and dark states) and a high dark-state affinity (800 nM). Guntas et al. sought to improve the dynamic range of LID by phage display screening and found two improved LIDs, iLID nano and iLID micro [63]. Together with TULIPs, iLID nano and micro provide a wide range of lit and dark state affinities to be utilized in specific cellular applications [64].

Another new application of the AsLOV2 is to induce protein *dissociation* by light as opposed to other optogenetic systems, which generally use light to induce protein *association*. Wang et al. developed the LOV2 trap and release of protein system (LOVTRAP) where proteins of interest were fused to a small protein Zdark (Zdk). Zdk was generated by screening a library of amino acid variants of the Z domain from staphylococcal protein A. In the dark state, Zdk domain bound to LOV2 with high affinity, which sequestered the fusion protein to LOV2. Upon blue light illumination, conformational changes in LOV2 promoted their dissociation to release the proteins of interest [65].

The Aureochrome-1 (AUREO1) transcription factor protein from the alga *Vaucheria frigida* consists of a blue-light-sensing LOV domain in its C-terminal region and a central basic region/ leucine zipper (bZIP) domain. Blue light-induced dimerization of monomeric AUREO1

increases its affinity for target DNA and enables its functionality in transcriptional control. The functionality of AUREO1 as a transcriptional switch was proposed to arise from synergistic interactions of its LOV-LOV and bZIP-bZIP domains, which stabilized the monomeric form in the dark and the dimeric form in the lit state [66]. Blue light-induced dimerization of VfAU1-LOV alone, however, is also sufficient to activate fused receptor tyrosine kinases (RTKs) in mammalian cells [67].

The 150-amino-acid vivid (VVD) protein from the filamentous fungus *Neurospora crassa* undergoes homodimerization upon light stimulation. To improve upon its low affinity of homodimerization, slow switch-off kinetics, as well as its selectivity, Kawano et al. developed a series of oppositely charged VVD pairs referred to as "Magnets". Charged residues were introduced in the VVD homodimerization interface comprising residues 47-56. Similar to the attraction between opposite magnetic poles, attraction only occurs between negative-charge-bearing "n-Magnets" and the positive-charge-bearing "p-Magnets", but not between n-n or p-p Magnet pairs. Magnet dissociation times can be tuned by combining different Magnet mutants that have either high affinity or fast dissociation kinetics [68].

Single-chain photodissociable Dronpa (pdDronpa1)

Zhou et al. developed photodissociable dimeric Dronpa domain, pdDronpa1, which can be photoswitched between monomeric and dimeric configurations by cyan and violet light, respectively [69]. Compared with its parental tetrameric protein DronpaK145N, pdDronpa1 utilizes a dimer-to-monomer mechanism to cage/uncage the protein of interest. In addition, pdDronpa1 is less likely to aggregate because the dimer has its valency requirement met by its own intramolecular interaction.

Second-generation tools based on cryptochrome

Cryptochrome 2 (CRY2) and cryptochrome-interacting basic-helix-loop-helix 1 (CIB1) is a heterodimerizing pair that has been widely used in optobiology. The first-generation optogenetic tools utilized either full-length CRY2 or its photolyase homology region (CRY2PHR; 1-498 a.a.) to interact with CIB1 or its N-terminus (CIBN). The system does not require addition of exogenous cofactors, but suffers from a relatively slow dissociation time ($t_{1/2}$ ≈ 5.5 min) [41]. Taslimi et al. sought to generate improved CRY2-CIB1 variants of smaller size, altered interaction lifetimes, and reduced dark-state interactions. A truncated version of CRY2 containing residues 1-535 was identified to possess higher dynamic range and less self-interaction in the dark compared to CRY2PHR. Truncations in CIB1 revealed that only the first 81 residues of CIB1, termed CIB81, was functionally at par with CIBN (170 a.a.) in its capacity to recruit a cytosolic CRY2PHR to the plasma membrane under blue light. By mutating the photocycle-impacting residues in CRY2(535), Taslimi et al. developed two mutants, which had shorter ($t_{1/2}$ ≈ 2.5 min, W349R) and longer ($t_{1/2}$ ≈ 24 min, L348F) dissociation times [70]. In addition, a CRY2 mutant (CRY2olig, E490G) with a stronger oligomerizing potential has been found by the same group [71]. Very recently, Park et al. discovered a short peptide (9 a.a.) which significantly enhanced CRY2PHR clustering when appended to its C-terminus [72]. When compared with other CRY2-based clustering tools, this enhanced reversible clustering tool, named "CRY2clust" exhibited lesser concentration dependence for clustering, higher light sensitivity, faster assembly and disassembly dynamics, and no undesired accumulation in subcellular compartments. Interestingly, the authors report that a 9 a.a. extension of the intrinsic PHR domain in CRY2, CRY2[1-507], also increased the efficiency of light-dependent CRY2 clustering.

Optobiological modules responsive to green light

Optobiological tools that respond to green light have been largely unavailable. Having another excitation wavelength would facilitate multiplexing optobiological applications. Kainrath et al. engineered bacterial cobalamin (vitamin B12) binding domains (CBDs) as a green light-mediated optobiological tool for use in cultured cells and zebrafish [73]. CBD uses a 5'-deoxyadenosylcobalamin (AdoCbl) cofactor, which absorbs green light. In the dark, CBD forms dimers of dimers, which dissociate into monomers under green light irradiation. When fused to the intracellular domain of a membrane-anchored murine fibroblast growth factor receptor mFGFR-MxCBD and expressed in mammalian cells, the construct induced elevated ERK activity, which was then reduced by green light-induced CBD dissociation. Similarly, hyperactive FGFR signaling could also be reduced by green light in zebrafish.

Optobiological modules responsive to red and near infrared light

As we have discussed so far, most optobiological tools are biased towards the blue end of the visible spectrum. Blue light, however, is suboptimal for deep tissue penetration. An attractive photoactivatable protein is phytochrome, which can be switched between the Pfr (absorbing infrared) and Pr (absorbing red light) states using IR and red light. Such a bidirectional control makes phytochrome useful in studying processes with fast association and dissociation kinetics. While *Arabidopsis thaliana* phytochrome B (PhyB)-based systems can outshine blue light-inducible optogenetic systems *in vivo* due to the better tissue penetrance of red light, such systems require the incorporation of an exogenously supplied chromophore, phycocyanobilin (PCB), which severely restricts their use [39]. Nonetheless, Buckley et al. successfully used this system to control subcellular protein localization in zebrafish embryos [74].

The recently discovered *Rhodopseudomonas palustris* bacterial bathy phytochrome, BphP1, has optogenetic properties that are similar to plant phytochromes. More attractively, BphP1 uses a biliverdin (BV) cofactor that can be produced by mammalian cells. Kaberniuk et al. [75] characterized the *in vitro* and *in vivo* interactions between BphP1 and its partner protein PpsR2 and developed an improved optogenetic system which responds to 740 and 636 nm light. This bidirectional control was tapped in a variety of applications ranging from protein translocation to gene transcription *in cellulo* and *in vivo*. To further improve the functionality and dynamic range of the BphP1-PpsR2 pair, Redchuk and colleagues [76] identified a minimal BphP1-interacting Q-PAS1 fragment (17 kD). Combining this system with blue light-activated AsLOV2 uncaging, the authors constructed a dual-color optogenetic system called iRIS (near-infrared-blue-light-inducible shuttle) which exhibited minimal spectral crosstalk. Another homodimerizer based on cyanobacterial phytochrome 1 (CPH1) has also been developed [77]. This system still requires addition of the tetrapyrrole phycocyanobilin (PCB) as a cofactor.

New photo-pharmacological tools

Photo-pharmacological approaches combine the spatiotemporal precision offered by light with the diversity and versatility of chemicals to control cell functions [78-80]. The well-established rapamycin-mediated dimerization of FKBP- and FRB- fusion proteins has been widely used in controlling protein dimerization [81]. A light-controllable rapamycin-FKPB-FRB system was developed by constructing a photocaged analog of rapamycin [82]. Alternatively, Brown et al. utilized a photocleavable dimerized rapamycin (dRap) to form inactive FKBP12-dRap-FKBP12 complexes which could not bind FRB [83]. UV light irradiation cleaved dRap into two functional Rap molecules and enabled the formation of the FKBP12-Rap-FRB complex. Other UV light-

mediated dimerizers include caged abscisic acid (ABA) [84], cTMP-Htag [85], a photoactivatable crosslinker for SNAPTag and HaloTag [86], and gibberellic acid [87].

Aside from photocaged small molecules, photocaged amino acids form another critical group of photopharmacological reagents [46]. Importantly, photocaged unnatural amino acids can be incorporated into any protein in response to an amber codon, UAG, through a protocol pioneered by Peter G. Schultz [88]. To do so, a synthesized pyrrolysyl-tRNA synthetase/tRNA pair was optimized to incorporate a photocaged lysine in response to an amber codon in mammalian cells. This system has been used to control protein localization [89], kinase activity [90], gene expression [91], and CRISPR/Cas9 activity [92]. A similar strategy was used to generate photocaged tyrosine, which was incorporated into the Cre recombinase to achieve light-controllable DNA recombination [93]. Recently, a caged methionine, (S)-N-(4,5-dimethoxy-2-nitrobenzyloxycarbonyl)-methionine, or NVOC-Met, was synthesized through a low-cost, one-step reaction [94]. UVA (365-nm) light illumination removed NVOC to release methionine. Instead of incorporating the photocaged methionine into a protein, the authors used it directly to achieve light-mediated repression of gene expression through a pMET17 promoter.

Optobiological control of cellular functions

Parallel to the development of new photoactivatable proteins, optobiology continues finding new applications in the modulation of cellular and organismal functionality though light-induced uncaging, protein translocation, modulation of concentration and avidity, as well as allosteric control (Figure 2). In this section, we summarize recent advances in optobiological control of cellular functions. We use subcellular locations (plasma membrane, cytoplasm, and

nucleus) to group these cases, highlighting the capacity of light to modulate cellular events with high spatial resolution. We also itemize these findings in Table 2.

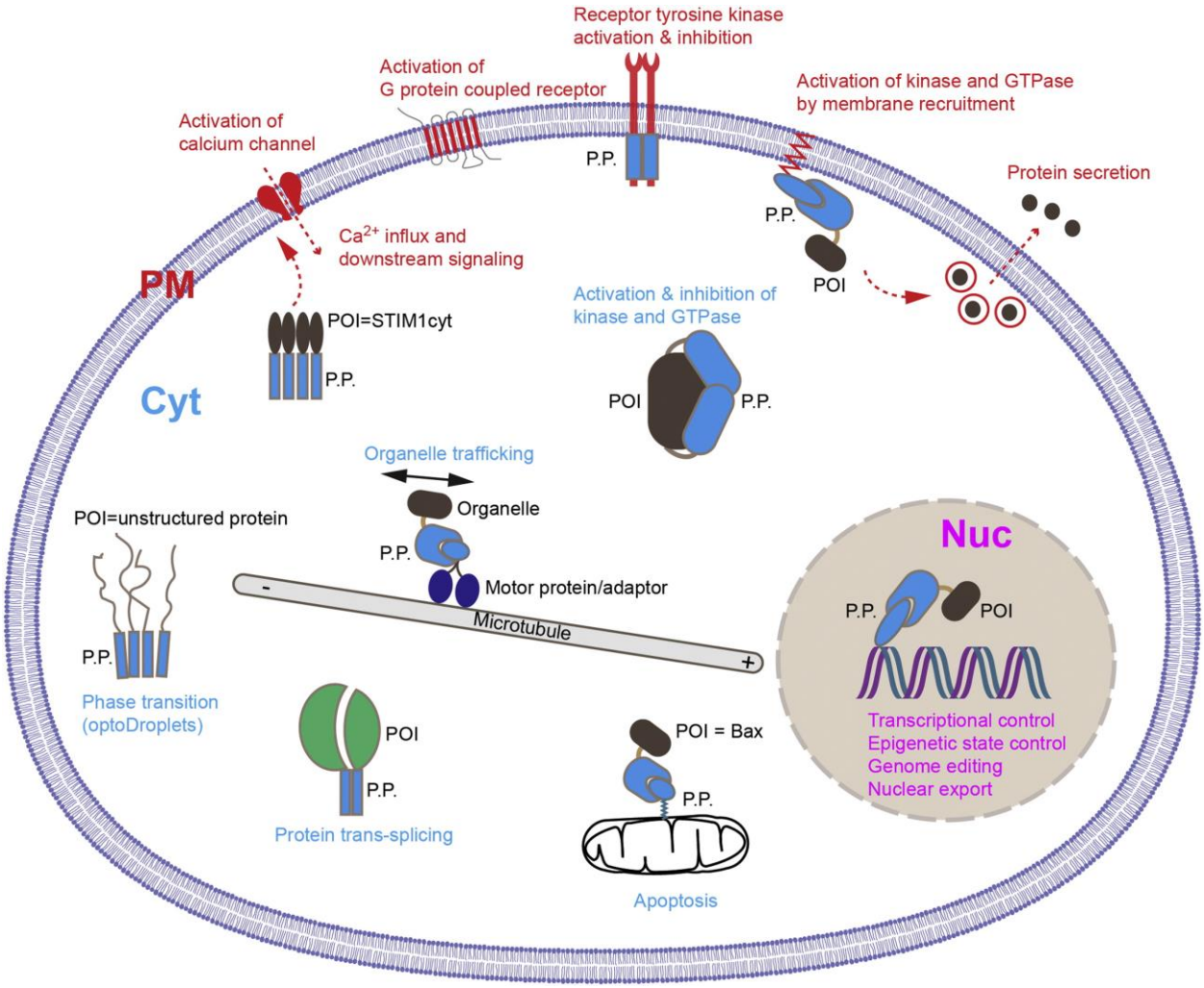

Figure 2. ***Expanded applications of optobiology in intact cells and multicellular organisms***. Optobiology has been utilized to control molecular machinery within distinct subcellular locations such as the nucleus (Nuc), the cytoplasm (Cyt), the plasma membrane (PM). Functionality of protein of interest (POI) can be modulated by light-mediated conformational changes in photoactivatable protein (P.P.).

Table 2: Emerging cellular and organismal functionality controlled by photoactivatable modules.

Site	Function	Module	Target	MOA	Organism	Ref.
PM	Ca^{2+} influx	AsLOV2	STIM1	Caging	Mammalian and hippocampal neurons, *Drosophila* S2 cells, transgenic mice	99
PM	Ca^{2+} influx	AsLOV2	STIM1	Caging	Mammalian cells, mice	100
PM	Ca^{2+} influx	CRY2	STIM1	Association	Mammalian cells zebrafish embryos, mice hippocampi	101
PM	PI(4,5)P2 regulation	CRY2-CIBN	Phosphatase	Association	Mammalian cells	103
PM	Cell contractility, PIP2 depletion	CRY2-CIBN	OCRL	Association	*Drosophila* embryo	105
PM	Phosphoinositide production	Magnets (VVD)	iSH2, Rac1	Association	Mammalian cells	68
PM	Cytoskeletal remodeling	AsLOV2	ITSN, Tiam1	Caging, association	Mammalian cells	63
PM	Membrane protrusion	AsLOV2	GTPase	Caging, association	Mammalian cells	65
PM	Cytokinetic furrowing	LOV-PDZ	LARG	Association	Mammalian cells	110
PM	ERK signaling	AsLOV2	SOS	Caging, association	*Drosophila* embryos	118
PM	Differentiation	CRY2-CIBN	Raf1	Association	Mammalian cells, *Xenopus* embryos	116
PM	GSV membrane translocation	CRY2-CIBN	PI3K, Akt	Association	3T3-L1 adipocytes	122
PM	RTK signaling	CRY2	SH2 of PLCγ	Association	Mammalian cells, rat hippocampal NSCs	114
PM	Polarity signaling	PIF6-PhyB	Pard3	Association	Zebrafish embryos	74
PM	Release of hormones	BphS	BldD	c-di-GMP synthesis	Mammalian cells, C57BL/6J mice	167
PM	Insulin secretion	PhotoETP	GLP-1R	Allosteric switch	Mammalian cells, C57BL6 mouse islets	123
Cyt	Cargo transport	LOV-PDZ/CRY2-CIBN	Motor proteins	Association	Mammalian cells, rat hippocampal neurons	129, 130

Table 2 (cont.)

Site	Function	Module	Target	MOA	Organism	Ref.
Cyt	Peroxisome transport	AsLOV2	PTS	Caging	Mammalian cells	131
Cyt	Enzymatic activity	AsLOV2	Src, Rac1	Allostery	Mammalian cells	133
Cyt	Inhibition of JNK and p38MAPK	AsLOV2	Peptides	Caging	Mammalian cells, cerebellar granule neurons	134
Cyt	Inhibition of CaMKII	AsLOV2	Peptides	Caging	Mammalian cells, mice hippocampal slices, mice	135
Cyt	Apoptosis	CRY2-CIBN	Bax	Association	Mammalian cells	132
Cyt	Kinase activity, synaptic vesicle trafficking	pdDronpa	Kinases	Caging	Mammalian cells, *C. elegans*	69
Cyt	Intracellular phase transition	CRY2	IDRs	Clustering	Mammalian cells	137
Cyt	Protein trans-splicing	AsLOV	Intein	Caging	Mammalian cells	136
Nuc	Transcription	CRY2-CIBN	Cre	Association	Ai9 mice cultured neurons	143
Nuc	Transcription	NVOC-Met	pMET-17	Caging	Yeast	94
Nuc	Transcription	TAEL	Sox32, lefty1, Cas9	Caging, association	Zebrafish embryos	148
Nuc	Transcription	CRY2-CIBN	dCas9	Association	Mammalian cells	145
Nuc	Transcription	CRY2-CIBN	Il1RN, HBG1, HBG2, ASCL1	Association	Mammalian cells	146
Nuc	Transcription	CRY2-CIB1 (variants)	Cre	Association	Yeast, mammalian cells	70
Nuc	Transcription, translocation	DMNB	ABA	Caging	Mammalian cells	84
Nuc	Transcription, behavior	CRY2-CIBN	GCaMP3.0, TRPA1	Association	*Drosophila* S2 cells, *Drosophila* embryos	147

Table 2 (cont.)

Site	Function	Module	Target	MOA	Organism	Ref.
Nuc	Epigenetic perturbations	CRY2-CIB1	Grm2, Histone	Association	Mammalian cells, cortical & prefrontal cortex neurons	149
Nuc	Protein shuttling, transcription	PIF3-PHYB	VP-16/ TetR	Association	Mammalian cells, zebrafish embryos	139
Nuc	Nuclear export	AsLOV2	CRM1	Caging	Mammalian cells	140
Nuc	Genome editing	Magnets	Cre	Association	Mammalian cells	144
Nuc	Genome editing	Magnets	Cas9	Association	Mammalian cells	152
Nuc	Genome editing	Caged lysine	Cas9	Caging	Mammalian cells	92
Nuc	DNA recombination	dRap	Cre	Cleavage	Mammalian cells	83
Nuc	Histone acetylation	COMET probes	HDAC	Isomerization	Mammalian cells	150, 151
Nuc	Histone modification	AsLOV2	Bre1	Caging, association	Yeast	141
Nuc	DNA recombination	Caged a.a	Cre	Caging	Mammalian cells	93

ABA, abscisic acid; COMET, chemo-optical modulation of epigenetically regulated transcription; SOS, Son of Sevenless.

Controlling molecular machinery at the plasma membrane

Calcium signaling

Calcium signaling is essential for cellular function and is involved in a variety of cellular processes such as exocytosis, excitability, and motility [95]. Calcium signaling is also diverse in both space and time, requiring precise spatiotemporal control for accurate study [96]. Optobiological systems have been developed to address this need, but some of the first were not specific for calcium [97] and provided modest changes in the intracellular calcium concentration [98], which did not reach the physiological range. To produce more robust optobiological tools for calcium signaling, Ishii et al. engineered a photocaged fragment of stromal interaction module 1 (STIM1), the gating factor for the ORAI1 Ca^{2+} release-activated Ca^{2+} (CRAC) channel [99]. The

authors named this system 'blue light-activated Ca^{2+} channel switch', or BACCS. The human or *Drosophila* minimal STIM1 fragment was fused to the C-terminus of AsLOV2, which caused steric hindrance in the dark. Blue light-stimulated unfolding of the LOV Jα helix led to the exposure of the STIM1 fragment, which allowed it to interact with endogenous or exogenous ORAI1 channels to promote reversible extracellular Ca^{2+} influx within the physiological range. The authors demonstrated that the degree of Ca^{2+} influx was tunable based on the intensity of stimulating light, and that the induction could be spatially confined to axon tips and dendrites. Using a similar approach, He et al. developed a near-infrared(NIR)-inducible optogenetic system (Opto-CRAC) to manipulate Ca^{2+} influx and Ca^{2+}-dependent gene expression in immune cells to promote heightened immune responses and tumor suppression in a melanoma mouse model [100]. In line with these studies, Kyung et al. engineered OptoSTIM1, a light-inducible system to reversibly control Ca^{2+} influx through endogenous ORAI1 channels [101]. By fusing CRY2PHR to a truncated form of cytosolic STIM1, the authors used blue light to form OptoSTIM1 clusters, which translocated to the plasma membrane to activate ORAI1 channels. More recently, Park et al deployed the earlier-described CRY2clust tool in OptoSTIM1 to obtain two-fold faster changes in intracellular Ca^{2+} levels [72].

Modification of phosphoinositides

Phosphoinositides in the plasma membrane are spatiotemporally regulated and they play a key role in the regulation of integral membrane proteins and a variety of cell signaling events [102]. Xie et al. used the CRY2-CIBN protein pair to investigate how membrane depletion of phosphatidylinositol 4,5-bisphosphate (PI(4,5)P2) affects the Ca^{2+}-triggered secretion of insulin from cultured pancreatic β cells [103]. CIBN was anchored to the plasma membrane by a

farnesylation motif and CRY2 was fused to a 5'-phosphatase. Blue light illumination induced membrane recruitment of the 5'-phosphatase, where it could catalyze the conversion of PI(4,5)P2 to phosphatidylinositol 4-phosphate (PI(4)P). PI(4,5)P2 depletion reduced Ca^{2+} influx and suppressed insulin secretion, thereby highlighting PI(4,5)P2 as a key regulator of voltage-dependent Ca^{2+} channels and Ca^{2+}-triggered insulin secretion from pancreatic β cells. PI(4,5)P2 is also known to regulate actin polymerization at the plasma membrane [104]. Because cell contractility depends on cortical actin dynamics, which in turn relies on the plasma membrane levels of PI(4,5)P2, membrane depletion of PI(4,5)P2 arrested ventral furrow formation in developing drosophila embryos [105].

Phosphatidylinositol 3,4,5-triphosphate (PI(3,4,5)P3) is regarded as a secondary messenger downstream of phosphatidylinositol 3-kinase (PI3K) that regulates actin polymerization and cell polarity [106]. Kawano et al. induced spatially confined generation of PI(3,4,5)P3 on the plasma membrane of NIH3T3 cells [68]. By pairing the Magnet variants nMagHigh1 and pMagFast2, where the former was membrane-anchored and the latter cytosolic, they used blue light to recruit the pMagFast2-fused, P110 catalytic subunit of PI3K to the plasma membrane. Localized lamellipodia protrusion and plasma membrane ruffles occurred on the illuminated portion of the cell and membrane retraction occurred on the non-illuminated rear side.

Modulation of GTPase activity

Small Rho GTPases including RhoA, Rac1 and Cdc42 are well known as regulators of cytoskeletal dynamics in processes such as cell motility, polarity, cell cycle and many others [107,108]. Therefore, controlling and perturbing their activity with spatiotemporal precision is of

great interest and use in biological research. Guntas and colleagues used the iLID system to recruit the guanine nucleotide exchange factors (GEFs) ITSN and Tiam1 to user-defined spots on the plasma membrane of fibroblasts, allowing control of local GTPase activity in a blue-light dependent manner. Membrane recruitment of GEF evoked lamellipodia formation and membrane ruffling in a localized fashion [63]. Wang et al. used the LOVTRAP system to drive cell edge oscillations by mimicking the natural oscillatory pattern of the underlying signaling pathways [65]. Constitutively active forms of Rac1, RhoA and their upstream GTP exchange factor Vav2 were fused to the Zdk protein and sequestered on mitochondria containing LOV2. Interestingly, Vav2 activation generated a sustained increase in protrusion and extension velocities.

Successful cell division relies on spatiotemporal precision in the assembly and function of the actomyosin-based contractile ring [109]. To investigate the spatial and temporal regulation of cytokinesis, Wagner and Glotzer developed PR_GEF, a cytosolic tandem PDZ-tagged catalytic domain of a RhoA GEF, for the specific activation of RhoA, a membrane-bound GTPase functional in contractile ring assembly during cytokinesis [110,111]. By anchoring a LOV-caged PDZ binding epitope at the plasma membrane, light-induced uncaging of the epitope allowed membrane recruitment of PR_GEF and subsequent RhoA activation. When tested in non-contractile early anaphase cells with a blocked endogenous activating pathway for RhoA, PR_GEF successfully induced cytokinetic furrows within the spatially defined illumination zones spanning both the cell midzone and the poles, but ingression was incomplete.

Modulation of kinase signaling

Kinase signaling pathways underlie all major cellular processes such as growth, proliferation, differentiation, migration, polarization and apoptosis. Achieving precise control over the activation of these pathways has been technically challenging. In addition, ligand dose-response relationship is often non-linear, which is further confounded by adaptive responses as well as oscillatory responses [112]. Since embryonic development requires inviolable spatiotemporal control, perturbing developmental signaling remains a prime challenge. Optobiology tackles this challenge by appending photoactivatable proteins to the target and rendering it responsive to light, the application of which can be controlled with spatiotemporal precision.

RTKs can activate spatially and temporally distinct signaling networks to mediate cellular processes such as cell survival, migration, proliferation, and differentiation [113]. To bypass ectopic overexpression of receptors, Bugaj et al. developed a light-activated system called Clustering Indirectly using Cryptochrome 2, or CLICR, to precisely control endogenous RTK signaling in space and time [114]. CRY2 was fused to the src homology 2 (SH2) domain of PLCγ, an RTK binding domain (BD) that has limited affinity as a monomer. Blue light-induced cytosolic clustering of the BD-CRY2s increased their avidity to associate with and consequently activate endogenous RTKs. Blue light illumination resulted in successful RTK targeting in several cell types expressing the CLICR system. Specifically, the system was found to modulate endogenous PDGFRβ, a mediator of fibroblast chemotaxis.

Our recent work investigated the effect of timed kinase activity on embryonic development. Using the CRY2PHR-CIBN system, we activated ERK via membrane recruitment of Raf1 in PC12 neuroblasts and in *Xenopus* embryos. It was known that hyperactive ERK

results in the formation of ectopic tail-like structures in developing *Xenopus* embryos [115]. It was unclear whether ectopic tail induction was restricted to any specific developmental time window. By optically hyperactivating ERK during and post gastrulation, we demonstrated that these structures can be induced by hyperactive ERK even after gastrulation [116,117]. Johnson et al. used the iLID system to probe the importance of the signaling precision of ERK in *Drosophila* embryonic development [118]. Blue light-induced uncaging of a plasma membrane anchored iLID was used to recruit Son of Sevenless (SOS), a Ras activator, to the membrane, which then activated ERK signaling. Two different regions in the embryo exhibited differential sensitivity to the same ERK signal – the middle of the embryo was most sensitive and the poles were unaffected. Interestingly, hyperactive ERK-induced segmentation defects and subsequent lethality occurred only during a brief window of ERK hyperactivation.

The PI3K signaling pathway is another primary pathway downstream of RTK activation. In response to insulin, PI3K signaling regulates the membrane translocation of glucose transporter 4 (GLUT4) storage vesicles (GSVs) [119,120]. Akt, or protein kinase B, is downstream of PI3K activation and is a spatiotemporally-regulated kinase with a variety of intracellular substrates that mediate diverse cellular functions [121]. To delineate PI3K and Akt's contributions to insulin-regulated GLUT4 trafficking, Xu et al. used the CRY2-CIBN system to recruit either the PI3K catalytic domain (Opto-PIP3) or Akt (Opto-Akt) to the plasma membrane [122]. In adipocytes, compared with insulin stimulation, light-mediated activation of Opto-PIP3 induced a comparable magnitude of PIP3 generation, Akt phosphorylation, and GSV membrane translocation. Compared to Opto-PIP_3, Opto-Akt showed reduced GSV translocation.

Allosteric activation of G-protein-coupled receptor

Allosteric regulation has potential to increase drug specificity as drug discovery is presently hampered by the inability to control allosteric sites. The ligand dependent allosteric activator 4-(3-(benzyloxy)phenyl)-2-(ethylsulfinyl)-6- (trifluoromethyl)pyrimidine (BETP) is known to modulate activity of glucagon-like peptide-1 receptor (GLP-1R), a class B G-protein-coupled receptor that is involved in maintenance of glucose levels. Broichhagen et al. constructed PhotoETP, a photoswitchable moiety that achieved light-mediated allosteric control of GLP-1R [123]. Isomerization of photoETP between its *trans*- and *cis*- states can be induced by blue (440 nm) and UV (330 nm) light. Similar to BETP, *trans*-PhotoETP potentiates GLP-1R through ligand-induced increase of cAMP and Ca^{2+} levels. This functionality can be switched off through UV illumination, which converts *trans*-PhotoETP to its *cis* form.

Controlling molecular machinery in the cytoplasm

Control of organelle and protein trafficking

Precise positioning of organelles at specific subcellular locations plays a crucial role in coordinating signal transduction and cell fate determination, particularly in polarized neuronal cells. For instance, mitochondrial positioning near the plasma membrane is crucial to maintain Ca^{2+} influx and T-cell activation [124,125], and specific endosome localization leads to neuron polarization and outgrowth [126]. Not surprisingly, defective organelle trafficking is involved in multiple neurological diseases such as Alzheimer's disease, Parkinson's disease, and amyotrophic lateral sclerosis [127]. A key question is whether defective organelle trafficking is a cause or consequence of neurological disorders. Answering this question requires tools that can control organelle trafficking in live cells, and recent developments in optobiology provide such

tools. Recent work on optogenetic control of cargo trafficking has been reviewed [128]. Attaching photoactivatable proteins such as LOVpep-PDZ [129] or CRY2PHR-CIBN [130] to motor proteins and cargoes allows for the control of organelle trafficking by light. Additionally, light can also be used to control protein localization to a specific organelle. For instance, Spiltoir et al fused GFP to AsLOV2, which caged a peroxisomal-targeting sequence (PTS) in the dark. Unwinding of the ASLOV2 Jα helix under blue light exposed the PTS, which then bound to the Pex5 peroxisomal import receptor, thereby allowing translocation of the protein to the peroxisome [131]. In addition, light-induced trafficking of the pro-apoptotic protein Bax to the outer mitochondrial membrane was used to initiate apoptosis [132].

Control of enzymatic activity

Precise spatiotemporal control of enzymatic activity is necessary to better investigate the biochemical complexity of living cells. As a recurring theme in optobiology, one method to achieve this relies on engineered allosteric control of the target enzyme of interest. Dagliyan et al. described a generalizable approach for genetically inserting light-sensitive allosteric switches into enzymes to control their activity using light [133]. The authors inserted an AsLOV2 as the photoswitch into nonconserved surface "tight loops" that were mechanically coupled to the active site of a constitutively active Src kinase and the Rac1 GTPase. In the dark, enzyme structure and function was unhindered. Upon blue light illumination, a conformational change was induced in the LOV2 domain, which was allosterically propagated to the host protein to disrupt its structure and function. Interestingly, the photoswitching in each engineered enzyme highly resembled the conversion between the natural active and inactive states of the wild-type enzymes as revealed by comparison to known crystal structures.

Enzymatic activity can be controlled by caging the catalytic domain of the enzyme of interest. By inserting a monomeric pdDronpa1 at the N-terminus of the kinase domain and within the FG loop, Zhou et al. reported light controllable kinase activity in MEK1, MEK2, and Raf1 [69]. The kinase domain is caged by the dimeric pdDronpa, whereas in the monomeric state it is exposed. Thus, kinase activity can be controlled by switching between cyan and violet light. The authors discovered a new negative feedback loop in the Raf/MEK/ERK pathway, where ERK activation induces phosphatase PP1 or PP2A to dephosphorylate MEK1/2. Using a similar strategy, the authors developed a photo-switchable cyclin-dependent kinase 5 (psCDK5), the activation of which relocated synaptic vesicles from dendrites to axons in *Caenorhabditis elegans.*

Enzymatic activity can also be controlled by engineering photocaged peptide inhibitors for the enzyme of interest. Melero-Fernandez de Mera et al. caged the C-terminal residues of the Jun amino-terminal kinase (JNK) inhibitor JIP1 using AsLOV2 (OptoJNKi) [134]. Uncaging of the inhibitor peptide under white or blue light enabled it to interact with and inhibit JNK, allowing for precise regulation of JNK activity in mammalian cells. Based on molecular dynamic simulations of OptoJNKi, the authors proposed adding a terminal phenylalanine residue as a simple method for effectively caging certain C-terminal peptides using AsLOV2. Using this approach, the authors also generated an inhibitor for p38MAPK, showcasing the method's general applicability to other peptide-based inhibitors. Similarly, Murakoshi et al. developed photoactivatable autocamtide inhibitory peptide 2 (paAIP2), an AsLOV2-caged inhibitor for endogenous Ca^{2+}/calmodulin kinase II (CaMKII) [135]. Activation of paAIP2 during the first 1-2 minutes of the induction of dendritic long-term potentiation inhibited the process in hippocampal slices and amygdalar neurons of mice.

Enzyme activity can be regulated by the complementation of its catalytically inactive fragments. Wong et al. engineered a photoactivatable protein trans-splicing system that allowed light-induced restoration of enzymatic activity [136]. A photoactivatable trans-splicing intein (LOVInC) was generated by caging one half of the naturally split DnaE intein from *Nostoc punctiforme* using AsLOV2. Light-induced uncaging allowed the split inteins to recombine and enable splicing between split enzyme fragments fused to the inteins to reconstitute enzymatic activity. This system was applied to activate enzymes including RhoA and the apoptotic protein Caspase-7.

Control of phase separation of liquid droplets

Although many biochemical interactions in cells occur within membrane-bound organelles such as mitochondria and the endoplasmic reticulum, they have also been observed in a variety of membrane-less organelles. For instance, ribonucleoprotein (RNP) granules are one type of membrane-less organelles that harbor RNA-protein interactions. A crucial driving force for these interactions is the concentration-dependent association between intrinsically disordered protein/regions (IDP/IDRs). RNA-binding proteins often have IDP/IDRs that facilitate their condensation into liquid-like droplets within cells. However, understanding of the physiological assembly of these granules largely depends on *in vitro* reconstitution, due to a lack of tools to probe protein phase transitions in live cells. Using an optogenetic assay, Shin et al. fused CRY2PHR to various sticky IDRs and used blue light to modulate their phase separation between liquid and gel-like structures in the cytoplasm of live cells [137]. Depending on the proximity to the phase boundary, these optoDroplets display distinct assembly kinetics – from

fully reversible structures to irreversible aggregates. Thus, optoDroplets facilitate studies of physiological assembly and pathological aggregates of liquid droplets in cells.

Controlling molecular machinery in the nucleus

Control of nucleocytoplasmic protein shuttling

Protein transfer into and out of the nucleus is critical for the tight regulation of gene expression and cell fate [138]. Beyer et al. developed a light-inducible system to control the nuclear localization of transcription factors in zebrafish [139]. By taking advantage of the intrinsic nuclear localization signal (NLS) of phytochrome interacting factor 3 (PIF3), synthetic transcription factors fused to PHYB with a nuclear export signal (NES) were translocated to the nucleus upon illumination with 660 nm light. The transcription factor activity was reversed using 740 nm light, leading to PHYB dissociation from PIF3 and nuclear export of the transcription factor.

To control nuclear export of proteins initially residing in the nucleus, Niopek et al. developed a reversible light-inducible nuclear export system, or LEXY, using an AsLOV2-caged NES [140]. An N-terminal NLS was also introduced into the construct to allow nuclear accumulation prior to illumination. In mammalian cell culture, blue light exposure uncaged the NES, allowing it to interact with the endogenous nuclear export receptor, CRM1, to mediate nuclear export of the construct through nuclear pores. Harnessing this mechanism, the authors created a chromatin-anchored LEXY variant through fusion with histone H2B to sequester CRM1 and reversibly inhibit endogenous nuclear export. Similarly, Yumerefendi et al. introduced a light-inducible nuclear exporter (LINX) by caging a super-PKI-2 NES within the Jα helix of AsLOV2 [141]. NLS sequences with varying strengths were used to direct the proteins to

nuclei in the dark. The tools developed by both groups showed rapid export-import kinetics with half-lives of seconds to minutes.

Control of gene expression

The Cre-LoxP system is commonly used to alter gene expression. A split Cre recombinase has been used with CRY2-CIBN to control gene expression with high spatiotemporal resolution in cell cultures [41], *Drosophila* [142], and mice [143]. This photoactivatable split Cre recombinase (PA-Cre 1.0) was constructed by fusing CRY2 and CIBN to the N- and C-half, respectively. A second-generation PA-Cre (PA-Cre2.0) was generated based on a CRY2 mutant, L348F, a slow cycler with a dissociation half-life of 24 min [70]. Compared with PA-Cre1.0, PA-Cre2.0 provided a five-fold increase in the dynamic range. Using Magnets, Kawano et al. also engineered a light-inducible split Cre recombinase system [144], where an nMag was fused to an N-Cre and a pMag was fused to a C-Cre. Because Magnets have slow photocycle kinetics (half-life 1.8 h), this split Cre system enabled DNA recombination in cells and in mice with a 30 second blue light pulse illumination.

Achieving simultaneous targeted transcriptional activation of multiple endogenous genes to perturb cells has been technically challenging. Two independent groups concurrently addressed this challenge by combining the versatility of the CRISPR-Cas9 system with optobiology to create similar light-activated CRISPR-Cas9 systems [145,146]. In both designs, a catalytically inactive dCas9 fused to CIB1/CIBN served as a customizable genomic anchor; a fusion containing CRY2PHR and a transactivation (TA) domain (P65/Vp64) was the activator. Blue light recruited the freely diffusive activator to the genome anchor, which constitutively occupied the promoter region of target genes. Both research groups demonstrated spatially

defined gene expression that correlated with the spatial pattern of illumination. Importantly, both groups achieved multiplexed photoactivation of genes in cultured cells using multiple sgRNAs to target these different genes simultaneously. Also by using the CRY2-CIBN system, Chan et al. achieved spatiotemporal control of gene expression in both embryonic and adult *Drosophila* tissues [147]. By using two-photon excitation, the authors restricted gene expression to a 20-μm region of interest, demonstrating excellent spatial control.

Transactivation domains commonly used in cultured cells could lead to toxicity when applied in certain multicellular organisms such as zebrafish. Reade et al. utilized a more tolerable KalTA4 TA domain to develop a light-inducible gene expression system for use in zebrafish embryos [148]. The authors fused the KalTA4 TA to EL222, a naturally occurring LOV-based transcription factor, to create a light-gated transcription factor (TAEL). Using TAEL, a single 2 min blue light pulse was sufficient to drive light-specific expression, and the system inactivated within 30 min after light was turned off. The authors demonstrated spatial control of TAEL by generating ectopic endoderm from ectoderm by driving Sox32 expression locally in the presumptive ectoderm. They then used TAEL to dissect the distinct roles of nodal signaling in early development (mesendoderm specification) and later development (left-right axis patterning).

Control of epigenetic states

Konermann et al. developed a modular two-component optogenetic system to facilitate control of gene transcription and epigenetic states in mammalian cells [149]. The first component is a genomic anchor generated by fusion of a customizable DNA-binding domain to CRY2. The second component is an effector domain fused to CIB1. Blue-light rendered the association of

CRY2 and CIB1 and recruited the effector domain to the target region enabling transcriptional repression or activation, depending on the nature of the effector. The modular nature of these light-inducible transcriptional effectors (LITEs) allows for flexibility in the DNA-binding region as well as the effectors thereby enabling a multitude of genomic or epigenetic modifications. Epigenetic mark-modifying LITEs (epiLITEs) were developed by including histone effectors in LITE to be used for locus-specific histone modification.

Controlling the subcellular localization of epigenetic modifiers is another powerful way to interrogate epigenetic states. The LINXa4 construct discussed earlier was used by Yumerefendi et al. to control a histone modifying E3 ubiquitin ligase Bre1 which monoubiquitylates (ub1) the histone H2B in yeast and promotes transcription [141]. Fusing an NLS-silenced Bre1 to LINXa4 in a BRE1 deletion strain, they demonstrated light-induced reversible loss of H2Bub1, which occurred within minutes. The kinetics of the accompanying H2Bub1-dependent histone modifications such as tri-methylation of lysine 4 on histone H3 (H3K4me3) and tri-methylation of lysine 79 on histone H3 (H3K79me3) were monitored, where the latter was observed to be much slower than the former, providing mechanistic insights into these epigenetic processes.

Reis et al. developed a method called chemo-optical modulation of epigenetically regulated transcription (COMET) to generate a blue light-dependent histone deacetylase (HDAC) inhibitor [150,151]. The authors amalgamated a fast-relaxing photochromic ligand para-methyl red (DABCYL) with an ortho-amino anilide (OAA) HDAC inhibitor that targets the catalytic zinc in the HDAC active site via electrostatic interactions. Blue light promoted *trans-cis* photoisomerization of DABCYL, which transmitted the electronic alteration to the attached zinc-chelating anilide for HDAC inhibition.

Genome editing

Attaining spatiotemporal and reversible control over genome editing with minimal cell invasiveness is a challenging goal. Nihongaki et al. used magnets to develop a photoactivatable RNA-guided endonuclease Cas9 (paCas9) for applications in CRISPR-mediated genome editing [152]. A split pair of Cas9 (N713, C714) was fused to pMag and nMag, respectively, creating paCas9-1. This construct showed no reduction in specificity compared to full-length Cas9 in homology dependent repair (HDR) assays, and could cleave endogenous mammalian genomic loci with 60% efficiency of that of Cas9. PACas9 could also be used in targeted genome editing via HDR when a donor repair template was supplied, with an incorporation frequency of 7.2%. Moreover, two additional functionalities were developed using paCas9-1: first, a single point mutation D10A converted paCas9-1 from an endonuclease to a nickase, which could reduce off-target genome modifications by making Cas9 activity dependent on a pair of guide RNAs instead of one; second, two point mutations D10A and H840A abolished Cas9 cutting activity, while retaining its targeting activity, which could be used to sterically block the transcription of a target-gene in an application termed CRISPR interference (CRISPRi) which was also demonstrated with luciferase reporters. Similarly, Reade et al. used TAEL to drive Cas9 expression in zebrafish, which led to tyrosinase gene disruption, demonstrating the CRISPR integration of TAEL for gene editing in multicellular organisms [148].

Using a photopharmacological strategy, Hemphill et al. engineered two Cas9 variants with photo-caged lysines at positions K163 and K866, which could be spatiotemporally activated with UV light [92]. The photo-caged Cas9 variants were completely inactive in the dark and achieved wild-type activity with 120 seconds of exposure to 365 nm light. Optical control of

CRISPR/Cas9 was used to silence the endogenous trans-membrane transferrin receptor, CD71, in HeLa cells.

Challenges and emerging new technologies

A major challenge in optobiology, both in basic sciences and in clinical research, is light delivery. Most photoactivatable proteins respond to visible light. The penetration depth for red light in biological tissues is around 0.2-2 mm [153]. Furthermore, as the light wavelength decreases, its penetration depth is reduced, severely limiting the use of visible light-responsive photoactivatable modules in deep tissues. Most *in vivo* optobiological applications have required the insertion of optical fibers to deliver visible light. This approach introduces a two-fold challenge: fibers impede free movement of the tethered animal and the insertion procedure may cause an inflammatory response in tissues.

Recent developments in nanotechnology have provided soft, stretchable, and implantable microLEDs that allow for wireless optobiology. These devices use miniaturized light-emitting diodes (LEDs) that are powered by radio-frequency (RF) scavengers [154-156]. To improve the chronic biocompatibility and integration with soft neuronal tissues and to use these devices in challenging areas such as the spinal cord and peripheral nervous system, fully implantable internal devices were made [157]. An improved multi-functional device, which included both optogenetic and microfluidic channels, allowed for the co-delivery of light and pharmacological reagents [158]. Organic LEDs have also been designed for high-resolution optogenetics [159] (Figure 3A).

Parallel to the development of microLEDs, researchers used upconversion nanoparticles (UCNPs) to convert near infrared (NIR) light (800-980 nm) to visible light, which shifted the

spectrum of illumination towards the NIR wavelength [160,161]. IR light has a higher penetration depth (~3-4 mm) than visible light [153]. For small animals, such as mice, this penetration depth can greatly help light reach deeper brain regions (Figure 3B). However, it remains challenging for IR light to penetrate deep brain regions of larger animals including humans. Biocompatible UCNPs have been used in photodynamic therapy (PDT) in deep tissues [162]. Recent proof-of-principle work showed that Er/Yb UCNPs coated with IR-sensitive dyes can be used to achieve optogenetic stimulation with 980 nm light in cell culture [163,164], *C. elegans* [165], and mice [100].

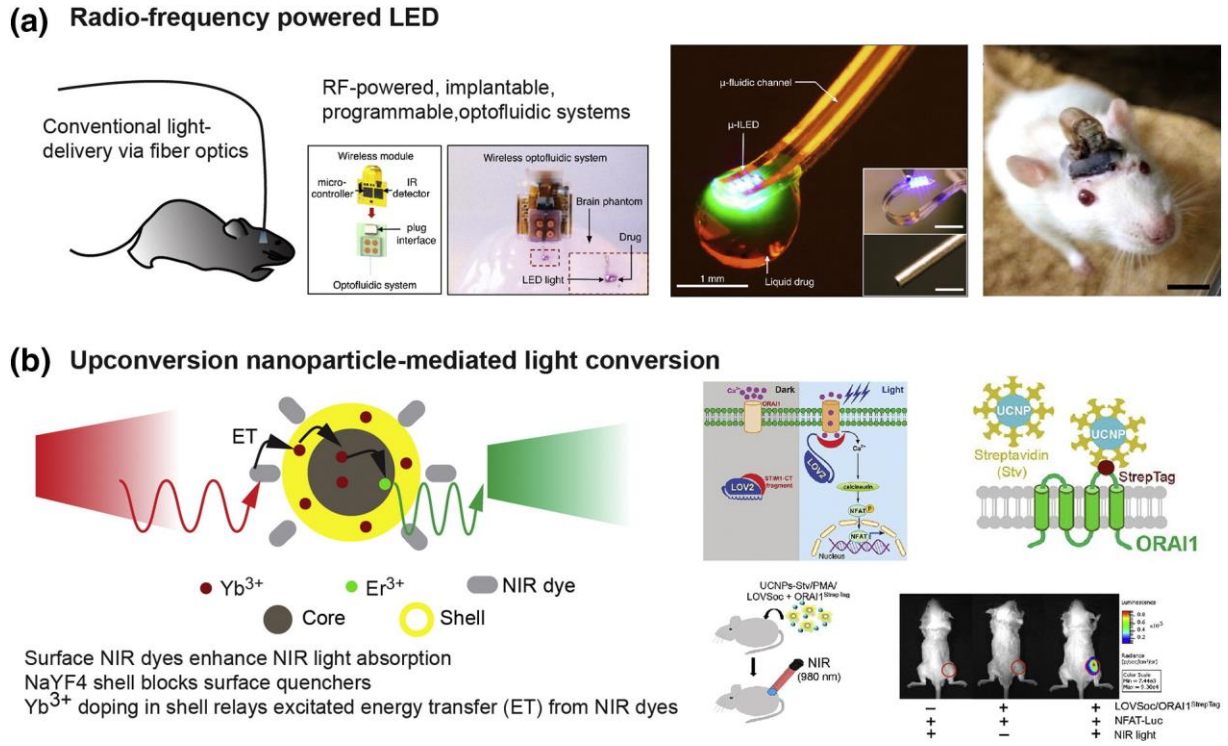

Figure 3. ***Emerging technologies for achieving wireless optobiological control in multicellular organisms***. (A) Wireless optobiology based on radio-frequency powered microLEDs. By integrating light source and microfluidic channels, these multiple-functionality devices can light up deep tissues in live animals and deliver pharmacological reagents. Reprint with permission from [158] (B) Upconversion nanoparticles (UCNPs) convert near infrared light, which has deeper penetration depth, to visible light through energy transfer from excited, surface-bound NIR dyes to the cores of UCNPs. The output visible light can be used to excite photoactivatable proteins. Reprint with permission from [100].

Outlook

Using photoactivatable moieties derived from nature, optobiology utilizes photoactivatable molecules in conjunction with proteins of interest to genetically engineer live cell systems. Parallel to the emerging field of synthetic biology, optobiology offers attractive approaches to customize cell and tissue responses. Orthogonal and multiplexed control of signaling circuits would help delineate endogenous signaling mechanisms. Additionally, novel functionality can potentially be created by exerting light control over proteins that normally do not interact with each other. From a molecular perspective, successful design of an optobiological system relies on insights from both molecular modeling and experimentation. Although several optobiological modules are available to choose from, benchmarking experiments have revealed that tool efficacy varies depending on the cellular context and application [64,166]. In general, trial and error investigation to identify the appropriate tool is often required. Reproducible strategies to insert, remove, modulate, or split modules in target proteins call for the development of universal design principles and utilities.

Beyond the bench, optobiology has also been applied in pre-clinical research using live animals. Recent work demonstrated a cell-based therapy that made use of smartphones to induce secretion of insulin via an optogenetic approach [167]. In this work, optogenetically engineered cells that allowed light-triggered release of glucose-lowering hormones were implanted in diabetic mice. The implanted cells responded to far-red light, which could be wirelessly controlled by a smartphone. Mouse insulin produced *in vivo* was able to maintain glucose homeostasis over several weeks in the diabetic mice. With superior spatiotemporal resolution, minimal invasiveness, and reversible operation, optobiological techniques promise to usher in a new era of molecular biology and biomedical research.

Acknowledgements

This work was supported by the University of Illinois at Urbana-Champaign (Kai Zhang). We thank L. Hanson (UC Berkeley) for help with figure design.

Abbreviations used

SHH: Sonic Hedgehog; TGFβ: transforming growth factor beta; BMP: bone morphogenetic protein; FGF: fibroblast growth factor; ERK: extracellular signal-regulated kinase; BDNF: brain-derived neurotrophic factor; AsLOV: *Avena sativa* light-oxygen-voltage; POI: protein of interest; TULIPS: tunable light-controlled interacting protein tags; LIDs: light inducible dimers; LOVpep: peptide epitope attached to AsLOV2 Jα helix; ePDZ: engineered Erbin PDZ domain; oLID: original light inducible dimers; iLID: improved light inducible dimers; LOVTRAP: LOV2 trap and release of protein system; Zdk: Zdark; sec: seconds; AUREO1: Aureochrome-1; bZIP: basic region/ leucine zipper domain; RTK: receptor tyrosine kinase; VVD: vivid; pdDronpa1: photodissociable dimeric Dronpa; psCDK5: photo-switchable cyclin-dependent kinase 5; CRY2: Cryptochrome 2; CIB1: cryptochrome-interacting basic-helix-loop-helix 1; CRY2PHR: CRY2 photolyase homology region; CIBN: CRY2 N-terminus; TF: transcription factor; PhyB: *Arabidopsis thaliana* phytochrome B; PCB: phycocyanobilin; BphP1: *Rhodopseudomonas palustris* bacterial bathy phytochrome; BV: biliverdin; iRIS: near-infrared-blue-light-inducible shuttle; dRap: dimerized rapamycin; ABA: abscisic acid; NVOC-Met: (S)-N-(4,5-dimethoxy-2-nitrobenzyloxycarbonyl)-methionine; BETP: 4-(3-(benzyloxy)phenyl)-2-(ethylsulfinyl)-6-(trifluoromethyl)pyrimidine; GLP-1R: glucagon-like peptide-1 receptor; PhotoETP: photoswitchable moiety for light-mediated allosteric control of GLP-1R; STIM1: stromal interaction module 1; CRAC: Ca^{2+} release-activated Ca^{2+}; BACCS: blue light-activated Ca^{2+}

channel switch; $PI(4,5)P_2$: phosphatidylinositol 4,5-bisphosphate; PI(4)P: phosphatidylinositol 4-phosphate; $PI(3,4,5)P_3$: Phosphatidylinositol 3,4,5-trisphosphate; PI3K: phosphatidylinositol 3-kinase; GEFs: guanine nucleotide exchange factor; prGEF: photo-recruitable GEF; CLICR: Clustering Indirectly using Cryptochrome 2; SH2: Src homology domain; BD: binding domain; SOS: Son of Sevenless; GLUT4: glucose transporter 4; GSV: GLUT4 storage vesicles; PTS: peroxisomal targeting sequence; Jnk: Jun N-terminal kinase; LOVInC: photoactivatable protein trans-splicing intein; RNP: ribonucleoprotein; (IDP/IDR): intrinsically disordered protein/regions; PIF3: phytochrome interacting factor 3; NLS: nuclear localization signal; NES: nuclear export signal; LEXY: light-inducible nuclear export system; LINX: light-inducible nuclear exporter; PA-Cre 1.0: photoactivatable split Cre recombinase; TA: transcriptional activation; TAEL: TA EL222; LITE: light-inducible transcriptional effectors; epiLITE: epigenetic mark-modifying LITE; ub1: monoubiquitin; H3K4me3: tri-methylation of lysine 4 on histone H3; H3K9me3: tri-methylation of lysine 79 on histone H3; COMET: chemo-optical modulation of epigenetically regulated transcription; HDAC: histone deacetylase; DABCYL: fast-relaxing photochromic ligand para-methyl red; OAA: ortho-amino anilide; paCas9: photoactivatable Cas9 nuclease; HDR: homology dependent repair; CRISPERi: CRISPER interference; LED: light emitting diodes; RF: radio frequency; UCNP: upconversion nanoparticles; NIR: near-infrared; IR: infrared; PDT: photodynamic therapy.

CHAPTER 2: OPTOGENETIC DELINEATION OF RECEPTOR TYROSINE KINASE SUBCIRCUITS IN PC12 CELL DIFFERENTIATION

This work contains previously published material.[*]

Abstract

Nerve growth factor elicits signaling outcomes by interacting with both its high-affinity receptor, TrkA, and its low-affinity receptor, p75NTR. Although these two receptors can regulate distinct cellular outcomes, they both activate the extracellular-signal-regulated kinase pathway upon stimulation with ligand. To delineate TrkA subcircuits in PC12 cell differentiation, we developed an optogenetic system where light was used to specifically activate TrkA signaling in the absence of nerve growth factor. By using tyrosine mutants of the optogenetic TrkA in combination with pathway-specific pharmacological inhibition, we find that Y490 and Y785 each contribute to PC12 cell differentiation through the extracellular-signal-regulated kinase pathway in an additive manner. Optogenetic activation of TrkA eliminates the confounding effect of p75NTR and other potential off-target effects of the ligand. This approach can be generalized for the mechanistic study of other receptor-mediated signaling pathways.

[*] **Khamo, J.S.** et al. (2019). Optogenetic Delineation of Receptor Tyrosine Kinase Subcircuits in PC12 Cell Differentiation. Cell Chem Biol 26, 400-410.

Introduction

The dimeric secretory nerve growth factor (NGF), the first discovered neurotrophin, exerts a broad spectrum of neuronal functions including cell survival, growth, differentiation [168], tissue regeneration [169], pain [170], synaptogenesis, and synaptic plasticity [171]. Trophic effects of NGF result from its interaction with the high-affinity receptor tropomyosin receptor kinase A or TrkA [172]. Upon binding to NGF, TrkA undergoes auto-phosphorylation of specific tyrosines in its intracellular domain (ICD). Phosphorylated tyrosines in the TrkA ICD serve as docking sites for distinct downstream effectors to activate canonical downstream signaling pathways including the extracellular-signal-regulated kinase **(**ERK) and phospholipase C-γ (PLCγ) pathways [173].

Outcomes of TrkA signaling have been complicated, however, by the discovery that NGF also binds to its low-affinity receptor, p75NTR [174]. In fact, p75NTR binds to other neurotrophins including brain-derived neurotrophic factor, neurotrophin-3, and neurotrophin-4/5 with similar affinities [175]. Evidence suggests a two-fold neuronal function of p75NTR: 1) it can functionally collaborate with TrkA to enhance neurotrophin binding and receptor activation [176,177], and 2) it can also induce cell apoptosis via ProNGF-dependent signaling processes [178]. Although NGF stimulation leads to ERK phosphorylation primarily through its binding to TrkA, ERK activation can also be mediated by p75NTR [179]. Thus, the existence of multiple receptors for NGF makes it challenging to delineate specific roles of TrkA subcircuits in the biological context [168,180].

To delineate sole contributions of TrkA and p75NTR to NGF signaling, *in vitro* and *in vivo* models have been developed. Cell lines and transgenic animal models with either gene disrupted have been generated. For instance, the PC12nnr5 cell line expresses only p75NTR (lacking TrkA) [181], while PC12-p75^{-} cells express only TrkA (lacking p75NTR) [182]. Additionally, 3T3 cells have been engineered to express TrkA or p75NTR [183]. Similarly, p75NTR mutant mice

[184] and TrkA knock-out mice [185] have been developed. However, caution should be warranted with genetic manipulation for at least two reasons: first, complete deletion of a gene may undesirably corrupt its roles in other cellular functions. For instance, p75NTR is widely expressed in non-neuronal tissues [186] and is involved in processes such as liver repair [187] and muscle regeneration [188]. Second, genetic manipulation often causes delayed responses and constitutive alteration of gene expression in cells. Alternatively, pharmacological inhibition can be used to primarily target specific pathways to dissect the NGF signaling network. However, potential off-target effects should be considered [189-191].

Even at the level of TrkA, contradictory evidence exists with respect to the functionality of its downstream subcircuits. Upon phosphorylation, two tyrosine residues, Y490 and Y785, serve as primary docking sites for downstream effectors. Y490 associates with Shc and Src domains [192], which further activate the Raf/MEK/ERK signaling pathway, whereas Y785 associates with PLCγ (Figure 4). Work based on a chimeric receptor, a fusion protein of the PDGFR extracellular domain (ECD) and TrkA ICD, shows that the mutation of Y785 in TrkA, which is believed to primarily activate the PLCγ signaling pathway, does not affect PC12 cell differentiation [193]. However, overexpression of the Src Homology domains of PLCγ1 inhibits NGF-induced PC12 cell differentiation [194], presumably through competition with endogenous PLCγ for receptor interaction. This discrepancy can arise from unknown off-target effects of the ligand or overexpressed protein domains, both of which are challenging to analyze quantitatively. Thus, delineation of TrkA subcircuits calls for the development of new strategies that can evaluate the functionality of specific tyrosines of the TrkA ICD with a clean biological context free from potential off-targets.

The emerging optogenetic techniques provide a new way to study signaling mechanisms by integrating photoactivatable proteins with signaling molecules [44,48,195-200]. As light can be easily manipulated with high spatial and temporal resolution, optogenetic control of signaling can provide insights into the kinetic and spatial features of signal transduction. In addition, light can bypass ligand-binding to specifically interrogate optogenetically engineered receptors, whose ligand can interact with and signal through multiple known and potentially unidentified receptors.

Here, we use an optogenetic approach to specifically elucidate the signaling outcomes of TrkA subcircuits in the absence of NGF. By constructing wild-type and tyrosine mutants of the optogenetic TrkA receptor, we control canonical TrkA signaling without introducing a ligand-based chimeric receptor or disturbing the endogenous TrkA expression and function. We find that both Y490 and Y785 of TrkA regulate PC12 cell differentiation, with Y490 primarily activating the ERK pathway and Y785 contributing to the ERK signaling cascade in a PLCγ- and PKC-dependent manner.

Results

System construction

Natural signal transduction mediated by TrkA sequentially involves NGF interaction with the receptor ECD, receptor dimerization, and a series of autophosphorylation at key tyrosines throughout the receptor ICD (Figure 4A). Several tyrosines located within the receptor kinase domain are critical for optimal kinase activity, and some tyrosines located outside of the kinase domain serve as docking sites for initiating factors of intracellular signaling pathways. To bypass the ligand requirement for receptor activity, we constructed an optogenetic TrkA (Lyn-

TrkAICD-AuLOV-GFP) by fusing a homo-associating domain, the light-oxygen-voltage domain of aureochrome1 from *V. frigida* (AuLOV) [67], to the ICD of the wild-type TrkA receptor (Figure 4B). This construct will be referred to as "WT ICD." Lyn is the lipidation motif of the Src family Lyn kinase, which serves as a membrane-targeting peptide that replaces the transmembrane and extracellular domain of TrkA. This construct is different from a previously reported optogenetic TrkA system, which used the full-length TrkA fused to the photoactivatable protein, cryptochrome 2 [201]. We chose to control TrkA ICD alone to avoid the potential interaction of TrkA ECD with other receptors such as p75NTR [202], although this interaction is a subject of debate [203]. For practical convenience, we chose AuLOV because of its smaller size (145 a.a.) compared to cryptochrome 2 (498 a.a.). In our system, we expected that light-induced homo-association of AuLOV would bring TrkA kinase domains within proximity of each other to initiate the cross- and autophosphorylation of specific tyrosines throughout the ICDs, including Y490 and Y785. To delineate the signaling outcomes of these two docking sites, we also constructed single tyrosine-to-phenylalanine mutants (Y490F, Y785F) and a double mutant (Y490/785F) of WT ICD. Note that light-induced activation of the optogenetic TrkA system should not activate the endogenous wild-type TrkA.

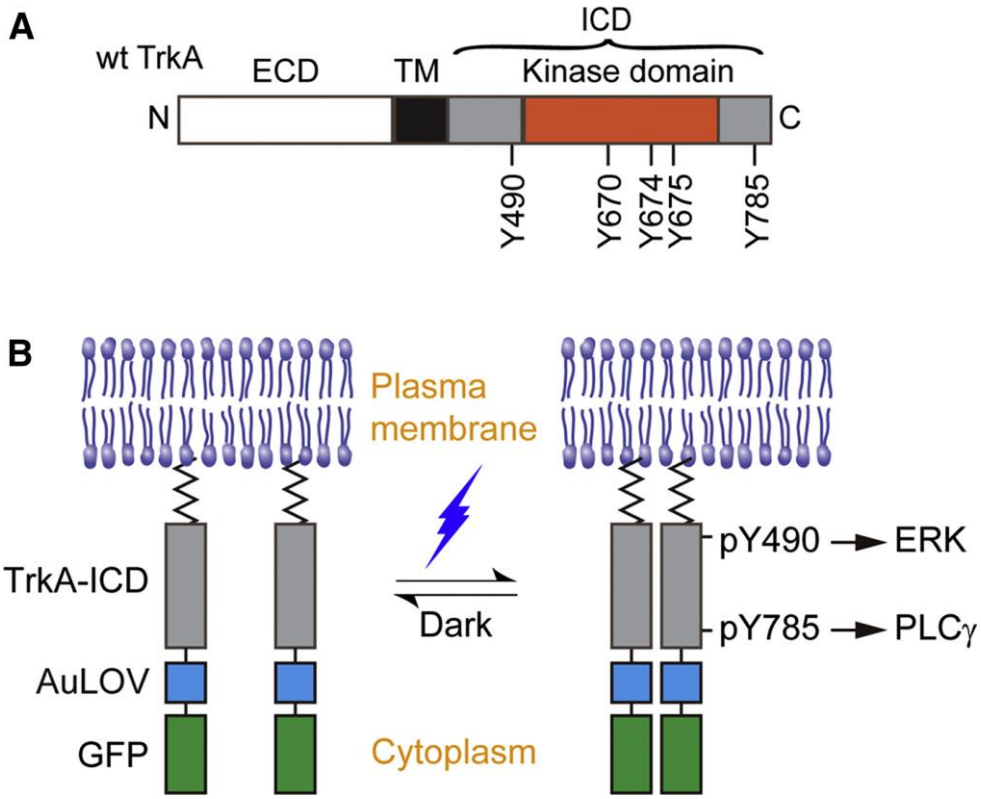

Figure 4. ***Design of the optogenetic TrkA system***. (A) Representation of the wild-type TrkA receptor. TrkA is a Type I transmembrane protein anchored at the plasma membrane by a single-helix transmembrane domain (TM). Nerve growth factor (NGF) associates with the extracellular domain (ECD) to promote receptor dimerization and phosphorylation of key tyrosines within the intracellular domain (ICD). Y670, Y674, and Y675 are critical for kinase activity, while Y490 and Y785 are involved in the initiation of the Raf/MEK/ERK and PLCγ-PKC signaling pathways, respectively. (B) Schematic representation of the optogenetic TrkA receptor. The ECD and TM are replaced by a lipidation motif to abolish ligand sensitivity, while retaining normal orientation and localization at the plasma membrane. Light sensitivity is introduced through fusion with the photosensitive protein, AuLOV. Illumination with blue light should promote dimerization of receptor ICDs and activation of downstream signaling pathways. Green fluorescent protein (GFP) serves as a probe for system expression.

Blue light illumination induces homo-association of optogenetic TrkA in live cells

When overexpressed in PC12 cells, WT ICD and its mutant variants localized primarily on the plasma membrane (Figure 5A). Compared to a cytosolic GFP, optogenetic TrkA variants showed a higher fluorescence intensity at the plasma membrane relative to the cytoplasm (Figure 5B). In the absence of ligand binding, the plasma membrane is the main subcellular localization

of wild-type TrkA in PC12 cells, which was revealed in previous work by crosslinking NGF with wild-type TrkA [204] as well as immunostaining of TrkA [205]. In addition, overexpression of fluorescently labeled TrkA results in primary targeting to the plasma membrane [206,207]. Here, we reproduced the results of TrkA overexpression and found that TrkA-mCherry overlapped with WT ICD in PC12 cells (Figure 5C), suggesting that the Lyn sequence allows for subcellular localization of TrkA ICD to the natural membrane compartment of full-length TrkA.

To confirm that blue light could induce the homo-association of WT ICD, we performed a bimolecular fluorescence complementation (BiFC) assay based on split Venus fragments, VN (amino acid 1-154) and VC (amino acids 155-238) [208,209]. Two plasmids were constructed: Lyn-TrkAICD-AuLOV-VN and Lyn-TrkAICD-AuLOV-VC. As expected, after 20 minutes of blue light illumination, fluorescence intensity from cells co-transfected with both plasmids increased (Figure 5 D-E). In cells co-transfected with the No AuLOV control (Lyn-TrkAICD-VN and Lyn-TrkAICD-VC), the same dose of blue light did not increase the fluorescence intensity (Figure 5 F-G).

We also used structured illumination microscopy (SIM) to probe blue-light-induced receptor homo-association. MDA-MB-231 cells were transfected with WT ICD and were exposed to blue light. To quantify the light-induced homo-association of WT ICD, we analyzed the SIM images using the thresholding technique. By setting the threshold at the midpoint value between the minimal and maximal intensity of the background-subtracted cell images, we calculated the percentage of above-threshold regions over the whole cell area using ImageJ based on a published protocol [210]. Following 5 minutes of blue light (405 nm) illumination, the above-threshold percentage increased in cells transfected with WT ICD, in stark contrast to cells

transfected with the No AuLOV control (Lyn-TrkAICD-GFP), which showed no increase in the above-threshold percentage (Figure 5 H-I).

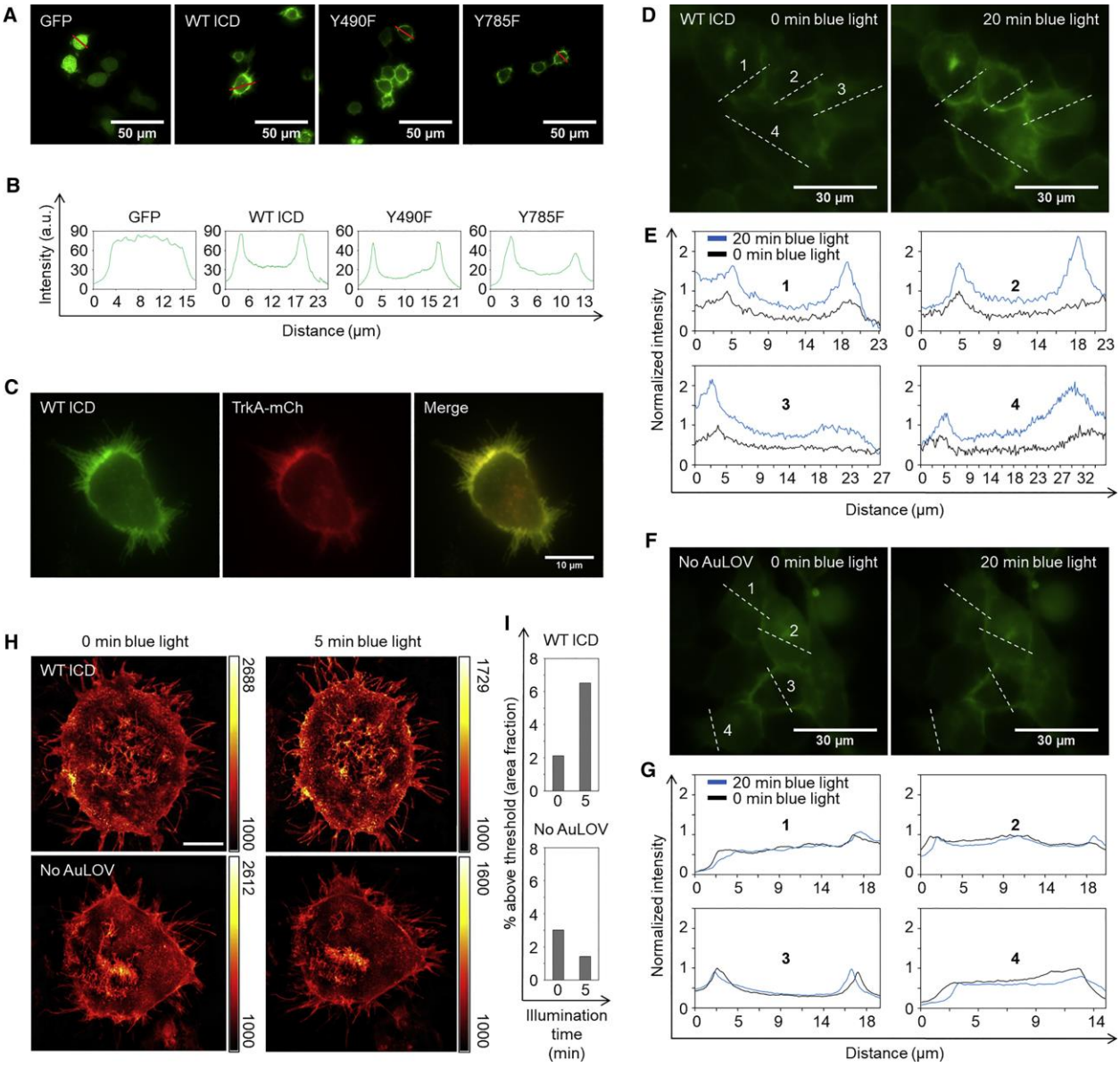

Figure 5. ***Optogenetic TrkA localizes to the plasma membrane and homo-associates in response to blue light***. (A) Fluorescence microscopy images of PC12 cells expressing a cytosolic GFP or variants of the optogenetic TrkA system. (B) Red-line profile analysis of fluorescence images in (A) reveals a strong membrane localization of the optogenetic constructs. (C) Overexpression of WT ICD and TrkA-mCherry shows that both fusion proteins primarily localize to the plasma membrane. (D) Bimolecular fluorescence complementation assay based on split Venus fragments. A 20-minute blue light illumination (5 mW/cm^2) increased the

Figure 5 (cont.) fluorescence intensity in cells co-transfected with Lyn-TrkAICD-AuLOV-VN and Lyn-TrkAICD-AuLOV-VC. Images of the same cells were acquired before and after blue light treatment. (E) Intensity quantification along four dash-line profiles outlined in (D). (F-G) Same as (D-E) except that a No AuLOV control, Lyn-TrkAICD-VN and Lyn-TrkAICD-VC, is used. The same blue light illumination does not enhance the fluorescence intensity. Data shown in (D-G) are for representative cells of more than 500 cells (N>500) from two biological replicates (n=2). (H) Structured illumination microscopy (SIM) images of MDA-MB-231 cells expressing WT ICD (top panels) or No AuLOV control (bottom panels) before and after blue light (405 nm) irradiation. (I) Quantification of the fraction of images whose intensity is above a threshold set at 50% of the maximum intensity of the background-subtracted images. Data shown in (H-I) represent WT ICD (N=4) and No AuLOV (N=3) from two biological replicates (n=2). Scale bar = 10 μm.

In addition to microscopy, we were inspired by a previous optogenetic study [211] to use native PAGE to resolve the light response of AuLOV. Cells were transfected with WT ICD and lysates were harvested in 0.5% Triton X-100 in PBS. Lysates were treated with blue light (5 mW/cm^2) for 5 minutes or kept in the dark. Equal amounts of each lysate were loaded on a native gel. The lane containing the illuminated sample underwent continued exposure to blue light throughout the electrophoresis. Samples were then analyzed by western blot using an anti-GFP antibody. As expected, blue light resulted in a reduced-mobility shift of the most prominent band in the dark control, indicative of light-mediated homo-association (Figure 6).

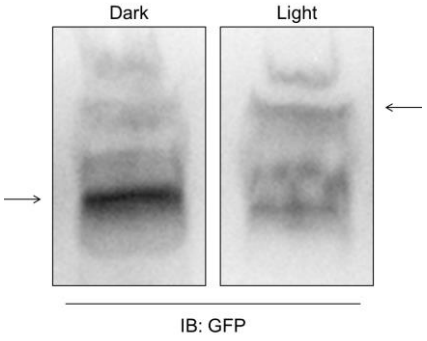

Figure 6. ***Native PAGE mobility shift assay shows that blue light induces homo-association of WT ICD***. The most prominent band in the dark control (left arrow) was depleted in the light sample, which coincided with an enrichment of a low mobility band (right arrow). This figure shows the result of one experiment (n=1).

Light-induced activation of optogenetic TrkA results in PC12 cell differentiation

PC12 cells project neurites in response to NGF stimulation, a process referred to as differentiation (Figure 7A). We proceeded to determine whether WT ICD activation could achieve a similar cellular outcome. PC12 cells transfected with WT ICD were exposed to blue light (300 $\mu W/cm^2$) for two days in a humidified 37 °C CO_2 incubator before their fluorescence images were acquired. Light stimulation of these cells resulted in significant differentiation (45%) compared to cells kept in the dark (12%) (Figure 7B). Cells expressing the optogenetic construct without the TrkA ICD (No ICD) showed little differentiation in both light and dark (<5%), indicating that light-induced differentiation was ICD-dependent. Cells expressing No ICD showed robust differentiation (>68%) when treated with 50 ng/mL NGF, indicating that endogenous TrkA retained ligand sensitivity and signaling activity.

Light-induced activation of optogenetic TrkA mutants results in diminished PC12 cell differentiation

To determine the functional role of Y490 and Y785 in differentiation, we transfected PC12 cells with mutant constructs and illuminated for 24 hours as previously described. Cells expressing Y490F or Y785F exhibited significantly reduced levels of light-induced differentiation (18% or 15%, respectively) compared to cells expressing WT ICD (36%) (Figure 7 C-D). Furthermore, the degree of differentiation undergone by cells expressing Y490/785F (6%) was similar to that displayed by cells expressing No ICD (4%), suggesting that Y490 and Y785 each contributed to TrkA-mediated PC12 cell differentiation.

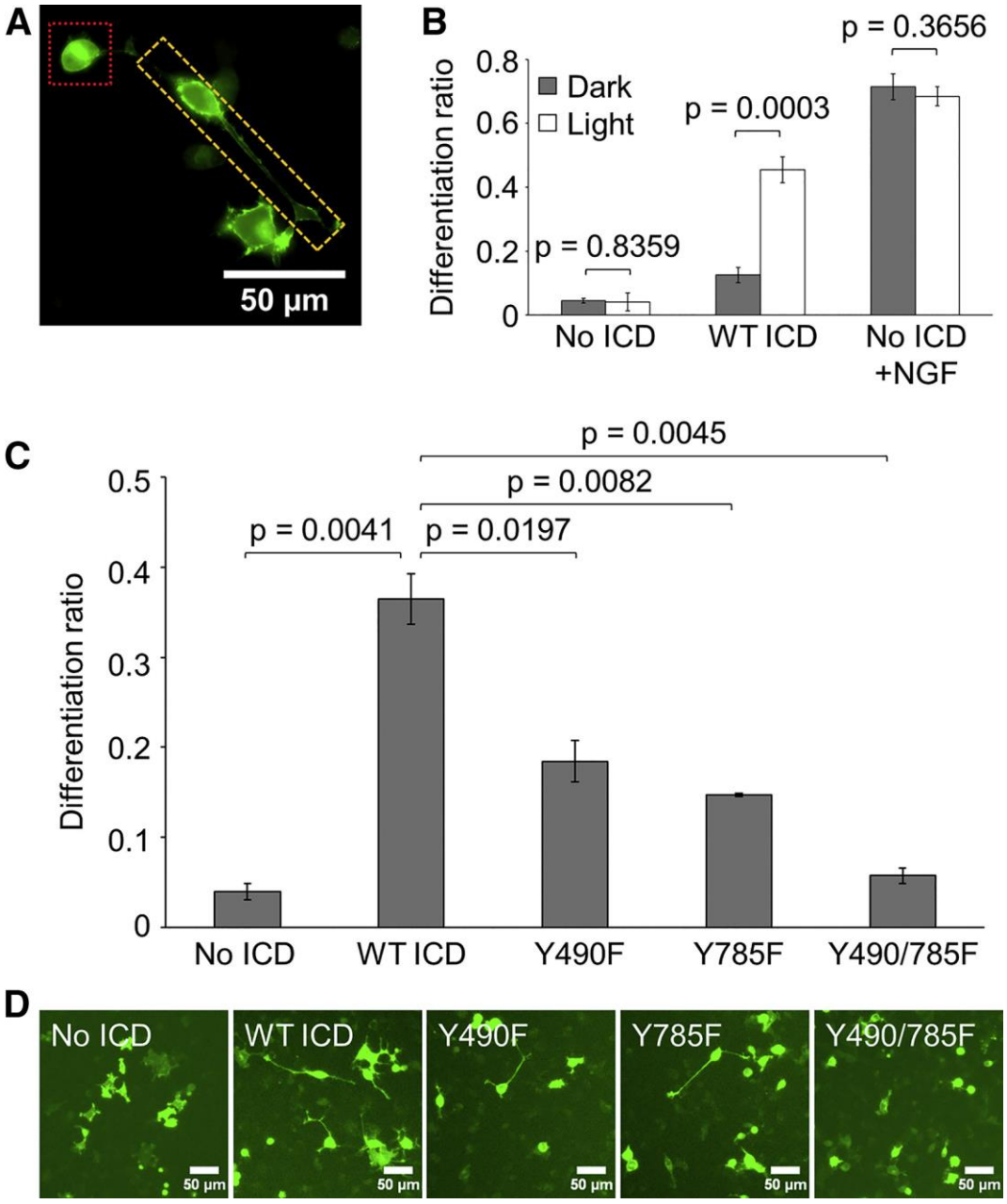

Figure 7. ***Optogenetic TrkA promotes PC12 cell differentiation in response to blue-light stimulation***. (A) Image for reference depicting differentiated (yellow box) and undifferentiated (red box) PC12 cells transfected with No ICD and treated with 50 ng/mL NGF for 24 hours. (B) Differentiation ratios calculated for PC12 cells expressing WT ICD or No ICD. Transfected cells were illuminated with 300 µW/cm^2 blue light or kept in the dark for 44 hours prior to imaging. WT ICD mediated significant light-induced differentiation compared to No ICD. Cells expressing No ICD in the presence of 50 ng/mL NGF underwent robust differentiation in a light-independent manner. Values represent the mean ± standard deviation of three biological replicates (n=3) with >70 cells counted per replicate. (C) Differentiation ratios calculated for PC12 cells expressing variants of the optogenetic TrkA system. Transfected cells were illuminated with 300 µW/cm^2 blue light for 24 hours prior to imaging. Y490F and Y785F

Figure 7 (cont.) showed a significant reduction in light-induced differentiation compared to WT ICD. Y490/785F resulted in a differentiation ratio similar to that of No ICD. Values represent the mean ± standard deviation of two biological replicates (n=2) with >900 cells counted per replicate. (D) Representative fluorescence images of the conditions reported in (C). Scale bar = 50 μm.

Light-induced optogenetic TrkA mutants differentially activate the ERK and PLCγ pathways

To interrogate the mechanism behind the reduced differentiation mediated by the optogenetic TrkA mutants, we performed western blots to probe the activity of downstream signaling pathways. To minimize baseline signaling activity and capture subtle differences between conditions, PC12 cells were transfected with mixtures of the variant ICD constructs and the No ICD construct. Cells were illuminated for 10 minutes with 5 mW/cm^2 blue light prior to lysis. Both Y490F and Y785F showed a significant reduction in ERK signaling compared to WT ICD, with the reduction for Y490F being more pronounced (Figure 8A, Lanes 4, 6, and 8). Cells expressing Y490F showed no change in light-induced PLCγ activity compared to WT ICD, while Y785F showed a complete loss of PLCγ activity (Figure 8B, Lanes 4, 6, and 8). These results indicate that Y490 primarily contributed to ERK activity, while Y785 primarily contributed to PLCγ activity. Additionally, Y785 seemed to partially contribute to ERK signaling as evidenced by the residual ERK activity observed for Y490F (Figure 8A, Lane 6) and the reduction in ERK activity observed for Y785F (Figure 8A, Lane 8) compared to WT ICD. To confirm that the observed variations in signaling were a result of specific mutations and not due to significant variability in system expression, lysates were probed with an anti-GFP antibody. All constructs were expressed at a comparable level (Figure 8C).

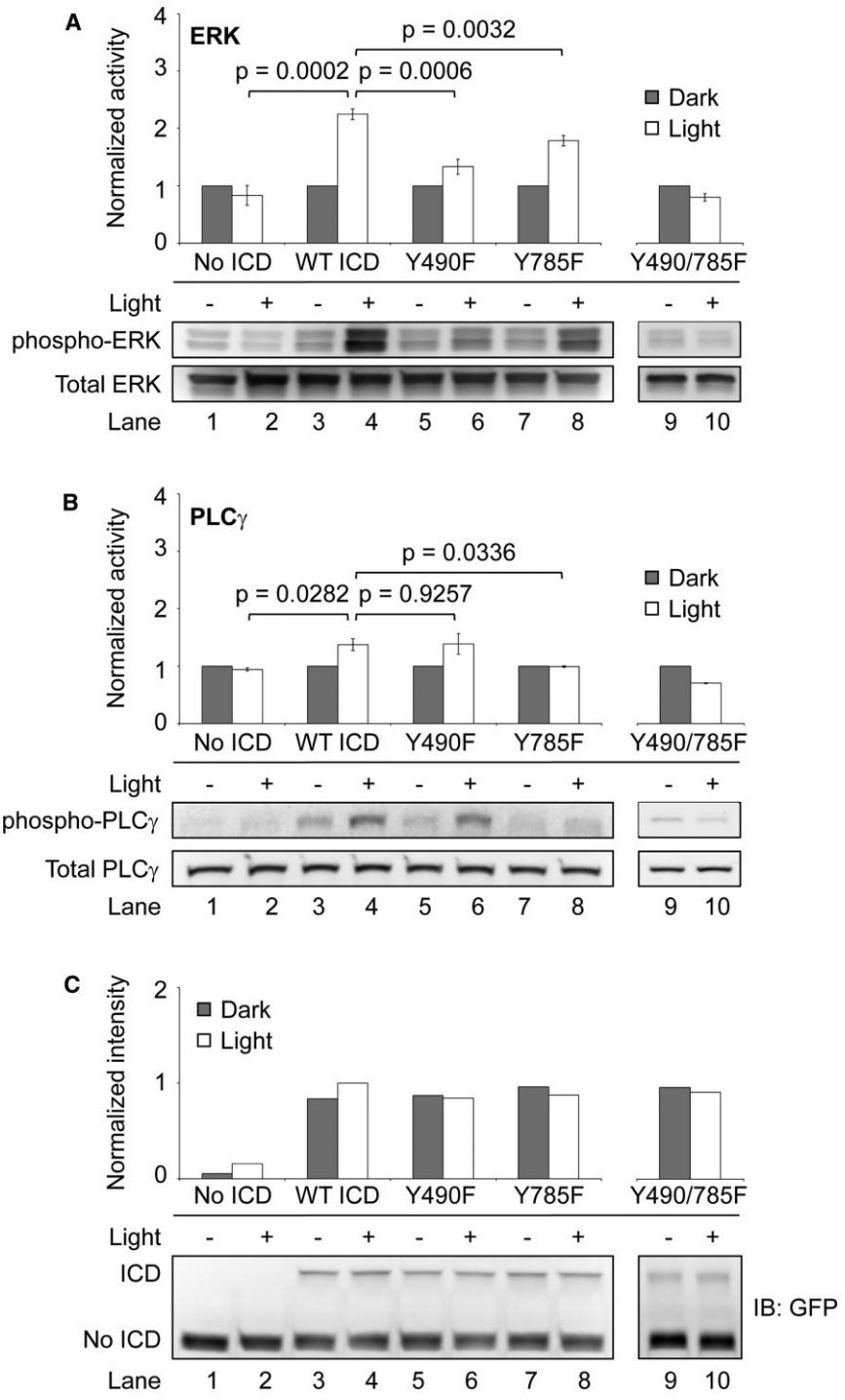

Figure 8. ***Light-induced optogenetic TrkA mutants differentially activate the ERK and PLCγ pathways***. Western blot analysis of light-induced (A) ERK and (B) PLCγ activity exhibited by PC12 cells expressing variants of the optogenetic TrkA system. Transfected cells were serum-starved overnight following transfection, and were illuminated with 5 mW/cm^2 blue light or kept in the dark for 10 minutes prior to lysis. Compared to WT ICD, Y490F displayed a dramatic reduction in ERK activity with no change in PLCγ activity. Y785F showed a relatively modest reduction in ERK activity with nearly abrogated PLCγ activity. Y490/785F showed no light-

Figure 8 (cont.) induced activity for either pathway, similar to No ICD. Values represent the mean ± standard deviation of three separate experiments (n=3) for ERK and two separate experiments (n=2) for PLCγ. (C) Western blot analysis of system expression by probing GFP. Expression level across samples fluctuates within 16%.

Y785 contributes to ERK signaling and PC12 cell differentiation in a PLCγ-PKC dependent manner

Given that Y785 is essential for PLCγ activity, we speculated that the contribution of Y785 to ERK signaling was mediated by pathway crosstalk. Indeed, findings from previous studies support this notion [212,213]. To validate this, we transfected PC12 cells as previously described with a combination of Y490F and No ICD. Transfected cells were then treated with a PLCγ inhibitor (U73122, 1 μM) or a PKC inhibitor (GF 109203X, 1 μM) 10 minutes prior to illumination. With the inhibitors still present, cells were then illuminated for 10 minutes with 5 mW/cm^2 blue light before lysis and subsequent immunoblotting (Figure 9A). Compared to untreated cultures, all cells treated with inhibitors displayed an abrogation of the light-induced residual ERK activity mediated by Y490F (Figure 9A, Lanes 2, 4, and 6), suggesting that the role of Y785 in ERK signaling is dependent on the PLCγ-PKC pathway. To confirm that the observed variations in signaling were not due to significant variability in system expression, lysates were probed with an anti-GFP antibody. All constructs were expressed at a comparable level (Figure 9B). In addition to interrogating the short-term effect of inhibitors on light-induced ERK signaling mediated by Y490F, we set out to determine the effect of long-term inhibition on PC12 cell differentiation. PC12 cells overexpressing Y490F were illuminated with blue light (300 μW/cm^2) for 24 hours in the presence or absence of U73122 (1 μM) or GF 109203X (1 μM). Inhibitors were added 1 hour prior to illumination. Cell cultures treated with either inhibitor

showed significantly reduced differentiation, suggesting that Y785 also contributes to PC12 cell differentiation in a PLCγ-PKC dependent manner (Figure 9 C-D).

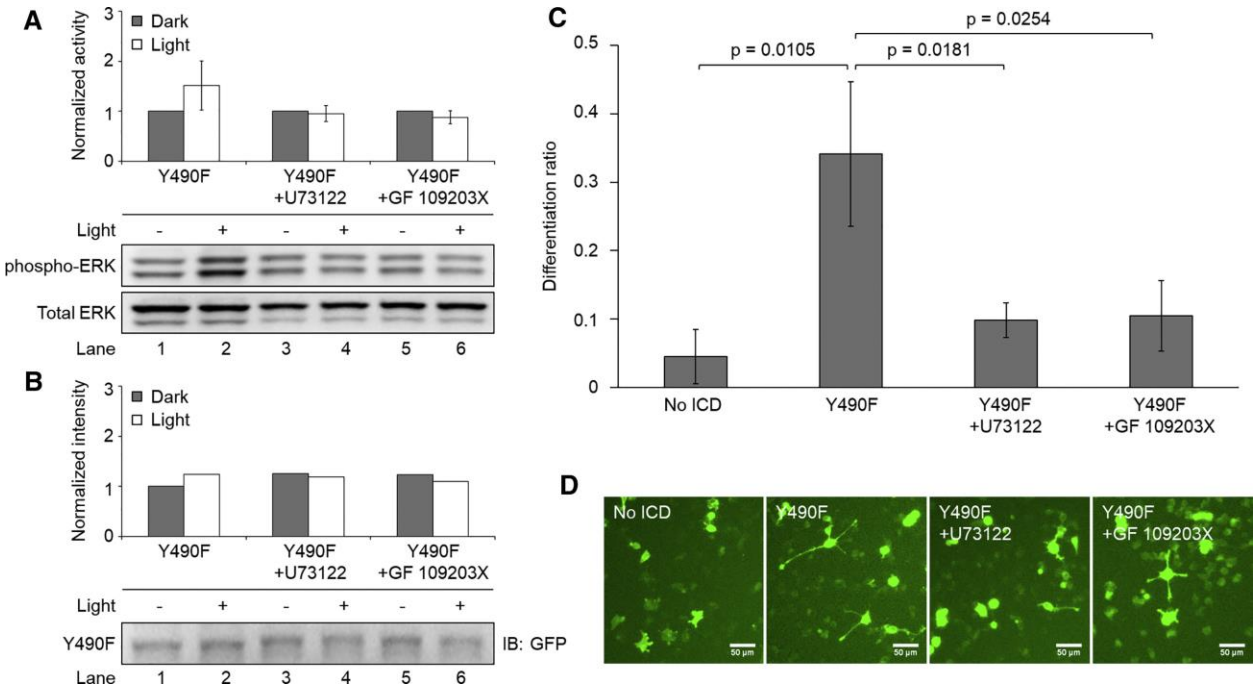

Figure 9. ***Y490F-mediated ERK signaling is abolished by PLCγ-PKC inhibitors***. (A) Western blot analysis of light-induced ERK activity exhibited by PC12 cells expressing Y490F. Transfected cells were serum-starved overnight following transfection and were treated with a PLC*γ* inhibitor (U73122, 1 μM) or a PKC inhibitor (GF 109203X, 1 μM) for 10 minutes prior to illumination. Cells were subsequently illuminated with 5 mW/cm^2 blue light or kept in the dark for 10 minutes prior to lysis. Cells treated with U73122 or GF 109203X had abolished light-induced ERK activity compared to the untreated control. Values represent the mean ± standard deviation of two separate experiments (n=2) for untreated, and four separate experiments (n=4) for U73122 and GF 109203X. (B) Western blot analysis of system expression by probing GFP. Expression level for illuminated conditions fluctuates within 14%. (C) Differentiation ratios calculated for PC12 cells expressing Y490F in the presence of U73122 (1 μM) or GF 109203X (1 μM). Inhibitors were added to cells 1 hour prior to illumination. Cells were illuminated with 300 μW/cm^2 blue light for 24 hours prior to imaging. Cells treated with U73122 or GF 109203X had decreased light-induced differentiation compared to the untreated control, which received inhibitor vehicle (DMSO). Values represent the mean ± standard deviation of three biological replicates (n=3) with >40 cells counted per replicate (D) Representative fluorescence images of the conditions reported in (C). Scale bar = 50 μm.

Discussion

We developed an optogenetic TrkA system to study differentiation in PC12 cells by photo-activation of the TrkA ICD and its downstream signaling pathways. Light-mediated homo-association of TrkA resulted in elevated ERK and PLCγ activity. Light stimulation specifically activated the optogenetic TrkA, efficiently decoupling its signaling from endogenous TrkA and p75NTR. By generating mutants of the signal pathway-specific tyrosines, Y490 and Y785, we used this system to determine the mechanisms by which TrkA regulates PC12 cell differentiation. In a previous study, we demonstrated that optogenetic activation of Raf/MEK/ERK signaling is sufficient to induce PC12 cell differentiation, suggesting that this pathway is a strong correlating factor for the phenotype [116]. From our experiments employing optogenetic TrkA mutants in combination with pathway-specific inhibitors, we propose a model of the TrkA signaling network in the context of PC12 cell differentiation (Figure 10). We find that Y490 regulates ERK signaling and Y785 primarily regulates PLCγ signaling. Y785 also promotes ERK signaling in a PLCγ-PKC-dependent manner. Indeed, previous studies showed that PKC could feed into the Raf/MEK/ERK signaling cascade [212,213]. The reduced differentiation caused by the Y490F and Y785F single mutants, and the abolished differentiation observed for the Y490/785F double mutant, suggest that TrkA uses both Y490 and Y785 to activate Raf/MEK/ERK signaling to promote PC12 cell differentiation.

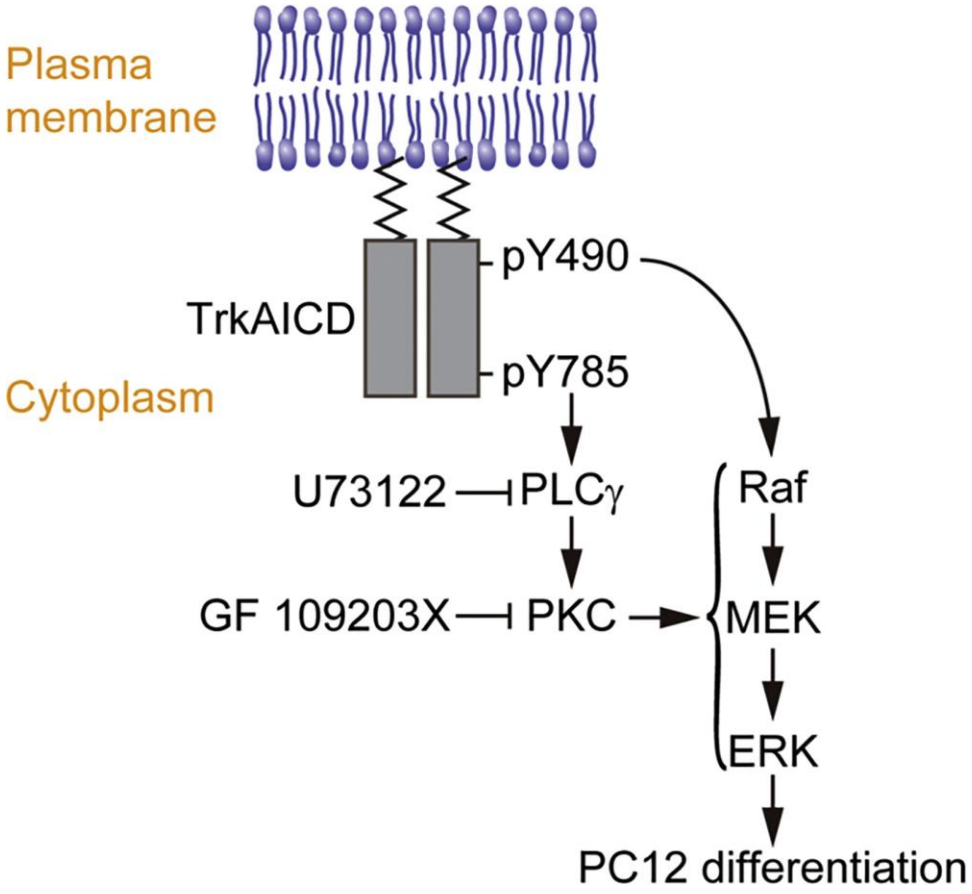

Figure 10. ***Proposed model for the role of Y490 and Y785 in TrkA-mediated PC12 cell differentiation***. The Raf/MEK/ERK signaling cascade, primarily instigated by Y490 of TrkA, is essential for PC12 cell differentiation. Y785 instigates the PLCγ-PKC pathway, which feeds into the Raf/MEK/ERK signaling cascade. Mutating Y785 or inhibiting the PLCγ-PKC pathway results in diminished receptor-mediated ERK signaling and differentiation in PC12 cells.

Based on previous studies [192,193], PC12 cells expressing the Y490/785F double mutant did not differentiate in the presence of NGF, in agreement with our optogenetic result. However, the individual contribution of Y490 and Y785 to PC12 cell differentiation has been elusive. In one case, expression of single mutants Y490F and Y785F did not affect NGF-induced PC12 cell differentiation, suggesting a redundancy in their phenotypical role [192]. In the other case, Y490F resulted in a dramatic loss of differentiation while Y785F had no effect [193]. This discrepancy may be due to the nature of the ligands (i.e., NGF versus PDGF) used in these studies.

Using our optogenetic TrkA system, we show that Y490 and Y785 make significant and additive contributions to PC12 cell differentiation. We found that Y490F and Y785F each diminished PC12 cell differentiation to approximately half of that promoted by WT ICD (Figure 7C). A similar additive trend was observed for their capacity to activate ERK (Figure 8A). Stephens and colleagues [192] observed a similar reduction of ERK activity for both Y490F and Y785F compared to wild-type TrkA. At the phenotypic level, however, Y490F and Y785F promoted a degree of PC12 cell differentiation comparable to that promoted by wild-type TrkA. These results indicate that an ERK signaling threshold exists for establishing maximal differentiation. It is possible that this threshold was exceeded by both Y490F and Y785F when stimulated with NGF. Here, we note that PC12 cell differentiation mediated by WT ICD was less than that of NGF treatment (Figure 7B). We speculated that this was a result of a difference in signaling intensity between ligand- and light-simulated receptors. To test this idea, we compared the ERK activity induced by WT ICD (Figure 11A) to NGF treatment (Figure 11B). Given that not all cells are light-responsive in transfected cultures, we defined the signaling response of optogenetic TrkA as $S_{optoTrkA} = \frac{\mathrm{R(light,WT\ ICD)-R(light,No\ ICD)}}{\mathrm{R(dark,WT\ ICD)-R(dark,No\ ICD)}}$. We defined the NGF signaling response of untransfected cells as $S_{NGF} = \frac{\mathrm{R(NGF)}}{\mathrm{R(No\ NGF)}}$. R is the signal ratio of phosphorylated ERK over total ERK probed by western blot. Figure 7 A-B shows that light elicited a milder signaling response ($S_{optoTrkA} = 6.2$) compared to NGF treatment ($S_{NGF} = 9.2$). This result suggests that NGF elicits higher ERK activity than WT ICD, at least on a short time scale (5-10 minutes). To determine if a similar signaling difference exists at a longer time scale, we compared the ERK activity generated by NGF and light-activated WT ICD after 4 hours and 24 hours of treatment. As expected, NGF promoted higher ERK activity than WT ICD at both time points (Figure 11C).

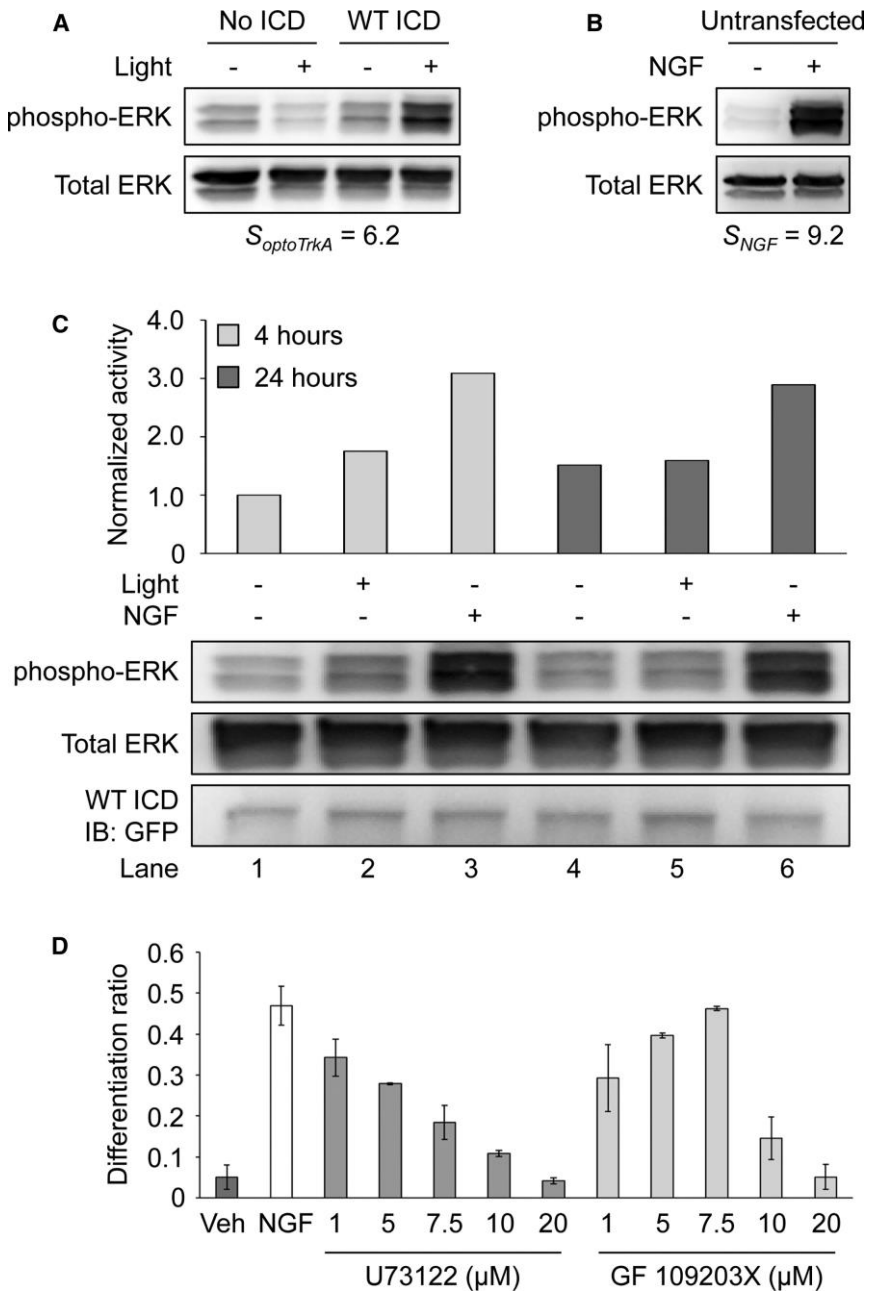

Figure 11. ***NGF elicits higher ERK activity compared to optogenetic TrkA and NGF-mediated PC12 cell differentiation is reduced by pharmacological inhibition of PLCγ and PKC in a dose-dependent manner.*** (A) Western blot analysis of two separate experiments. Transfected cells (No ICD and WT ICD) were serum-starved overnight following transfection. Cells were illuminated with 5 mW/cm^2 blue light or kept in the dark for 10 minutes prior to lysis. (B) Untransfected cells were serum-starved overnight prior to treatment. Cells were untreated or treated with NGF (100 ng/mL) for 5 minutes prior to lysis. The ERK activity mediated by optogenetic TrkA was lower than that of NGF. (C) Western blot analysis of ERK signaling mediated by long-term NGF or WT ICD activity. PC12 cells were transfected with WT ICD and serum-starved overnight following transfection. Cells were then kept in the dark, illuminated with 300 μW/cm^2 blue light, or treated with NGF (50 ng/mL) for 4 or 24 hours prior to lysis.

Figure 11 (cont.) Untreated cells received NGF vehicle (sodium acetate). NGF stimulation elicited higher ERK activity than WT ICD for both durations. All samples are normalized to Lane 1. (D) Differentiation ratios for PC12 cells treated with NGF in the presence of U73122 or GF 109203X. Serum-starved cells were treated with inhibitors (1, 5, 7.5, 10, and 20 μM) 1 hour prior to NGF treatment. Cells were treated with NGF (50 ng/mL) for 24 hours. Cells were stained with 1 μM Calcein AM 10 minutes before imaging. NGF-induced PC12 cell differentiation was reduced by U73122 or GF 109203X in a dose-dependent manner. Untreated cells received NGF vehicle (sodium acetate) and inhibitor vehicle (DMSO). Values represent the mean ± standard deviation of two biological replicates (n=2) with >400 cells counted per replicate.

Thus, the previously observed reduction of ERK activity for NGF-treated PC12 cells expressing either Y490F or Y785F may still surpass the signaling threshold required for saturated differentiation, thereby obscuring the contribution of individual tyrosines [192]. On the other hand, the optogenetic Y490F and Y785F likely produce a sub-threshold ERK activity when stimulated with light, providing advantages in interpreting the phenotypic role of each tyrosine. These results suggest that the difference between light- and ligand-induced PC12 cell differentiation resulted from their distinct potency in the induction of ERK signaling, the reason for which has yet to be determined, although it can be speculated that p75NTR plays a role in the presence of the ligand. In the physiological context, while Y490 primarily mediates the ERK-dependent trophic effects of NGF, we speculate that the role of Y785 in ERK signaling becomes more critical where NGF concentrations are low.

Finally, we asked if pharmacological inhibition of NGF-induced PLCγ-PKC activity would support our proposed model of the TrkA signaling network in the context of PC12 cell differentiation. We performed a differentiation assay in the presence of U73122 or GF 109203X. As expected, NGF-induced differentiation was reduced by both inhibitors in a dose-dependent manner, supporting our previous finding that the PLCγ-PKC axis contributes to PC12 cell differentiation (Figure 11D).

Optogenetic activation of TrkA provides an attractive approach to dissect NGF signaling processes by leaving the endogenous TrkA expression unperturbed and by bypassing p75NTR signaling. As we have demonstrated, optogenetics can also be applied together with conventional inhibitor-based assays to further delineate signaling mechanisms. Although this work has primarily focused on delineation of TrkA signaling in mammalian cells, utilization of this optogenetic TrkA system in multicellular organisms should be applicable. Indeed, recent work from multiple laboratories including our own has demonstrated optogenetic control of intracellular signaling pathways in drosophila [105,118], zebrafish [74,148], Xenopus [116], and mice [101,149,214,215]. Notably, *in vivo* application of optogenetics has been significantly improved by the utilization of novel nanometer materials, such as upconversion nanoparticles [100,160,161,216], to convert near-infrared light to visible light and facilitate deep-tissue light delivery. As receptor tyrosine kinase activation is a common function for a variety of growth factors and cytokines, we expect that this strategy can be generalized to study other receptor-mediated signal transduction pathways.

Significance

Cell fate is largely determined by integrating and processing a variety of signaling inputs from the environment. To effectively and precisely transmit extracellular signals into the cell, delicate signaling machinery is required. Transmembrane receptors serve as the major machinery for transducing membrane-impermeant extracellular signals. In some cases, one type of ligand may bind to a variety of receptors to elicit distinct signaling outcomes. The signaling mechanisms of these receptors are often confounded particularly where common downstream signaling pathways are activated. In these cases, mechanistic delineation of the signaling

mediated by each type of receptor calls for a strategy that can successfully decouple receptor activity. Nerve growth factor is one such ligand that interacts with both its high-affinity and low-affinity receptors, TrkA and p75NTR, both of which activate the extracellular-signal-regulated kinase pathway. To delineate TrkA subcircuits from those of p75NTR, we developed an optogenetic system where light was used to specifically activate TrkA signaling in the absence of nerve growth factor. By combining optogenetics with pharmacological assays, we demonstrated that the tyrosine residues Y490 and Y785 of the TrkA intracellular domain each contributes to PC12 cell differentiation through the extracellular-signal-regulated kinase pathway in an additive manner. Because receptor tyrosine kinase signaling is involved in neurological disorders, development, and cancer, we believe that delineating the signaling outcomes of TrkA subcircuits could lead to new insights into pathological conditions.

Acknowledgments

We thank Prof. Tobias Meyer at Stanford University for providing the PC12 cell line and Dr. Jun-Lin Guan at University of Cincinnati for MDA-MB-231 cells. We thank Prof. Erik Procko at the University of Illinois at Urbana-Champaign for providing split Venus plasmids. We thank Dr. Sandra McMasters from the cell media facility at the University of Illinois at Urbana-Champaign for providing DH5α competent cells. Kai Zhang thanks the funding support from University of Illinois at Urbana-Champaign. Jiajie Diao thanks the support from National Institutes of Health (R35GM128837).

CHAPTER 3: SINGLE-MOLECULE ANALYSIS OF FLUORESCENT CARBON DOTS BY TIRF MICROSCOPY

This work contains previously published material[*†]

Abstract

Carbon dots are an attractive nanomaterial in cell and molecular biology because of their biocompatibility and luminescence properties. To guide particle development for use in varying biological assays, an understanding of particle photophysics is required. Although bulk-state measurements provide some insight on particle behavior, single-molecule analysis proves useful in precisely characterizing the photophysical properties of carbon dots. Here, we report the single-molecule analysis of carbon dots by total internal reflection fluorescence microscopy. This work was performed in collaboration with the laboratory of Dr. Dipanjan Pan in the Department of Bioengineering at the University of Illinois at Urbana-Champaign. The Pan Laboratory synthesized and provided the carbon dots.

[*] Misra, S.K., Srivastava, I., **Khamo, J.S.**, Krishnamurthy, V.V., Sar, D., Schwartz-Duval, A.S., Soares, J.A.N.T., Zhang, K., and Pan, D.P.J. (2018). Carbon dots with induced surface oxidation permits imaging at single-particle level for intracellular studies. Nanoscale 10, 18510-18519.

[†] Fathi, P., **Khamo, J.S.**, Huang, X., Srivastava, I., Esch, M.B., Zhang, K., and Pan, D.P.J. (2019). Bulk-state and single-particle imaging are central to understanding carbon dot photophysics and elucidating the effects of precursor composition and reaction temperature. Carbon 145, 572-585.

The analysis of carbon dots synthesized in the presence of N-methyl morpholine-N-oxide

In this work, mutli-color carbon dots (CDs) were synthesized using sucrose as the carbon source in the presence of N-methyl morpholine-N-oxide (NMMO). NMMO is a mild oxidant that mediates the nanoscale surface oxidation of CDs to enhance particle brightness and trigger luminescence tuning (Figure 12). Resulting CDs were fractionated by emission wavelength using chromatographic separation. Four fractions were isolated: blue (CD-NMMO-B), green (CD-NMMO-G), yellow (CD-NMMO-Y), and red (CD-NMMO-R). To compliment the bulk-state measurements performed by the Pan Lab, we analyzed these CDs at the single-molecule level by using total internal reflection fluorescence (TIRF) microscopy.

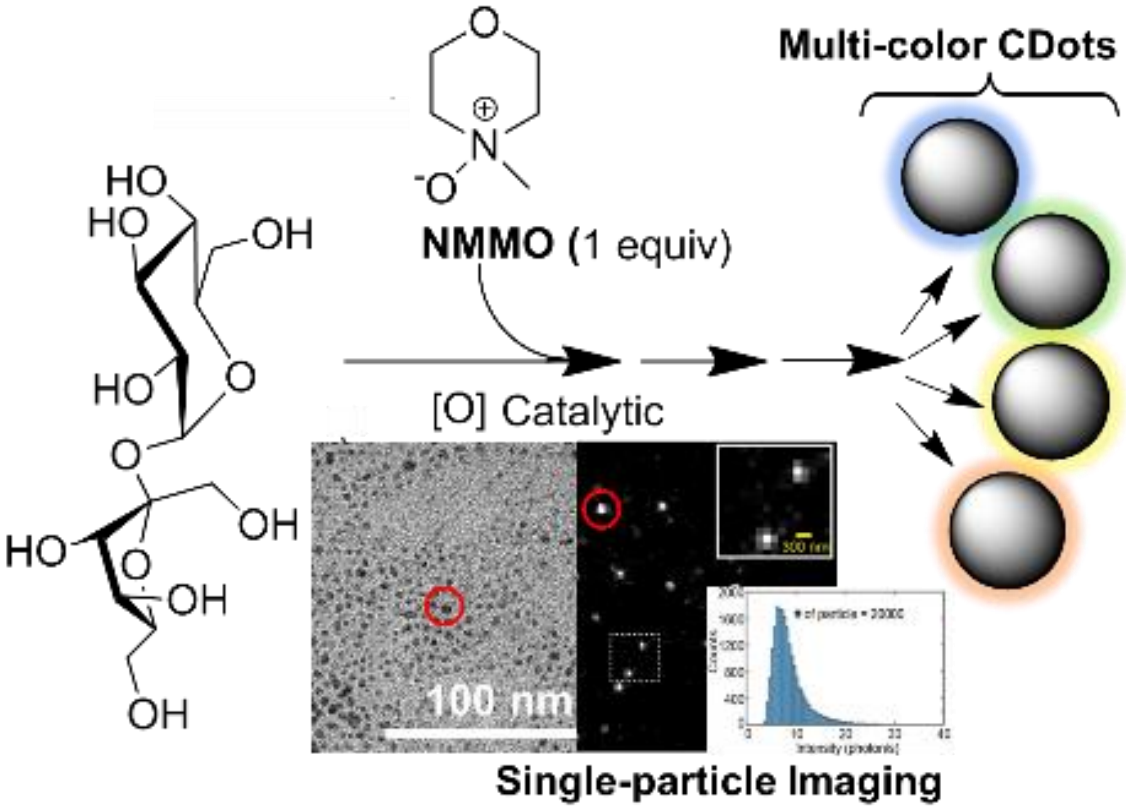

Figure 12. Separated fractions of carbon dots having induced surface oxidation allows imaging at single-particle level and can be used for intracellular studies.

For single-particle imaging, we deposited 40 μL of solutions containing CDs or CD-NMMOs to each cavity (1 mm in diameter) of a polydimethylsiloxane (PDMS) chamber (Figure 13A). Such a device allows for detection of multiple types of particles on the same substrate. The sample was diluted in water so that 500 particles were detected within an 80 μm × 80 μm field of view. A home-built TIRF microscope equipped with a 488 nm, a 100× oil-immersion objective, and an electron multiplying Charge-Coupled Device (EMCCD) was used to image individual particles. Individual particles were detected as bright diffraction-limited spots (Figure 13B). The excitation power was 1.5 mW at the back aperture of the objective. Similar images were obtained from CD-NMMO-B (Figure 13C), CD-NMMO-Y (Figure 13D), CD-NMMO-G (Figure 13E) and CD-NMMO-R (Figure 13F) samples. The excitation power was 1.5 mW at the back aperture of the objective. A control with solvent (water) alone was measured to confirm that the signal was indeed resulting from the CDs. As shown in the Figure 13G, there are significantly less, if any, particles that can be detected for this negative control. Ten time-stamped images of 600 frames were then taken for each field of view. With a dynamic frame transfer mode turned on, transfer time between sequential frames is about 1 ms, which makes the total trajectory time slightly longer than 60 sec with a 100 ms exposure time.

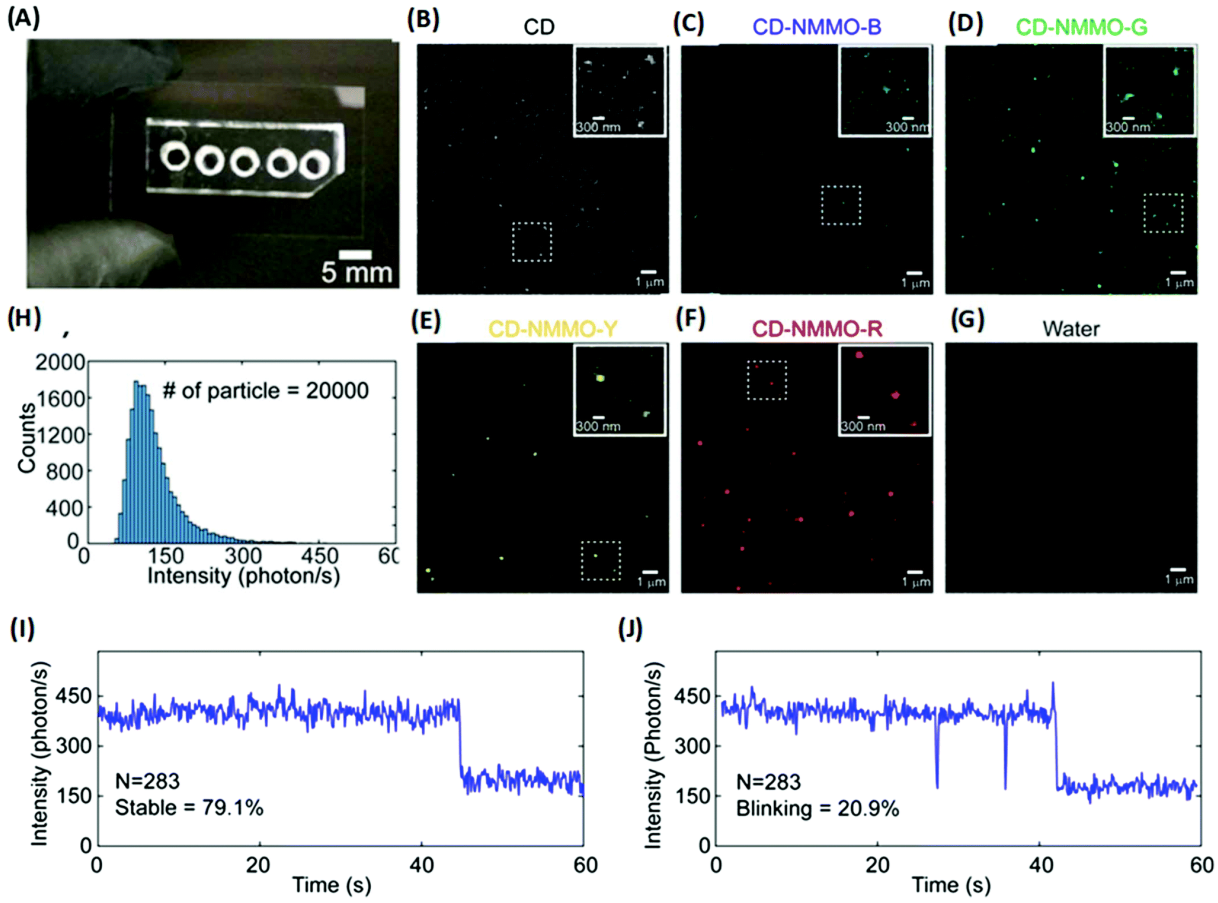

Figure 13. ***Single particle imaging of CD-NMMO and its fractions CD-NMMO-B, CD-NMMO-G, CD-NMMO-Y, and CD-NMMO-R***. (A) A home-made micro-cavity device used in single-particle imaging. Up to five samples can be imaged on the same coverslip. Representative single-particle emission images of (B) CD-NMMO, (C) CD-NMMO-B, (D) CD-NMMO-Y, (E) CD-NMMO-G and (F) CD-NMMO-R as captured by an EMCCD camera. Inset: Individual particles form diffraction-limited images and (G) A snapshot of a sample without CDs (control). (H) A histogram of emission intensity from 20,000 single CD-NMMOs. (I, J) Representative intensity trajectories from single CD-NMMOs, which show a typical single-step photo bleaching. Out of 283 CD-NMMOs, approximately 80% displayed stable trajectory (I) and 20% displayed transient blinking (J).

The intensity of each particle was analyzed by a Matlab script that allows for semi-automatic detection of bright spots [217]. Because CD-NMMOs' emission properties depend on molecules on their surface, we did not apply any chemical-conjugation strategy to immobilize these particles on the glass surface. This would not affect measurement of the brightness at the single-particle level because the evanescent field used in TIRF microscopy only excites particles

localized within 200 nm distance from the surface. For particles diffusing away from the focus during image acquisition, their intensities were then calculated by averaging all frames over their prior surface-dwelling time. The representative distribution of individual CD-NMMO particle intensity is shown in Figure 13H. For the majority of nanoparticles, we observe a flat emission trajectory with minimal photo-blinking (Figure 13I). To determine the photostability and photo blinking of individual CD-NMMOs, images were collected using an acquisition time of 600 frames (60 s). This helped us detect a single-step bleaching behavior. Results from 283 particles indicated 80% displayed flat trajectories (Figure 13I) and 20% displayed transient blinking lasting less than 1 s (Figure 13J).

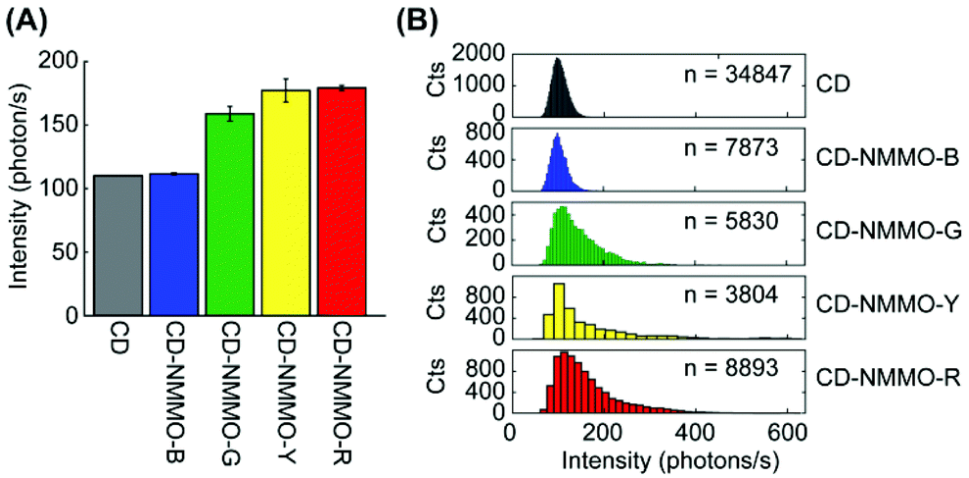

Figure 14. ***Single particle analysis of CD-NMMO fractions***. (A) Single-particle analysis of the brightness of each fraction of CD-NMMO and CD alone. (B) The histogram shows intensity distribution of each fraction of particles. Green, yellow, and red fractions show extended peak shift to the right (brighter). This extension indicates appearance of particles with enhanced fluorescence at single particle level.

To quantitatively determine the brightness of particles in each fraction (CD-NMMO-B, CD-NMMO-G, CD-NMMO-Y and CD-NMMO-R), we performed single-particle imaging for each fraction (Figure 14). Within the emission spectrum window (500-550 nm & 585-635 nm),

the yellow and red fractions appeared brighter than the blue and green fractions as well as CD alone. This result confirmed that particles in the yellow and red fractions exhibit significant red-shift in their emission peak and enhancement of single-particle brightness compared with pristine

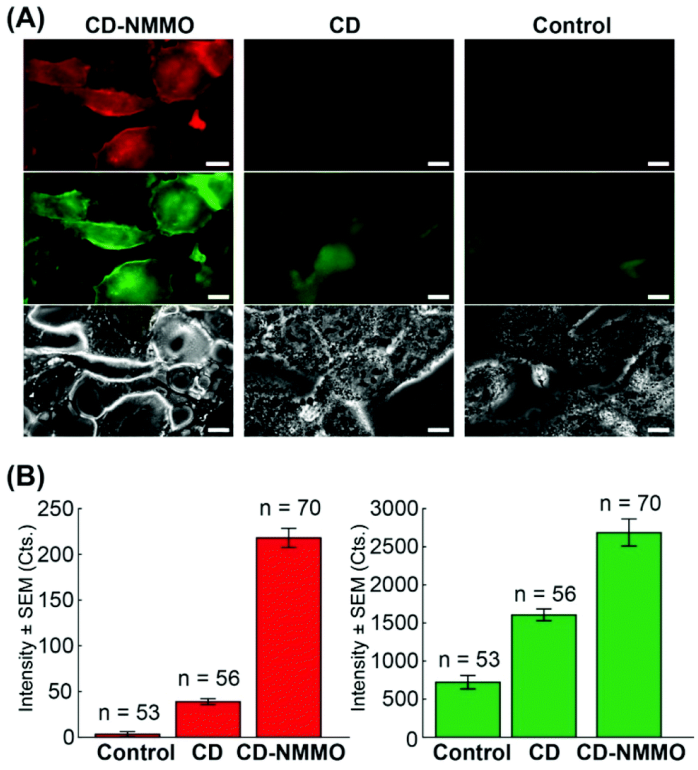

Figure 15. ***Intracellular single particle imaging of CD-NMMOs compared with CDs***. (A) Fluorescence measurement of C32 cells incubated with CD-NMMO (left), CD (middle), and no particles (right). Cells were incubated with or without particles, fixed on coverslip, and imaged with epi-fluorescence microscopy. The dynamic range for each of the three images in the red (top) and green (middle) channels were identical. CD-NMMO incubated cells show significantly brighter images. (B) Quantification of cell brightness in both red (left) and green (right) fluorescence channels. The base level from control may arise from auto fluorescence of cells. The number of cells (n) analyzed in each condition was marked above each bar. For the green channel, the excitation wavelength was 450-490 nm and emission wavelength was 500-550 nm. For red channel, the excitation wavelength was 540-580 nm and emission wavelength was 600-675 nm.

Intracellular emission features of CD-NMMOs were investigated in C32 mammalian cells (model human melanoma cells). Cells were incubated with CD-NMMOs (1 mg/mL) for 4 h

before fixation with 4% paraformaldehyde. Cells incubated with CDs or with no particles were used as negative controls (Figure 15). Cells incubated with CD-NMMO showed strongest emission in both green and red channels (Figures 15A and 16), indicating the presence of CD-NMMO's with different wavelength emissions. For the green channel, the excitation wavelength was 450-490 nm and emission wavelength was 500-550 nm. For red channel, the excitation wavelength was 540-580 nm and emission wavelength was 600-675 nm. Considering the relative strong cellular auto-fluorescence in the green channel, we believe red channel is a better choice for intracellular imaging with CD-NMMOs (Figure 15B).

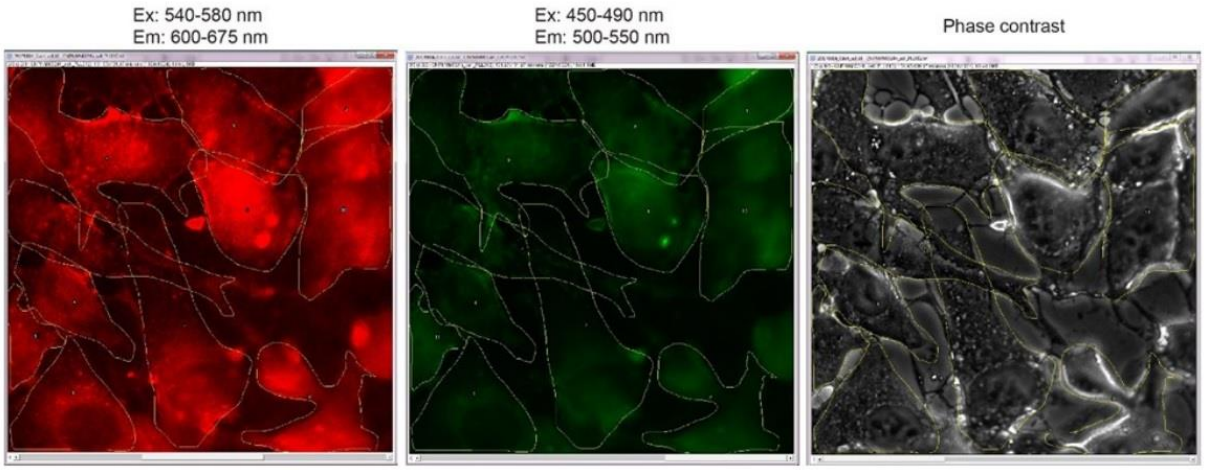

Figure 16. ***Single-cell image analysis of C32 cells incubated with CD-NMMO***. For each field of view, three channels (Red, Green, Phase Contrast) were used to capture cell image. The region of interest *(ROI) Manager* plugin from FIJI was used to analyze the correlation of fluorescence intensities for each channel.

We also examined the intracellular imaging capacity for each of the fractions of CD-NMMO. Cells were prepared with the same protocol as mentioned above. We found equally efficient CD-NMMO-B, CD-NMMO-G, CD-NMMO-Y, and CD-NMMO-R fractions in DAPI, GFP, TX2 and Y5 regions, respectively (Figure 17). Because autofluorescence raises the

baseline of fluorescence within the intracellular environment, this work does not cover the scope of exploring single-particle imaging within live cells. Ongoing collaborative works in our laboratories involve further modification of particle synthesis and imaging technique to enhance the signal-to-background ratio of single-particle imaging. Results from these studies will be published in the near further.

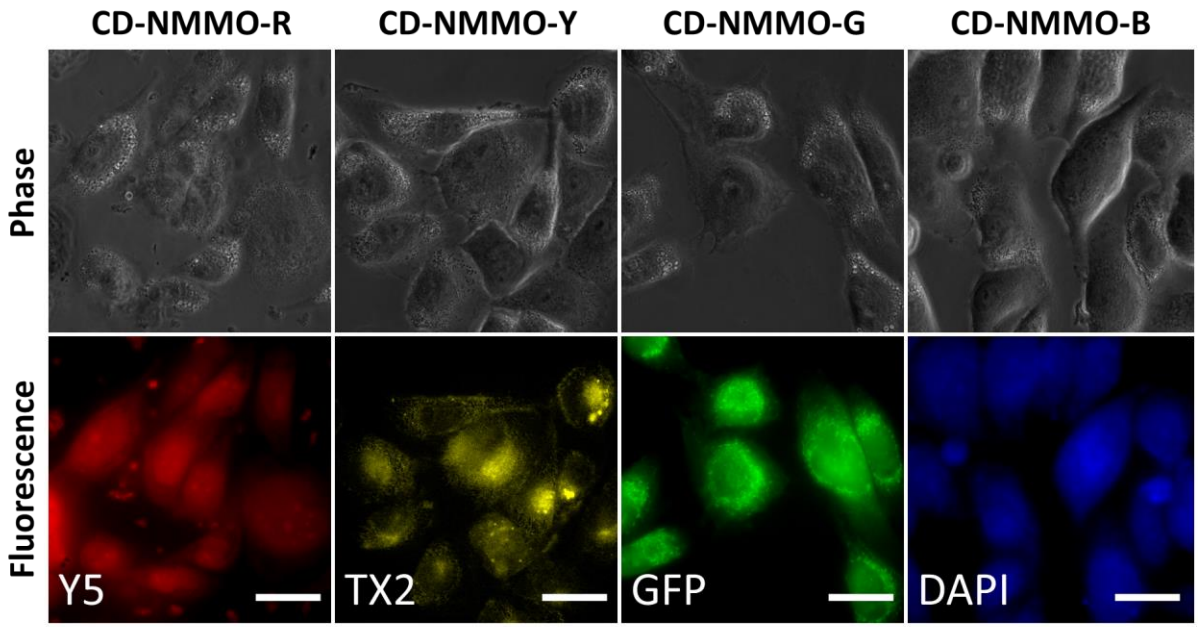

Figure 17. ***Intracellular image analysis of C32 cells incubated with different fractions of CD-NMMO***. Images of cells treated with CD-NMMO-B, CD-NMMO-G, CD-NMMO-Y, and CD-NMMO-R acquired under DAPI, GFP, TX2 and Y5 regions, respectively. For each field of view, two channels (Color and Phase Contrast) were used to capture cell image. The region of interest *(ROI) Manager* plugin from FIJI was used to analyze the correlation of fluorescence intensities for each channel. Scale bar is 30 µm.

The analysis of carbon dots synthesized using different carbon sources and temperatures

In this work, CDs were synthesized using four different carbon sources as precursors (α-d-Glucose 1-phosphate dipotassium salt hydrate, β-d-Glucosamine pentaacetate, D-glucuronic acid, and sucrose) at two different synthesis temperatures (200 °C or 150 °C). These CDs were

spectroscopically analyzed using bulk-state and single molecule techniques to determine the effects of synthesis temperature and carbon source on the photophysical properties of CDs (Figure 18). TIRF microscopy was used to acquire single-molecule data, as reported below.

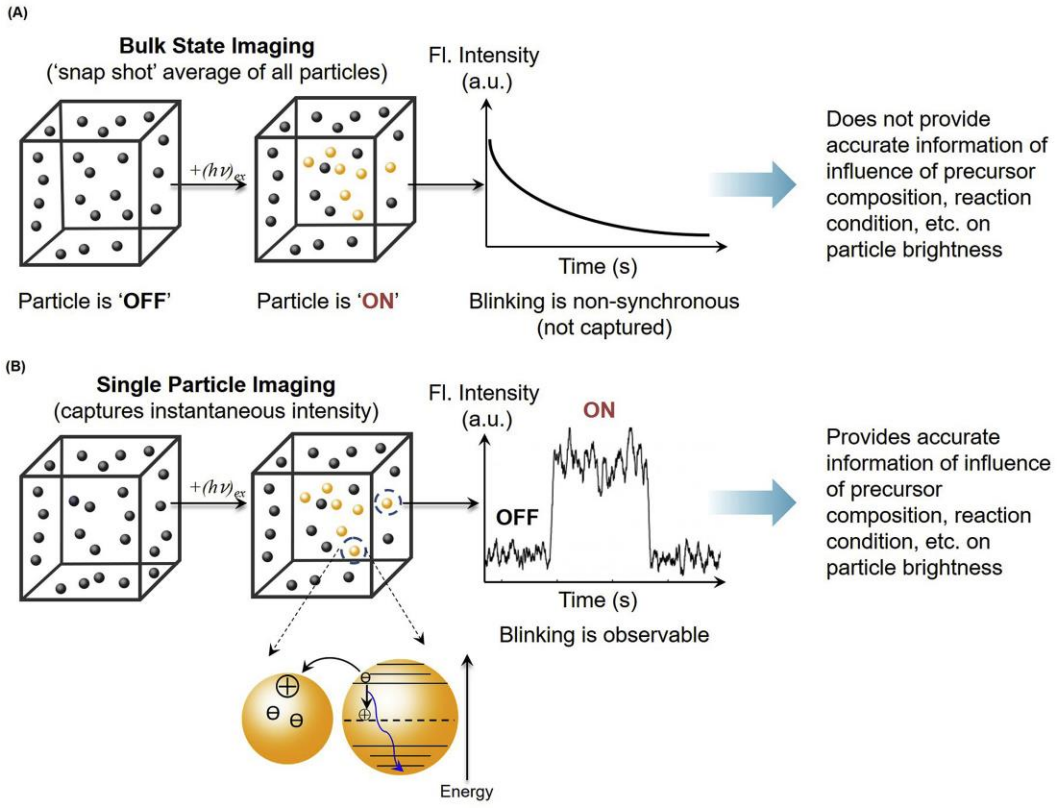

Figure 18. ***Bulk state vs. single particle imaging***. (A) Bulk state imaging provides a snap shot average of all particles in the sample. The particle blinking in the bulk sample is non-synchronous, leading to a lack of information about the influence of temperature and composition on particle brightness. (B) Single particle imaging captures information about the instantaneous intensity of individual particles, allowing for evaluation of particle brightness based on individual particle "on" and "off" characteristics.

Interpreting particle brightness by single-particle imaging analysis

Bulk measurements of each type of CD showed that they display a wide range of particle brightness. To better understand their photophysics, we proceeded to analyze single-particle imaging data. By employing a change point data analysis algorithm [218,219], we parsed individual

trajectories of each type of particle into “on” and “off” segments. The “on” segment was defined by intensity thresholding with the mean value of the darkest segment plus three times the standard deviation of that segment.

We first determined if different precursor materials and temperatures affect particle brightness. There are two parameters that can be used to quantify particle brightness: 1) the instantaneous brightness, which is the mean value of intensity in all the “on” segments, and 2) the on-time duty cycle, which determines the probability of a particle staying in the emissive state during the data acquisition time. We first calculated the instantaneous particle intensity (Figure 19A). Although different particles showed different instantaneous intensities, their variation is much less than those measured in bulk. This result indicates that, before photobleaching, each type of particle has a comparable capacity in emitting photons, an observation that seems to contradict the bulk fluorescence measurement.

We then further determined the on-time duty cycle of each type of particle. Different particles displayed a variety of on-time duty cycles, with the largest duty cycle (20%, β-D-gluc at 200 °C) almost doubling the smallest one (9%, d-glucuronic acid, 200 °C). We reason that fluorescence intensity measured by bulk measurement is determined by both the instantaneous intensity and the on-time duty cycle. Indeed, if both factors are considered, the product of instantaneous intensity and on-time duty cycle (Figure 19B) much better resembles the bulk fluorescence measurement.

Consideration of both the instantaneous intensity and on-time duty cycle helped us better understand the photophysics of different types of particles. For instance, β-D-gluc 200 °C displayed the largest instantaneous intensity, as well as the largest on-time duty cycle, therefore standing out as the brightest type of particle, consistent with the bulk measurement. On the other

hand, although sucrose 150 °C, β-D-gluc 150 °C, and α-D-gluc 200 °C CDs show a similar instantaneous intensity, the on-time duty cycle of sucrose 150 °C CDs is only 9%, much less than that of β-D-gluc 150 °C (15%) or α-D-gluc 200 °C (14%). Consequently, sucrose 150 °C CDs are dimmer than β-D-gluc 150 °C or α-D-gluc 200 °C CDs. Thus, single-particle imaging allows for delineation of photophysical mechanisms underlying CD emission. In general, the intensity at different synthesis temperatures within the same precursor remains comparable, whereas the intensity difference is more significant between different precursor materials.

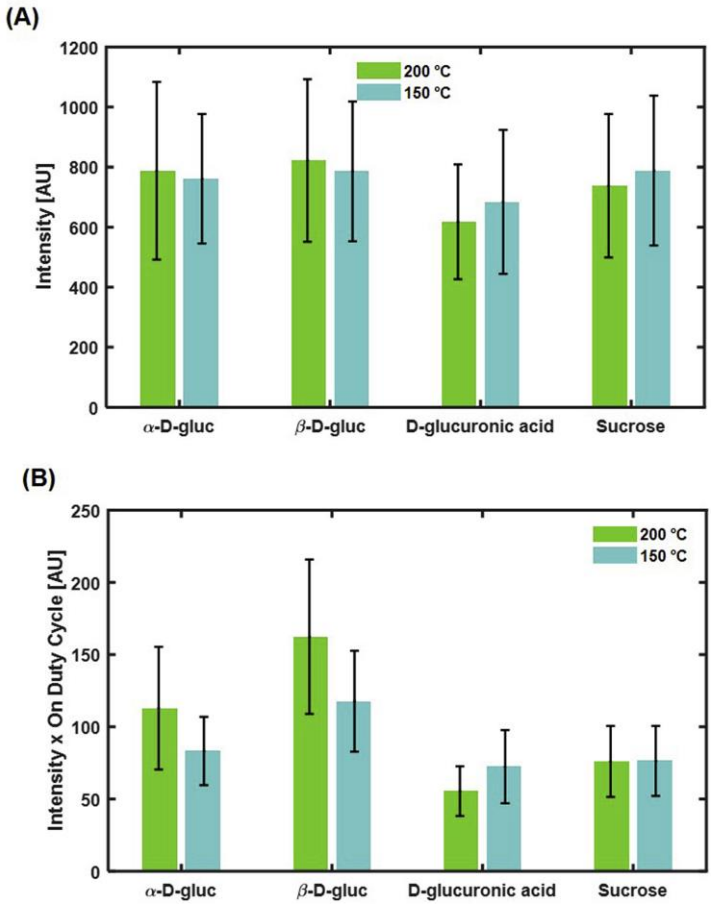

Figure 19. ***Single particle analysis of particle brightness***. (A) Average particle intensity. All particle types have comparable intensities. (B) The product of average intensity and t_{on} duty cycle. This appears more comparable to the bulk results than just examining intensity alone.

Comparing the photobleaching kinetics between bulk and single-particle measurements

Bulk photobleaching experiments determined that the photobleaching curves could be best fit with a second order exponential, implying that there may be more than one nanoparticle population present for each composition and temperature. This led to obtaining two time constants for each nanoparticle. In single-particle photobleaching experiments (Figure 20A), the photobleaching curves (Figure 20B) were best fit with second order exponential functions. However, the single particle time constants (Figure 20C) displayed a trend that was different than that of the bulk photobleaching experiments. α-D-gluc and Sucrose CDs had a higher first time constant for nanoparticles synthesized at 200 °C than those synthesized at 150 °C, while the first time constant for β-D-gluc was lower for nanoparticles synthesized at 200 °C than those synthesized at 150 °C. The first time constant did not change very much from one synthesis temperature to another for D-glucuronic acid CDs. The second time constant was found to decrease with a decrease in synthesis temperature for α-D-gluc and β-D-gluc CDs but increased with a decrease in temperature for D-glucuronic acid and sucrose CDs. We note that the bulk blinking lifetime is subjected to the "intensity-dependent" artifact. Indeed, densely packed particles can modify the local emission properties via e.g. secondary absorption of the emitted light. Thus, we focus on quantification of the photophysical properties of CDs at the single-particle level.

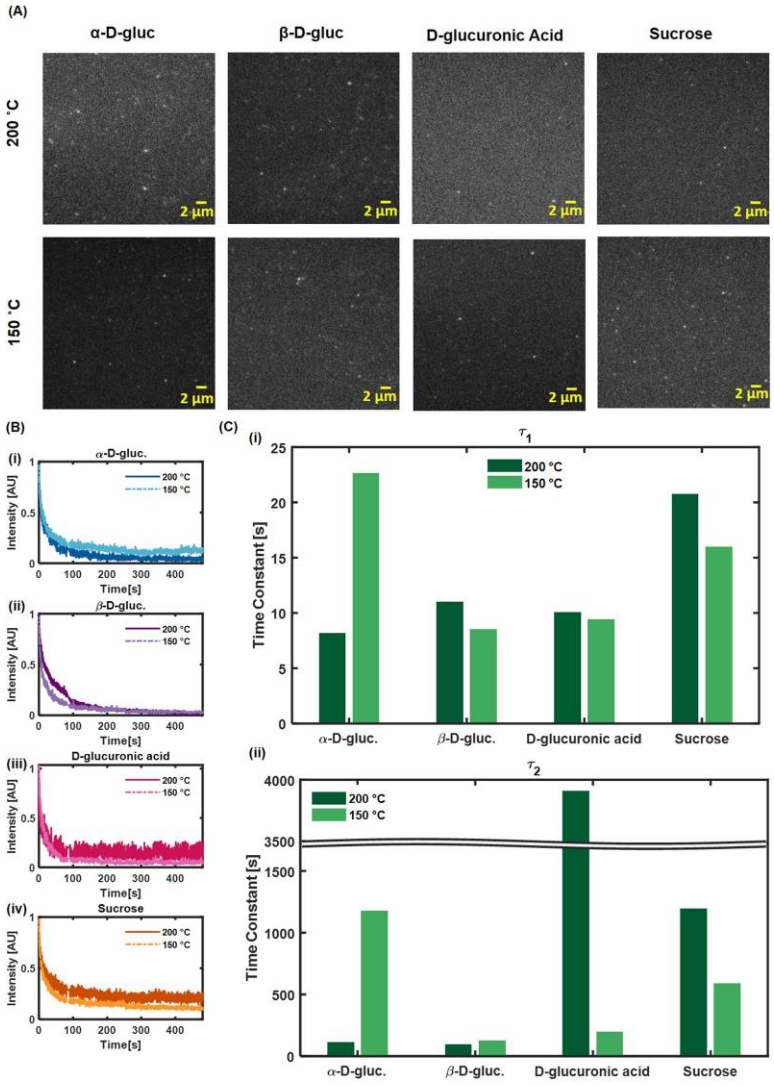

Figure 20. ***Single-particle photobleaching***. (A) Single-particle images. (B) Time to photobleaching curves for single particles (n=4 for each type). (C) Time constants determined form a second order exponential fit of the time to photobleaching curves.

Quantification of CD photoblinking

The double exponential components in the bleaching lifetime motivates us to pay closer attention to particle photophysics. A detailed examination of single-particle trajectories revealed two types of photophysical behaviors: 1) a single-step photobleaching and 2) a multiple-step photoblinking. Although the emission mechanism underlying these two distinct photophysics remains to be elucidated, these two types of optical behaviors may correspond to two types of

nanoparticles with distinct photobleaching characteristics. In particular, the single-step bleaching should contribute primarily to the fast decay constant, whereas the multiple-step photoblinking may account for the prolonged decay constant.

To better understand the photoblinking of single CDs, we proceeded to analyze their distribution of time on (t_{on}) and time off (t_{off}). It has been shown that carbon nanoparticles, like other types of nanosized emitters such as quantum dots, display a power-law distribution of t_{on} and t_{off}. Indeed, by using a change point algorithm to identify bright and dark states, we assigned each segment of the single-particle trajectories to either an "on" or "off" state. Consistent with previous studies [220], both t_{on} and t_{off} of nanoparticles showed a linear line in the log-log plot of probability vs. durations of t_{on} and t_{off} (Figure 21 A-B). We observed that the slopes of t_{on} and t_{off} do not vary significantly over temperature or precursor material (Figure 21 C-D). At first sight, this result seems to be contradictory to the observation that the on-time duty cycle between each type of particle significantly varies (e.g. from 9% to 20%) because a similar t_{on} slope implies that the probability distribution of each on-time duration remains the same. In fact, we can estimate the mean duration of on-time by a weighted average from each t_{on} power-law plot. The resulted mean values between each particle were indeed very consistent within a small range of 0.42 to 0.65 seconds, with the maximum value occurring for D-glucuronic acid 150 °C CDs, whose on-time duty cycle is at the lower end of 10 %.

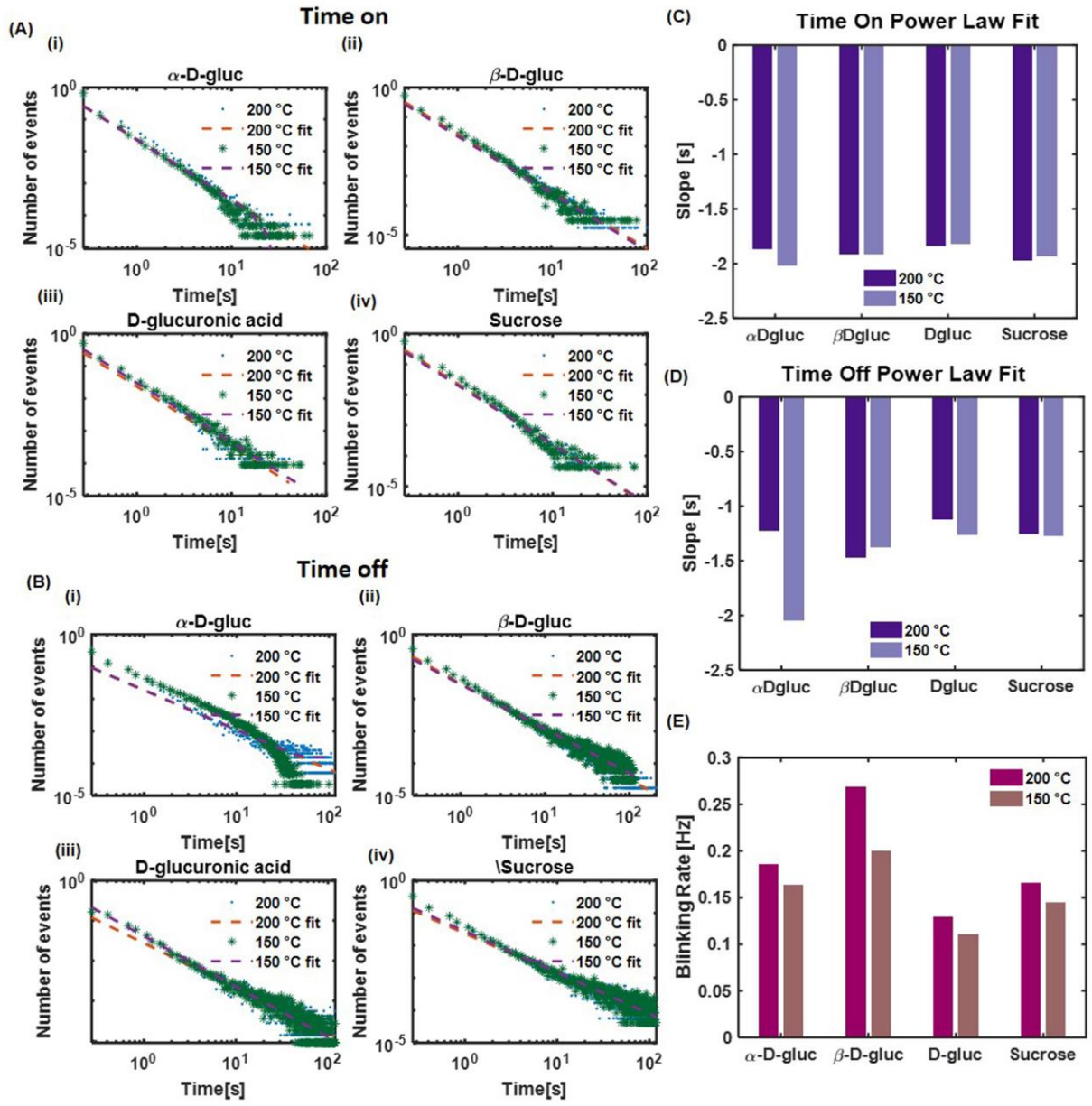

Figure 21. ***t_{on} and t_{off} photoblinking data based on many single-particle trajectories***. Data was fit with a power law distribution. (A) Time on distributions for each carbon source and synthesis temperature. (B) Time off distributions for each carbon source and synthesis temperature. (C) Slopes of time on power law fits. (D) Slopes of time off power law fits. (E) Blinking rate (transition rate) for each particle type and synthesis temperature.

This discrepancy can be explained by considering that the on-time duty cycle not only depends on the probability distribution of on-time duration but also depends on the blinking frequency. Indeed, when we calculated the average blinking frequency for each type of particle,

which is defined as the number of blinking events per unit time, we observed a significantly different range across all samples, ranging from 0.11 Hz (D-glucuronic acid 150 °C CDs) to 0.26 Hz (β-D-gluc 200 °C) (Figure 21E). The transition rate of each type of particle quantitatively determines the capacity of a particle to recover from an off state to an on state. Thus, for particles with similar instantaneous intensity (e.g. α-D-gluc 200 °C, β-D-gluc 150 °C, and sucrose 150 °C), the increase of particle brightness, which primarily arises from an increase of on-time duty cycle, arises from an increase of blinking frequency rather than a change in the distribution of on-time duration. Within all four precursor materials, an increase of the synthesis temperature leads to a slight increase of the blinking frequency. A summary of all results is provided in Figure 22.

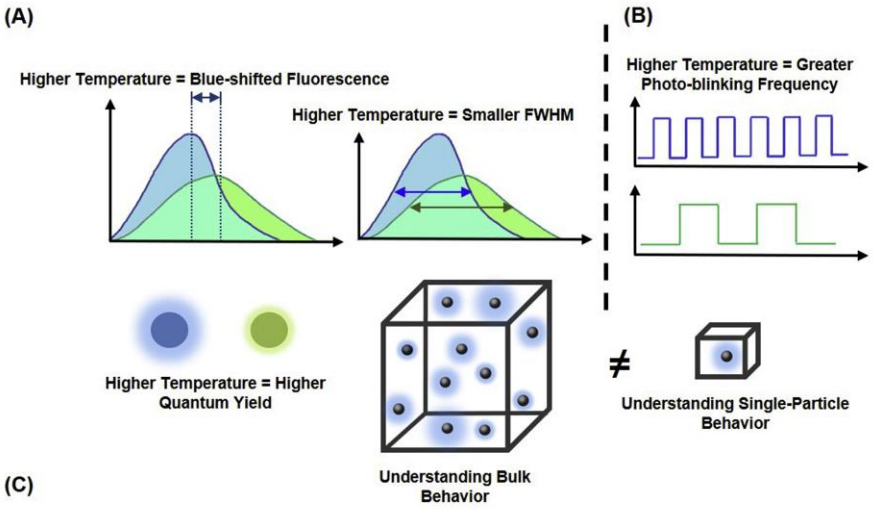

(C)

Single-Particle Brightness

Particle type	Instantaneous intensity [1/s]	Standard deviation [1/s]	Number of particles	On-time duty cycle [%]	Average on time [s]	Blinking frequency [Hz]
α-D-gluc, 200 °C	788.10	296.00	876	14.33	0.53	0.19
α-D-gluc, 150 °C	761.10	215.60	1223	10.94	0.46	0.16
β-D-gluc, 200 °C	822.30	270.60	1775	19.76	0.59	0.27
β-D-gluc, 150 °C	786.00	232.90	1351	14.98	0.51	0.20
D-glucuronic acid, 200 °C	617.90	191.40	619	8.97	0.47	0.13
D-glucuronic acid, 150 °C	684.10	239.50	985	10.58	0.65	0.11
Sucrose, 200 °C	738.00	238.90	871	10.30	0.42	0.17
Sucrose, 150 °C	788.50	249.50	1351	9.69	0.45	0.14

Figure 22. ***Summary of results***. (A) At the bulk level, a higher synthesis temperature was found to lead to a blue-shifted fluorescence, a smaller fluorescence full-width at half maximum (FWHM), and a higher quantum yield. (B) At the single-particle level, a higher temperature was

Figure 22 (cont.) found to lead to a greater photo-blinking frequency, which led to brighter signals from particles. (C) Evaluation at the single-particle level elucidates the effects of precursor and synthesis temperature on particle brightness.

We note that the on- and off-time power-law distribution curves down at the timescale of 10-100 sec. The downward curving of the power-law distribution may indicate competing physical processes that interrupt power-law blinking at this timescale. Indeed, this phenomenon has also been reported in early studies of quantum dots [221] and nanowires [222]. A slight better fit can be achieved with a "truncated power law". Because such modification does not change the conceptual description of photoblinking behaviors in this work, we chose to use the ordinary power-law distribution.

CHAPTER 4: MATERIALS AND METHODS

Optogenetic delineation of receptor tyrosine kinase subcircuits in PC12 cell differentiation

Experimental model and subject details

Cell culture

PC12 cells were cultured in F12K medium supplemented with 15% horse serum, 2.5% FBS, and 1× Penicillin-Streptomycin solution (complete medium). HEK293T and MDA-MB-231 cells were cultured in DMEM medium supplemented with 10% FBS and 1× Penicillin-Streptomycin solution. Information about cell line sex is unavailable.

Method details

Materials

Phusion DNA polymerase master mix was purchased from NEB (Cat. #M0531). Oligonucleotides and gBlock Gene Fragments for cloning were purchased from IDT. In-Fusion HD Cloning Plus kit was purchased from Clontech (Cat. #638909). BamHI, NheI, Turbofect transfection reagent, protease/phosphatase inhibitors, Bradford reagent, and Calcein AM were purchased from Thermo Fisher Scientific (Cat. #FD0054, #FD0973, #R0533, #A32959, #23238, #C3100MP). F12K cell media and horse serum were purchased from Gibco (Cat. #21127-022, #26050-088). Fetal bovine serum (FBS) was purchased from Sigma-Aldrich (Cat. #12303C). Penicillin-Streptomycin solution and DPBS were purchased from Corning (Cat. #30-002-CI, #21-031-CV). RIPA lysis buffer was purchased from Millipore (Cat. #20-188). LDS sample buffer was purchased from Invitrogen (Cat. #NP0007). Polyacrylamide gels, PVDF membrane, and protein standards were purchased from Bio-Rad (Cat. # 4561046, # 1620177, # 1610374).

NGF and antibodies were purchased from Cell Signaling Technology (Cat. #5221, #9101, #9102, #2821, #2822, #2956, #7074). Erlotinib was purchased from Selleck Chemicals (Cat. #S7786). U73122 and GF 109203X were purchased from Tocris (Cat. #1268, #0741).

Plasmid construction

Lyn-TrkAICD-AuLOV-GFP was constructed by inserting a gBlock fragment coding the Lyn lipidation tag fused to the rat TrkA ICD and AuLOV (Lyn-TrkAICD-AuLOV) into a pEGFP-N1 vector (Clontech, discontinued; www.addgene.org/vector-database/2491/; linearized by NheI and BamHI digestion) using In-Fusion cloning. ICD mutants were generated using overlap extension PCR.

Cell culture and transfection

PC12 cells were cultured in F12K medium supplemented with 15% horse serum, 2.5% FBS, and 1× Penicillin-Streptomycin solution (complete medium). Cultures were maintained in a standard humidified incubator at 37 ºC with 5% CO_2. For differentiation assays, 2400 ng of DNA were combined with 7.2 μL of Turbofect in 240 μL of serum-free F12K. For western blots, 1200 ng of DNA (1200 ng No ICD construct alone or 700 ng No ICD construct + 500 ng ICD-containing construct) were combined with 3.6 μL of Turbofect in 120 μL of serum-free F12K. The transfection mixtures were incubated at room temperature for 20 minutes prior to adding to cells cultured in 35 mm dishes with 500 μL complete medium. For differentiation assays, the transfection medium was replaced with 2 mL complete medium after 3 hours of transfection to recover cells overnight. For western blots, the transfection medium was replaced with 1 mL

serum-free F12K supplemented with 1× Penicillin-Streptomycin solution after 3 hours of transfection to serum-starved cells overnight.

PC12 cell differentiation assay

Transfected and recovered PC12 cells were switched to F12K supplemented with 0.15% horse serum, 0.025% FBS, and 1× Penicillin-Streptomycin solution (starvation medium) immediately prior to incubating cells on a homemade blue LED light box emitting at 300 μW/cm^2. Untransfected cells were similarly switched to starvation medium immediately prior to NGF treatment. Any inhibitors were added prior to NGF or light treatment. Cells were incubated with light for 24 or 44 hours before imaging GFP fluorescence at 10× magnification using a Leica DMI8 microscope. Untransfected cells were treated with 1 μM Calcein AM for 10 minutes before imaging. Differentiation ratios were calculated as follows:

$$\frac{\#\text{ of green fluorescing cells with neurite length longer than the cell body diameter}}{\#\text{ of green fluorescing cells}}$$

Epi-illumination fluorescence live-cell microscopy

An epi-illumination inverted fluorescence microscope (Leica DMI8) equipped with a 10×, 100× objective (HCX PL FLUOTAR 100×/1.30 oil) and a light-emitting diode illuminator (SOLA SE II 365) transfected cells. Green fluorescence was detected using the GFP filter cube (Leica, excitation filter 472/30, dichroic mirror 495, and emission filter 520/35). Exposure time for both fluorescence channel was 200 ms.

Three-dimensional structured illumination microscopy (SIM)

A total of 2×10^5 MDA-MB-231 cells were seeded into a 35 mm dish containing a 14 mm coverslip 24 hours prior to transfection with WT ICD. Super-resolution images were acquired on an N-SIM Microscope (Nikon, Tokyo, Japan) equipped with solid-state lasers (405 nm and 488 nm). Light-induced WT ICD homo-association was stimulated by 405 nm, and SIM images were acquired under 488 nm excitation. The cells were exposed to continuous blue light (405 nm) for 300 seconds. SIM images were captured at the beginning and the end of illumination using an electron-multiplying charge coupled device (EMCCD) camera (iXon 897, Andor, USA). To reduce photobleaching during SIM image acquisition, laser power (488 nm) was reduced to <20% with a minimum exposure time of 200 ms for each image. Images were obtained at 512 × 512 using Z-stacks with a step size of 0.125 μm. SIM frames were deliberately spaced at 2-s intervals. SIM images were analyzed with Nikon Elements and ImageJ.

Western blot

All transfected and serum-starved PC12 cells were treated with 10 μM Erlotinib (an EGFR inhibitor) for 5 minutes prior to illumination to further minimize baseline signaling. Cell were then illuminated for 10 minutes using a homemade blue LED light box emitting at 5 mW/cm^2. For PLCγ and PKC inhibitor experiments, cells were treated with inhibitors for 10 minutes prior to light treatment. Following illumination, cells were washed once with 1 mL cold DBPS and lysed with 100 μL cold lysis buffer (RIPA + protease/phosphatase inhibitor cocktail). Lysates were centrifuged at 17,000 RCF, 4 °C for 10 minutes to pellet cell debris. Purified lysates were normalized using Bradford reagent. Normalized samples were mixed with LDS buffer and loaded onto 12% polyacrylamide gels. SDS-PAGE was performed at room temperature. Samples

were transferred to PVDF membranes overnight at 30 V, 4 °C. Membranes were blocked in 5% BSA/TBST for 1 hour at room temperature and probed with the primary and secondary antibodies according to company guidelines. Membranes were incubated with ECL substrate and imaged using a Bio-Rad ChemiDoc XRS chemiluminescence detector. Signal analysis was performed using ImageJ. Activity is defined as the signal ratio of phospho-target/total target. All reported activity is normalized to the "dark" activity of each tested condition.

Quantification and statistical analysis

The p-values were determined by performing two-tailed, unpaired t-test using the GraphPad Prism software. The p-values were determined by performing two-tailed, unpaired t-test using the GraphPad Prism software.

Single-molecule analysis of fluorescent carbon dots by TIRF microscopy

The analysis of carbon dots synthesized in the presence of N-methyl morpholine-N-oxide

Single-particle fluorescence microscopy

Objective-based total internal reflection fluorescence microscopy (TIRFM) was used for single-particle imaging. A continuous wavelength (488-nm, Spectral physics) laser was used as the light source. An inverted microscope (IX73) equipped with a 100x oil immersion objective (Olympus, PlanApo, 100×, N.A. 1.49, oil immersion) was used. The laser beam was then expanded, collimated to about 35 mm, and directed into the microscope by 400-mm lens (Thorlabs LA1725A). The incident light was directed through the objective via an exciter (FF01-482/563-25) and a dual-band dichroic filter (Di01-R488/561-25x36). The mean excitation power before the objective is about 1.5 mW/cm^2. The luminescence photons from individual CDs were

collected by the same objective, passing an emitter (FF01-523/610-25) and captured by an Electron Multiplying Charge Coupled Device (EMCCD) camera (iXon U797, Andor. Technology) The emission filter was designed to have a spectral cut off at 500-548 nm, covering the central wavelength of CDs emission at 500 nm. Thus, experimental observations of emission intensity were not affected by potential spectral diffusion of ±10 nm. The sample coverslip was secured onto a 2-D stage. Individual nanoparticles were located by raster scanning the stage. An exposure time of 100 ms was used. At least ten time-stamped image stacks, each of which consists of 600 frames, were taken for each type of particle.

Intracellular imaging of CD-NMMOs with epi-fluorescence microscopy

An epi-illumination inverted fluorescence microscope (Leica DMI8) equipped with a 100× objective (HCX PL FLUOTAR 100×/1.30 oil) and a light-emitting diode illuminator (SOLA SE II 365) was used to image CDs in fixed cells. Red fluorescence was detected using the TX2 filter cube (Leica, excitation filter 560/40, dichroic mirror 595, and emission filter 645/75). Green fluorescence was detected using the GFP filter cube (Leica, excitation filter 472/30, dichroic mirror 495, and emission filter 520/35). Exposure time for both fluorescence channel was 200 ms.

Image analysis for single-particle imaging

All analysis for single-particle imaging was performed with a custom-written software in MATLAB. For each frame, a 7×7-pixel area surrounding each individual fluorescent spot was identified. The background level was calculated by averaging the intensity of the peripheral pixels excluding the central spot. The intensity of each spot was calculated by averaging all

intensities from each pixel within the central spot. The net intensity of each spot was calculated by subtracting the background level from that of the central spot. The number of photons was calculated by following a formula provided by the vendor.

$$\mathbf{Photons} = \frac{(\mathbf{electrical\ count} - \mathbf{bias\ offset}) \times \mathbf{preamp}}{\mathbf{EM\ gain} \times \mathbf{QE}}$$

Intracellular image analysis for CD-NMMOs

The region of interest (ROI) *Manager* plugin from FIJI was used to analyze the correlation of fluorescence intensities for CD-NMMOs in C32 cells. A snapshot of each field of view was acquired in three channels (TX2, GFP, and Phase contrast). Manual selection of the cell profile was used to enclose each cellular area. An ROI with no cells were selected as the background. The average fluorescence intensity in each ROI was measured from the plugin. The fluorescence intensity of each cell was calculated by subtracting the background level from that of each cell. More than 50 cells were analyzed for each condition.

Imaging CD-NMMO fraction with epi-fluorescence microscopy

C32 cells were seeded into a multi-cavity PDMS chamber (cavity diameter = 5 mm) placed on top of a coverslip 24 hours before treatment. Prior to imaging, cells were incubated with each CD fraction (one per cavity) for 15 min at 37oC, 5% CO_2, followed by a single wash and submersion with DPBS. Live cells were imaged using an inverted epi-illumination fluorescence microscope (Leica DMI8) equipped with a 100× objective (HCX PL FLUOTAR 100×/1.30 oil) and a light-emitting diode illuminator (SOLA SE II 365). Red fluorescence was detected using the Y5 filter cube (Leica, excitation filter 620/60, dichroic mirror 660, and emission filter 700/75) with an exposure time of 600 ms. Yellow fluorescence was detected using the TX2 filter cube (Leica,

excitation filter 560/40, dichroic mirror 595, and emission filter 645/75) with an exposure time of 300 ms. Green fluorescence was detected using the GFP filter cube (Leica, excitation filter 472/30, dichroic mirror 495, and emission filter 520/35) with an exposure time of 200 ms. Blue fluorescence was detected using the DAPI filter cube (Leica, excitation filter 350/50, dichroic mirror 400, and emission filter 460/50) with an exposure time of 100 ms.

The analysis of carbon dots synthesized using different carbon sources and temperatures

Single-particle photobleaching

A droplet of 0.2 μL of CD samples was applied to a clean coverslip. The coverslip was then kept in a clean biosafety cabinet for 10 min to allow the droplet to dry. Concentrations of each CD sample were adjusted so that a layer formed on the surface. To measure the photostability of CDs, the coverslip was placed on a home-built TIRF microscope and the boundary of the dried smear of CDs was localized. An inverted microscope equipped with a 100x oil immersion objective was used. The laser beam was then expanded, collimated to about 35 mm, and directed into the microscope by a lens (focal length = 400 mm). The incident light was directed through the objective via an exciter and a dual-band dichroic filter. The mean excitation power before the objective is 1.5 mW/cm^2. For each field of view, 2400 time-stamped images were taken with the exposure time of 200 ms per frame, which accounts for a total of 8 min of trajectory. The CD signal (inside the boundary) and background (outside the boundary) were extracted by averaging a total of 100×100 pixels in the corresponding area. The net signal of CDs was calculated by subtracting the background from the gross CD signal for each frame. The emission decaying curve was generated by normalizing the maximum net CD signal to 1.0. A script was used to fit

the normalized emission decaying curve with a two-component exponential function. The photobleaching lifetime was extracted from the fitted values.

Data analysis for single-particle photobleaching

A MATLAB (Version R2016a) code was generated from the built-in "Curve Fitting Tool" to fit the single-particle photobleaching trajectories. A two-component exponential function gave the best fit, which generated two time constants, τ_1 and τ_2, as well as their respective weights and the goodness of fit (R^2).

$$f(t) = ae^{(\frac{1}{\tau_1})t} + ce^{(\frac{1}{\tau_2})t}$$

Because the variance of the data is larger at the longer timescale than at the shorter timescale, the "Weighted Least Square" fit option was used and each data point was weighted by its variance.

Single-particle photoblinking analysis

Single-particle trajectories were segmented to define the "on" and "off" states based on the changepoint analysis. The intensity threshold was defined as the mean of the segment with the lowest intensity plus three times the standard deviation of that segment (Mean + 3 σ). A segment of the trajectory whose intensity was above this threshold is defined as an "ON" state and its duration as t_{on}. An "OFF" state refers to any segment whose intensity was below the threshold and its duration as t_{off}. An array of t_{on} and t_{off} was collected from each trajectory and pooled for the same type of particle. The power-law distribution of t_{on} and t_{off} were generated by plotting the histogram of pooled data.

REFERENCES

1 Perrimon, N., Pitsouli, C. & Shilo, B. Z. Signaling mechanisms controlling cell fate and embryonic patterning. *Cold Spring Harb Perspect Biol* **4**, a005975, (2012).

2 Isomura, A. & Kageyama, R. Ultradian oscillations and pulses: coordinating cellular responses and cell fate decisions. *Development* **141**, 3627-3636, (2014).

3 Deblandre, G. A., Wettstein, D. A., Koyano-Nakagawa, N. & Kintner, C. A two-step mechanism generates the spacing pattern of the ciliated cells in the skin of Xenopus embryos. *Development* **126**, 4715-4728, (1999).

4 Pourquie, O. Vertebrate segmentation: from cyclic gene networks to scoliosis. *Cell* **145**, 650-663, (2011).

5 Hubaud, A. & Pourquie, O. Making the clock tick: right time, right pace. *Dev Cell* **24**, 115-116, (2013).

6 Schroter, C. *et al.* Dynamics of zebrafish somitogenesis. *Dev Dyn* **237**, 545-553, (2008).

7 Marshall, C. J. Specificity of receptor tyrosine kinase signaling: transient versus sustained extracellular signal-regulated kinase activation. *Cell* **80**, 179-185, (1995).

8 Santos, S. D., Verveer, P. J. & Bastiaens, P. I. Growth factor-induced MAPK network topology shapes Erk response determining PC-12 cell fate. *Nat Cell Biol* **9**, 324-330, (2007).

9 Albeck, J. G., Mills, G. B. & Brugge, J. S. Frequency-modulated pulses of ERK activity transmit quantitative proliferation signals. *Mol Cell* **49**, 249-261, (2013).

10 Ji, Y. *et al.* Acute and gradual increases in BDNF concentration elicit distinct signaling and functions in neurons. *Nat Neurosci* **13**, 302-309, (2010).

11 Guo, W., Ji, Y., Wang, S., Sun, Y. & Lu, B. Neuronal activity alters BDNF-TrkB signaling kinetics and downstream functions. *J Cell Sci* **127**, 2249-2260, (2014).

12 Imayoshi, I. *et al.* Oscillatory control of factors determining multipotency and fate in mouse neural progenitors. *Science* **342**, 1203-1208, (2013).

13 Shimojo, H., Ohtsuka, T. & Kageyama, R. Oscillations in notch signaling regulate maintenance of neural progenitors. *Neuron* **58**, 52-64, (2008).

14 Kholodenko, B. N. Negative feedback and ultrasensitivity can bring about oscillations in the mitogen-activated protein kinase cascades. *Eur J Biochem* **267**, 1583-1588, (2000).

15 Hadac, O., Muzika, F., Nevoral, V., Pribyl, M. & Schreiber, I. Minimal oscillating subnetwork in the Huang-Ferrell model of the MAPK cascade. *PLoS One* **12**, e0178457, (2017).

16 Kochanczyk, M. *et al.* Relaxation oscillations and hierarchy of feedbacks in MAPK signaling. *Sci Rep* **7**, 38244, (2017).

17 Kobayashi, T. *et al.* The cyclic gene Hes1 contributes to diverse differentiation responses of embryonic stem cells. *Genes Dev* **23**, 1870-1875, (2009).

18 Hughes, R. M., Bolger, S., Tapadia, H. & Tucker, C. L. Light-mediated control of DNA transcription in yeast. *Methods* **58**, 385-391, (2012).

19 Sauer, B. Inducible gene targeting in mice using the Cre/lox system. *Methods* **14**, 381-392, (1998).

20 Ling, M. M. & Robinson, B. H. Approaches to DNA mutagenesis: an overview. *Anal Biochem* **254**, 157-178, (1997).

21 Sosa, M. A. G., De Gasperi, R. & Elder, G. A. Animal transgenesis: an overview. *Brain Struct Funct* **214**, 91-109, (2010).

22 Banghart, M., Borges, K., Isacoff, E., Trauner, D. & Kramer, R. H. Light-activated ion channels for remote control of neuronal firing. *Nature Neuroscience* **7**, 1381-1386, (2004).
23 Boyden, E. S., Zhang, F., Bamberg, E., Nagel, G. & Deisseroth, K. Millisecond-timescale, genetically targeted optical control of neural activity. *Nature Neuroscience* **8**, 1263-1268, (2005).
24 Bi, A. D. *et al.* Ectopic expression of a microbial-type rhodopsin restores visual responses in mice with photoreceptor degeneration. *Neuron* **50**, 23-33, (2006).
25 Deisseroth, K. *et al.* Next-generation optical technologies for illuminating genetically targeted brain circuits. *Journal of Neuroscience* **26**, 10380-10386, (2006).
26 Tye, K. M. & Deisseroth, K. Optogenetic investigation of neural circuits underlying brain disease in animal models. *Nature Reviews Neuroscience* **13**, 251-266, (2012).
27 Aston-Jones, G. & Deisseroth, K. Recent advances in optogenetics and pharmacogenetics. *Brain Res* **1511**, 1-5, (2013).
28 Vazey, E. M. & Aston-Jones, G. New tricks for old dogmas: Optogenetic and designer receptor insights for Parkinson's disease. *Brain Res* **1511**, 153-163, (2013).
29 Astori, S., Wimmer, R. D. & Luthi, A. Manipulating sleep spindles - expanding views on sleep, memory, and disease. *Trends Neurosci* **36**, 738-748, (2013).
30 Govorunova, E. G., Cunha, S. R., Sineshchekov, O. A. & Spudich, J. L. Anion channelrhodopsins for inhibitory cardiac optogenetics. *Sci Rep-Uk* **6**, (2016).
31 Entcheva, E. Cardiac optogenetics. *Am J Physiol-Heart C* **304**, H1179-H1191, (2013).
32 Mei, Y. & Zhang, F. Molecular Tools and Approaches for Optogenetics. *Biol Psychiat* **71**, 1033-1038, (2012).
33 Sorensen, A. T. & Kokaia, M. Novel approaches to epilepsy treatment. *Epilepsia* **54**, 1-10, (2013).
34 Busskamp, V., Picaud, S., Sahel, J. A. & Roska, B. Optogenetic therapy for retinitis pigmentosa. *Gene Ther* **19**, 169-175, (2012).
35 Sahel, J. A. & Roska, B. Gene Therapy for Blindness. *Annual Review of Neuroscience, Vol 36* **36**, 467-488, (2013).
36 Knopfel, T. *et al.* Toward the Second Generation of Optogenetic Tools. *Journal of Neuroscience* **30**, 14998-15004, (2010).
37 Shimizu-Sato, S., Huq, E., Tepperman, J. M. & Quail, P. H. A light-switchable gene promoter system. *Nature Biotechnology* **20**, 1041-1044, (2002).
38 Wu, Y. I. *et al.* A genetically encoded photoactivatable Rac controls the motility of living cells. *Nature* **461**, 104-U111, (2009).
39 Levskaya, A., Weiner, O. D., Lim, W. A. & Voigt, C. A. Spatiotemporal control of cell signalling using a light-switchable protein interaction. *Nature* **461**, 997-1001, (2009).
40 Yazawa, M., Sadaghiani, A. M., Hsueh, B. & Dolmetsch, R. E. Induction of protein-protein interactions in live cells using light. *Nature Biotechnology* **27**, 941-U105, (2009).
41 Kennedy, M. J. *et al.* Rapid blue-light-mediated induction of protein interactions in living cells. *Nature Methods* **7**, 973-U948, (2010).
42 Toettcher, J. E., Voigt, C. A., Weiner, O. D. & Lim, W. A. The promise of optogenetics in cell biology: interrogating molecular circuits in space and time. *Nature Methods* **8**, 35-38, (2011).
43 Strickland, D. *et al.* TULIPs: tunable, light-controlled interacting protein tags for cell biology. *Nature Methods* **9**, 379-U392, (2012).

44 Kim, B. & Lin, M. Z. Optobiology: optical control of biological processes via protein engineering. *Biochem Soc T* **41**, 1183-1188, (2013).
45 Eleftheriou, C., Cesca, F., Maragliano, L., Benfenati, F. & Maya-Vetencourt, J. F. Optogenetic Modulation of Intracellular Signalling and Transcription: Focus on Neuronal Plasticity. *J Exp Neurosci* **11**, (2017).
46 Gautier, A. *et al.* How to control proteins with light in living systems. *Nat Chem Biol* **10**, 533-541, (2014).
47 Zhou, X. X., Pane, M. & Lin, M. Z. Investigating neuronal function with optically controllable proteins. *Front Mol Neurosci* **8**, (2015).
48 Zhang, K. & Cui, B. Optogenetic control of intracellular signaling pathways. *Trends Biotechnol* **33**, 92-100, (2015).
49 Schmidt, D. & Cho, Y. K. Natural photoreceptors and their application to synthetic biology. *Trends in Biotechnology* **33**, 80-91, (2015).
50 Brieke, C., Rohrbach, F., Gottschalk, A., Mayer, G. & Heckel, A. Light-controlled tools. *Angew Chem Int Ed Engl* **51**, 8446-8476, (2012).
51 Losi, A. & Gartner, W. The evolution of flavin-binding photoreceptors: an ancient chromophore serving trendy blue-light sensors. *Annu Rev Plant Biol* **63**, 49-72, (2012).
52 van der Horst, M. A. & Hellingwerf, K. J. Photoreceptor proteins, "star actors of modern times": a review of the functional dynamics in the structure of representative members of six different photoreceptor families. *Acc Chem Res* **37**, 13-20, (2004).
53 Karunarathne, W. K., O'Neill, P. R. & Gautam, N. Subcellular optogenetics - controlling signaling and single-cell behavior. *J Cell Sci* **128**, 15-25, (2015).
54 Shcherbakova, D. M., Shemetov, A. A., Kaberniuk, A. A. & Verkhusha, V. V. Natural Photoreceptors as a Source of Fluorescent Proteins, Biosensors, and Optogenetic Tools. *Annu Rev Biochem* **84**, 519-550, (2015).
55 Fenno, L., Yizhar, O. & Deisseroth, K. The development and application of optogenetics. *Annu Rev Neurosci* **34**, 389-412, (2011).
56 Rein, M. L. & Deussing, J. M. The optogenetic (r)evolution. *Mol Genet Genomics* **287**, 95-109, (2012).
57 Del Bene, F. & Wyart, C. Optogenetics: a new enlightenment age for zebrafish neurobiology. *Dev Neurobiol* **72**, 404-414, (2012).
58 Berlin, S. & Isacoff, E. Y. Synapses in the spotlight with synthetic optogenetics. *EMBO Rep* **18**, 677-692, (2017).
59 Hegemann, P. & Nagel, G. From channelrhodopsins to optogenetics. *EMBO Mol Med* **5**, 173-176, (2013).
60 Hegemann, P. & Moglich, A. Channelrhodopsin engineering and exploration of new optogenetic tools. *Nat Methods* **8**, 39-42, (2011).
61 Deisseroth, K. Optogenetics: 10 years of microbial opsins in neuroscience. *Nat Neurosci* **18**, 1213-1225, (2015).
62 Lungu, O. I. *et al.* Designing photoswitchable peptides using the AsLOV2 domain. *Chem Biol* **19**, 507-517, (2012).
63 Guntas, G. *et al.* Engineering an improved light-induced dimer (iLID) for controlling the localization and activity of signaling proteins. *P Natl Acad Sci USA* **112**, 112-117, (2015).
64 Hallett, R. A., Zimmerman, S. P., Yumerefendi, H., Bear, J. E. & Kuhlman, B. Correlating in Vitro and in Vivo Activities of Light-Inducible Dimers: A Cellular Optogenetics Guide. *ACS Synth Biol* **5**, 53-64, (2016).

65 Wang, H. *et al.* LOVTRAP: an optogenetic system for photoinduced protein dissociation. *Nature Methods* **13**, 755-758, (2016).
66 Nakatani, Y. & Hisatomi, O. Molecular Mechanism of Photozipper, a Light-Regulated Dimerizing Module Consisting of the bZIP and LOV Domains of Aureochrome-1. *Biochemistry* **54**, 3302-3313, (2015).
67 Grusch, M. *et al.* Spatio-temporally precise activation of engineered receptor tyrosine kinases by light. *EMBO J* **33**, 1713-1726, (2014).
68 Kawano, F., Suzuki, H., Furuya, A. & Sato, M. Engineered pairs of distinct photoswitches for optogenetic control of cellular proteins. *Nature Communications* **6**, (2015).
69 Zhou, X. X., Fan, L. Z., Li, P., Shen, K. & Lin, M. Z. Optical control of cell signaling by single-chain photoswitchable kinases. *Science* **355**, 836-842, (2017).
70 Taslimi, A. *et al.* Optimized second-generation CRY2-CIB dimerizers and photoactivatable Cre recombinase. *Nat Chem Biol* **12**, 425-430, (2016).
71 Taslimi, A. *et al.* An optimized optogenetic clustering tool for probing protein interaction and function. *Nat Commun* **5**, 4925, (2014).
72 Park, H. *et al.* Optogenetic protein clustering through fluorescent protein tagging and extension of CRY2. *Nature Communications* **8**, (2017).
73 Kainrath, S., Stadler, M., Reichhart, E., Distel, M. & Janovjak, H. Green-Light-Induced Inactivation of Receptor Signaling Using Cobalamin-Binding Domains. *Angew Chem Int Ed Engl* **56**, 4608-4611, (2017).
74 Buckley, C. E. *et al.* Reversible Optogenetic Control of Subcellular Protein Localization in a Live Vertebrate Embryo. *Dev Cell* **36**, 117-126, (2016).
75 Kaberniuk, A. A., Shemetov, A. A. & Verkhusha, V. V. A bacterial phytochrome-based optogenetic system controllable with near-infrared light. *Nat Methods* **13**, 591-597, (2016).
76 Redchuk, T. A., Omelina, E. S., Chernov, K. G. & Verkhusha, V. V. Near-infrared optogenetic pair for protein regulation and spectral multiplexing. *Nat Chem Biol* **13**, 633-639, (2017).
77 Reichhart, E., Ingles-Prieto, A., Tichy, A. M., McKenzie, C. & Janovjak, H. A Phytochrome Sensory Domain Permits Receptor Activation by Red Light. *Angew Chem Int Ed Engl* **55**, 6339-6342, (2016).
78 Voss, S., Klewer, L. & Wu, Y. W. Chemically induced dimerization: reversible and spatiotemporal control of protein function in cells. *Curr Opin Chem Biol* **28**, 194-201, (2015).
79 Ellis-Davies, G. C. Caged compounds: photorelease technology for control of cellular chemistry and physiology. *Nat Methods* **4**, 619-628, (2007).
80 Amatrudo, J. M., Olson, J. P., Agarwal, H. K. & Ellis-Davies, G. C. Caged compounds for multichromic optical interrogation of neural systems. *Eur J Neurosci* **41**, 5-16, (2015).
81 Inoue, T., Heo, W. D., Grimley, J. S., Wandless, T. J. & Meyer, T. An inducible translocation strategy to rapidly activate and inhibit small GTPase signaling pathways. *Nat Methods* **2**, 415-418, (2005).
82 Karginov, A. V. *et al.* Light regulation of protein dimerization and kinase activity in living cells using photocaged rapamycin and engineered FKBP. *J Am Chem Soc* **133**, 420-423, (2011).
83 Brown, K. A. *et al.* Light-cleavable rapamycin dimer as an optical trigger for protein dimerization. *Chem Commun (Camb)* **51**, 5702-5705, (2015).

84 Wright, C. W., Guo, Z. F. & Liang, F. S. Light control of cellular processes by using photocaged abscisic acid. *Chembiochem* **16**, 254-261, (2015).
85 Ballister, E. R., Aonbangkhen, C., Mayo, A. M., Lampson, M. A. & Chenoweth, D. M. Localized light-induced protein dimerization in living cells using a photocaged dimerizer. *Nat Commun* **5**, 5475, (2014).
86 Zimmermann, M. *et al.* Cell-permeant and photocleavable chemical inducer of dimerization. *Angew Chem Int Ed Engl* **53**, 4717-4720, (2014).
87 Schelkle, K. M. *et al.* Light-induced protein dimerization by one- and two-photon activation of gibberellic acid derivatives in living cells. *Angew Chem Int Ed Engl* **54**, 2825-2829, (2015).
88 Young, T. S. & Schultz, P. G. Beyond the canonical 20 amino acids: expanding the genetic lexicon. *J Biol Chem* **285**, 11039-11044, (2010).
89 Gautier, A. *et al.* Genetically encoded photocontrol of protein localization in mammalian cells. *J Am Chem Soc* **132**, 4086-4088, (2010).
90 Gautier, A., Deiters, A. & Chin, J. W. Light-activated kinases enable temporal dissection of signaling networks in living cells. *J Am Chem Soc* **133**, 2124-2127, (2011).
91 Hemphill, J., Chou, C., Chin, J. W. & Deiters, A. Genetically encoded light-activated transcription for spatiotemporal control of gene expression and gene silencing in mammalian cells. *J Am Chem Soc* **135**, 13433-13439, (2013).
92 Hemphill, J., Borchardt, E. K., Brown, K., Asokan, A. & Deiters, A. Optical Control of CRISPR/Cas9 Gene Editing. *J Am Chem Soc* **137**, 5642-5645, (2015).
93 Luo, J. *et al.* Genetically encoded optical activation of DNA recombination in human cells. *Chem Commun (Camb)* **52**, 8529-8532, (2016).
94 Kusen, P. M. *et al.* Optogenetic Regulation of Tunable Gene Expression in Yeast Using Photo-Labile Caged Methionine. *ACS Chem Biol* **11**, 2915-2922, (2016).
95 Clapham, D. E. Calcium signaling. *Cell* **131**, 1047-1058, (2007).
96 Berridge, M. J., Bootman, M. D. & Roderick, H. L. Calcium signalling: dynamics, homeostasis and remodelling. *Nat Rev Mol Cell Biol* **4**, 517-529, (2003).
97 Ye, H., Daoud-El Baba, M., Peng, R. W. & Fussenegger, M. A synthetic optogenetic transcription device enhances blood-glucose homeostasis in mice. *Science* **332**, 1565-1568, (2011).
98 Fukuda, N., Matsuda, T. & Nagai, T. Optical control of the Ca2+ concentration in a live specimen with a genetically encoded Ca2+-releasing molecular tool. *ACS Chem Biol* **9**, 1197-1203, (2014).
99 Ishii, T. *et al.* Light generation of intracellular Ca(2+) signals by a genetically encoded protein BACCS. *Nat Commun* **6**, 8021, (2015).
100 He, L. *et al.* Near-infrared photoactivatable control of Ca(2+) signaling and optogenetic immunomodulation. *Elife* **4**, (2015).
101 Kyung, T. *et al.* Optogenetic control of endogenous Ca(2+) channels in vivo. *Nat Biotechnol* **33**, 1092-1096, (2015).
102 Di Paolo, G. & De Camilli, P. Phosphoinositides in cell regulation and membrane dynamics. *Nature* **443**, 651-657, (2006).
103 Xie, B. *et al.* Plasma Membrane Phosphatidylinositol 4,5-Bisphosphate Regulates Ca(2+)-Influx and Insulin Secretion from Pancreatic beta Cells. *Cell Chem Biol* **23**, 816-826, (2016).

104 Logan, M. R. & Mandato, C. A. Regulation of the actin cytoskeleton by PIP2 in cytokinesis. *Biol Cell* **98**, 377-388, (2006).
105 Guglielmi, G., Barry, J. D., Huber, W. & De Renzis, S. An Optogenetic Method to Modulate Cell Contractility during Tissue Morphogenesis. *Dev Cell* **35**, 646-660, (2015).
106 Insall, R. H. & Weiner, O. D. PIP3, PIP2, and cell movement--similar messages, different meanings? *Dev Cell* **1**, 743-747, (2001).
107 Heasman, S. J. & Ridley, A. J. Mammalian Rho GTPases: new insights into their functions from in vivo studies. *Nat Rev Mol Cell Biol* **9**, 690-701, (2008).
108 Hodge, R. G. & Ridley, A. J. Regulating Rho GTPases and their regulators. *Nat Rev Mol Cell Biol* **17**, 496-510, (2016).
109 Li, R. Cytokinesis in development and disease: variations on a common theme. *Cell Mol Life Sci* **64**, 3044-3058, (2007).
110 Wagner, E. & Glotzer, M. Local RhoA activation induces cytokinetic furrows independent of spindle position and cell cycle stage. *J Cell Biol* **213**, 641-649, (2016).
111 Liu, Z. & Weiner, O. D. Positioning the cleavage furrow: All you need is Rho. *J Cell Biol* **213**, 605-607, (2016).
112 Warmflash, A., Siggia, E. D. & Brivanlou, A. H. Signaling dynamics and embryonic development. *Cell Cycle* **11**, 3529-3530, (2012).
113 Lemmon, M. A. & Schlessinger, J. Cell signaling by receptor tyrosine kinases. *Cell* **141**, 1117-1134, (2010).
114 Bugaj, L. J. *et al.* Regulation of endogenous transmembrane receptors through optogenetic Cry2 clustering. *Nat Commun* **6**, 6898, (2015).
115 Ishimura, A. *et al.* Oncogenic Met receptor induces ectopic structures in Xenopus embryos. *Oncogene* **25**, 4286-4299, (2006).
116 Krishnamurthy, V. V. *et al.* Reversible optogenetic control of kinase activity during differentiation and embryonic development. *Development* **143**, 4085-4094, (2016).
117 Krishnamurthy, V. V. *et al.* Light-mediated Reversible Modulation of the Mitogen-activated Protein Kinase Pathway during Cell Differentiation and Xenopus Embryonic Development. *J Vis Exp*, (2017).
118 Johnson, H. E. *et al.* The Spatiotemporal Limits of Developmental Erk Signaling. *Dev Cell* **40**, 185-192, (2017).
119 Tanti, J. F. *et al.* Overexpression of a constitutively active form of phosphatidylinositol 3-kinase is sufficient to promote Glut 4 translocation in adipocytes. *J Biol Chem* **271**, 25227-25232, (1996).
120 Martin, S. S. *et al.* Activated phosphatidylinositol 3-kinase is sufficient to mediate actin rearrangement and GLUT4 translocation in 3T3-L1 adipocytes. *J Biol Chem* **271**, 17605-17608, (1996).
121 Manning, B. D. & Cantley, L. C. AKT/PKB signaling: navigating downstream. *Cell* **129**, 1261-1274, (2007).
122 Xu, Y., Nan, D., Fan, J., Bogan, J. S. & Toomre, D. Optogenetic activation reveals distinct roles of PIP3 and Akt in adipocyte insulin action. *J Cell Sci* **129**, 2085-2095, (2016).
123 Broichhagen, J. *et al.* Allosteric Optical Control of a Class B G-Protein-Coupled Receptor. *Angew Chem Int Ed Engl* **55**, 5865-5868, (2016).
124 Quintana, A. *et al.* Sustained activity of calcium release-activated calcium channels requires translocation of mitochondria to the plasma membrane. *J Biol Chem* **281**, 40302-40309, (2006).

125 Schwindling, C., Quintana, A., Krause, E. & Hoth, M. Mitochondria positioning controls local calcium influx in T cells. *J Immunol* **184**, 184-190, (2010).
126 Sadowski, L., Pilecka, I. & Miaczynska, M. Signaling from endosomes: location makes a difference. *Exp Cell Res* **315**, 1601-1609, (2009).
127 Hirokawa, N., Niwa, S. & Tanaka, Y. Molecular motors in neurons: transport mechanisms and roles in brain function, development, and disease. *Neuron* **68**, 610-638, (2010).
128 Mondal, P., Khamo, J. S., Krishnamurthy, V. V., Cai, Q. & Zhang, K. Drive the Car(go)s-New Modalities to Control Cargo Trafficking in Live Cells. *Front Mol Neurosci* **10**, 4, (2017).
129 van Bergeijk, P., Adrian, M., Hoogenraad, C. C. & Kapitein, L. C. Optogenetic control of organelle transport and positioning. *Nature* **518**, 111-114, (2015).
130 Duan, L. *et al.* Optogenetic control of molecular motors and organelle distributions in cells. *Chem Biol* **22**, 671-682, (2015).
131 Spiltoir, J. I., Strickland, D., Glotzer, M. & Tucker, C. L. Optical Control of Peroxisomal Trafficking. *ACS Synth Biol* **5**, 554-560, (2016).
132 Hughes, R. M. *et al.* Optogenetic apoptosis: light-triggered cell death. *Angew Chem Int Ed Engl* **54**, 12064-12068, (2015).
133 Dagliyan, O. *et al.* Engineering extrinsic disorder to control protein activity in living cells. *Science* **354**, 1441-1444, (2016).
134 Melero-Fernandez de Mera, R. M. *et al.* A simple optogenetic MAPK inhibitor design reveals resonance between transcription-regulating circuitry and temporally-encoded inputs. *Nat Commun* **8**, 15017, (2017).
135 Murakoshi, H. *et al.* Kinetics of Endogenous CaMKII Required for Synaptic Plasticity Revealed by Optogenetic Kinase Inhibitor. *Neuron* **94**, 690, (2017).
136 Wong, S., Mosabbir, A. A. & Truong, K. An Engineered Split Intein for Photoactivated Protein Trans-Splicing. *PLoS One* **10**, e0135965, (2015).
137 Shin, Y. *et al.* Spatiotemporal Control of Intracellular Phase Transitions Using Light-Activated optoDroplets. *Cell* **168**, 159-171 e114, (2017).
138 Komeili, A. & O'Shea, E. K. Nuclear transport and transcription. *Curr Opin Cell Biol* **12**, 355-360, (2000).
139 Beyer, H. M. *et al.* Red Light-Regulated Reversible Nuclear Localization of Proteins in Mammalian Cells and Zebrafish. *ACS Synth Biol* **4**, 951-958, (2015).
140 Niopek, D., Wehler, P., Roensch, J., Eils, R. & Di Ventura, B. Optogenetic control of nuclear protein export. *Nat Commun* **7**, 10624, (2016).
141 Yumerefendi, H. *et al.* Light-induced nuclear export reveals rapid dynamics of epigenetic modifications. *Nat Chem Biol* **12**, 399-401, (2016).
142 Boulina, M., Samarajeewa, H., Baker, J. D., Kim, M. D. & Chiba, A. Live imaging of multicolor-labeled cells in Drosophila. *Development* **140**, 1605-1613, (2013).
143 Schindler, S. E. *et al.* Photo-activatable Cre recombinase regulates gene expression in vivo. *Sci Rep* **5**, 13627, (2015).
144 Kawano, F., Okazaki, R., Yazawa, M. & Sato, M. A photoactivatable Cre-loxP recombination system for optogenetic genome engineering. *Nat Chem Biol* **12**, 1059-1064, (2016).
145 Nihongaki, Y., Yamamoto, S., Kawano, F., Suzuki, H. & Sato, M. CRISPR-Cas9-based photoactivatable transcription system. *Chem Biol* **22**, 169-174, (2015).

146 Polstein, L. R. & Gersbach, C. A. A light-inducible CRISPR-Cas9 system for control of endogenous gene activation. *Nat Chem Biol* **11**, 198-200, (2015).
147 Chan, Y. B., Alekseyenko, O. V. & Kravitz, E. A. Optogenetic Control of Gene Expression in Drosophila. *PLoS One* **10**, e0138181, (2015).
148 Reade, A. *et al.* TAEL: a zebrafish-optimized optogenetic gene expression system with fine spatial and temporal control. *Development* **144**, 345-355, (2017).
149 Konermann, S. *et al.* Optical control of mammalian endogenous transcription and epigenetic states. *Nature* **500**, 472-476, (2013).
150 Reis, S. A. *et al.* Light-controlled modulation of gene expression by chemical optoepigenetic probes. *Nat Chem Biol* **12**, 317-323, (2016).
151 Madsen, A. S. & Olsen, C. A. Optoepigenetics: An acetylation photoswitch. *Nat Chem Biol* **12**, 306-307, (2016).
152 Nihongaki, Y., Kawano, F., Nakajima, T. & Sato, M. Photoactivatable CRISPR-Cas9 for optogenetic genome editing. *Nat Biotechnol* **33**, 755-760, (2015).
153 Stolik, S., Delgado, J. A., Perez, A. & Anasagasti, L. Measurement of the penetration depths of red and near infrared light in human "ex vivo" tissues. *J Photochem Photobiol B* **57**, 90-93, (2000).
154 Montgomery, K. L. *et al.* Wirelessly powered, fully internal optogenetics for brain, spinal and peripheral circuits in mice. *Nat Methods* **12**, 969-974, (2015).
155 Ho, J. S. *et al.* Self-Tracking Energy Transfer for Neural Stimulation in Untethered Mice. *Phys Rev Appl* **4**, (2015).
156 Kim, T. I. *et al.* Injectable, cellular-scale optoelectronics with applications for wireless optogenetics. *Science* **340**, 211-216, (2013).
157 Park, S. I. *et al.* Soft, stretchable, fully implantable miniaturized optoelectronic systems for wireless optogenetics. *Nat Biotechnol* **33**, 1280-1286, (2015).
158 Jeong, J. W. *et al.* Wireless Optofluidic Systems for Programmable In Vivo Pharmacology and Optogenetics. *Cell* **162**, 662-674, (2015).
159 Steude, A., Witts, E. C., Miles, G. B. & Gather, M. C. Arrays of microscopic organic LEDs for high-resolution optogenetics. *Sci Adv* **2**, e1600061, (2016).
160 Huang, K., Dou, Q. Q. & Loh, X. J. Nanomaterial mediated optogenetics: opportunities and challenges. *Rsc Adv* **6**, 60896-60906, (2016).
161 Zhang, Y. *et al.* Illuminating Cell Signaling with Near-Infrared Light-Responsive Nanomaterials. *ACS Nano* **10**, 3881-3885, (2016).
162 Punjabi, A. *et al.* Amplifying the red-emission of upconverting nanoparticles for biocompatible clinically used prodrug-induced photodynamic therapy. *ACS Nano* **8**, 10621-10630, (2014).
163 Wu, X. *et al.* Dye-Sensitized Core/Active Shell Upconversion Nanoparticles for Optogenetics and Bioimaging Applications. *ACS Nano* **10**, 1060-1066, (2016).
164 Shah, S. *et al.* Hybrid upconversion nanomaterials for optogenetic neuronal control. *Nanoscale* **7**, 16571-16577, (2015).
165 Bansal, A., Liu, H., Jayakumar, M. K., Andersson-Engels, S. & Zhang, Y. Quasi-Continuous Wave Near-Infrared Excitation of Upconversion Nanoparticles for Optogenetic Manipulation of C. elegans. *Small* **12**, 1732-1743, (2016).
166 Pathak, G. P., Strickland, D., Vrana, J. D. & Tucker, C. L. Benchmarking of optical dimerizer systems. *ACS Synth Biol* **3**, 832-838, (2014).

167 Shao, J. *et al.* Smartphone-controlled optogenetically engineered cells enable semiautomatic glucose homeostasis in diabetic mice. *Sci Transl Med* **9**, (2017).
168 Chao, M. V. Neurotrophins and their receptors: a convergence point for many signalling pathways. *Nat Rev Neurosci* **4**, 299-309, (2003).
169 Widenfalk, J., Lundstromer, K., Jubran, M., Brene, S. & Olson, L. Neurotrophic factors and receptors in the immature and adult spinal cord after mechanical injury or kainic acid. *J Neurosci* **21**, 3457-3475, (2001).
170 Hirose, M., Kuroda, Y. & Murata, E. NGF/TrkA Signaling as a Therapeutic Target for Pain. *Pain Pract* **16**, 175-182, (2016).
171 Poo, M. M. Neurotrophins as synaptic modulators. *Nat Rev Neurosci* **2**, 24-32, (2001).
172 Huang, E. J. & Reichardt, L. F. Neurotrophins: roles in neuronal development and function. *Annu Rev Neurosci* **24**, 677-736, (2001).
173 Segal, R. A. Selectivity in neurotrophin signaling: theme and variations. *Annu Rev Neurosci* **26**, 299-330, (2003).
174 Deshmukh, M. & Johnson, E. M., Jr. Programmed cell death in neurons: focus on the pathway of nerve growth factor deprivation-induced death of sympathetic neurons. *Mol Pharmacol* **51**, 897-906, (1997).
175 Bothwell, M. Functional interactions of neurotrophins and neurotrophin receptors. *Annu Rev Neurosci* **18**, 223-253, (1995).
176 Barker, P. A. p75NTR: A study in contrasts. *Cell Death Differ* **5**, 346-356, (1998).
177 Dechant, G. & Barde, Y. A. The neurotrophin receptor p75(NTR): novel functions and implications for diseases of the nervous system. *Nat Neurosci* **5**, 1131-1136, (2002).
178 Lee, R., Kermani, P., Teng, K. K. & Hempstead, B. L. Regulation of cell survival by secreted proneurotrophins. *Science* **294**, 1945-1948, (2001).
179 Susen, K., Heumann, R. & Blochl, A. Nerve growth factor stimulates MAPK via the low affinity receptor p75(LNTR). *FEBS Lett* **463**, 231-234, (1999).
180 Lu, B., Pang, P. T. & Woo, N. H. The yin and yang of neurotrophin action. *Nat Rev Neurosci* **6**, 603-614, (2005).
181 Green, S. H., Rydel, R. E., Connolly, J. L. & Greene, L. A. PC12 cell mutants that possess low- but not high-affinity nerve growth factor receptors neither respond to nor internalize nerve growth factor. *J Cell Biol* **102**, 830-843, (1986).
182 Bassili, M., Birman, E., Schor, N. F. & Saragovi, H. U. Differential roles of Trk and p75 neurotrophin receptors in tumorigenesis and chemoresistance ex vivo and in vivo. *Cancer Chemother Pharmacol* **65**, 1047-1056, (2010).
183 Huang, C. S. *et al.* Nerve growth factor signaling in caveolae-like domains at the plasma membrane. *J Biol Chem* **274**, 36707-36714, (1999).
184 Lee, K. F. *et al.* Targeted mutation of the gene encoding the low affinity NGF receptor p75 leads to deficits in the peripheral sensory nervous system. *Cell* **69**, 737-749, (1992).
185 Liebl, D. J., Klesse, L. J., Tessarollo, L., Wohlman, T. & Parada, L. F. Loss of brain-derived neurotrophic factor-dependent neural crest-derived sensory neurons in neurotrophin-4 mutant mice. *Proc Natl Acad Sci U S A* **97**, 2297-2302, (2000).
186 Lomen-Hoerth, C. & Shooter, E. M. Widespread neurotrophin receptor expression in the immune system and other nonneuronal rat tissues. *J Neurochem* **64**, 1780-1789, (1995).
187 Passino, M. A., Adams, R. A., Sikorski, S. L. & Akassoglou, K. Regulation of hepatic stellate cell differentiation by the neurotrophin receptor p75NTR. *Science* **315**, 1853-1856, (2007).

188 Colombo, E. *et al.* Human neurotrophin receptor p75NTR defines differentiation-oriented skeletal muscle precursor cells: implications for muscle regeneration. *J Neuropathol Exp Neurol* **70**, 133-142, (2011).
189 Liu, Y. *et al.* Wortmannin, a widely used phosphoinositide 3-kinase inhibitor, also potently inhibits mammalian polo-like kinase. *Chem Biol* **12**, 99-107, (2005).
190 Arcaro, A. & Wymann, M. P. Wortmannin is a potent phosphatidylinositol 3-kinase inhibitor: the role of phosphatidylinositol 3,4,5-trisphosphate in neutrophil responses. *Biochem J* **296 (Pt 2)**, 297-301, (1993).
191 Martin, K. J., Shpiro, N., Traynor, R., Elliott, M. & Arthur, J. S. Comparison of the specificity of Trk inhibitors in recombinant and neuronal assays. *Neuropharmacology* **61**, 148-155, (2011).
192 Stephens, R. M. *et al.* Trk receptors use redundant signal transduction pathways involving SHC and PLC-gamma 1 to mediate NGF responses. *Neuron* **12**, 691-705, (1994).
193 Obermeier, A. *et al.* Neuronal differentiation signals are controlled by nerve growth factor receptor/Trk binding sites for SHC and PLC gamma. *EMBO J* **13**, 1585-1590, (1994).
194 Bae, S. S. *et al.* Src homology domains of phospholipase C gamma1 inhibit nerve growth factor-induced differentiation of PC12 cells. *J Neurochem* **71**, 178-185, (1998).
195 Tischer, D. & Weiner, O. D. Illuminating cell signalling with optogenetic tools. *Nat Rev Mol Cell Biol* **15**, 551-558, (2014).
196 Muller, K., Naumann, S., Weber, W. & Zurbriggen, M. D. Optogenetics for gene expression in mammalian cells. *Biol Chem* **396**, 145-152, (2015).
197 Tucker, C. L. Manipulating cellular processes using optical control of protein-protein interactions. *Prog Brain Res* **196**, 95-117, (2012).
198 Toettcher, J. E., Gong, D., Lim, W. A. & Weiner, O. D. Light control of plasma membrane recruitment using the Phy-PIF system. *Methods Enzymol* **497**, 409-423, (2011).
199 Zoltowski, B. D. & Gardner, K. H. Tripping the light fantastic: blue-light photoreceptors as examples of environmentally modulated protein-protein interactions. *Biochemistry* **50**, 4-16, (2011).
200 Khamo, J. S., Krishnamurthy, V. V., Sharum, S. R., Mondal, P. & Zhang, K. Applications of Optobiology in Intact Cells and Multicellular Organisms. *J Mol Biol* **429**, 2999-3017, (2017).
201 Chang, K. Y. *et al.* Light-inducible receptor tyrosine kinases that regulate neurotrophin signalling. *Nat Commun* **5**, 4057, (2014).
202 Covaceuszach, S. *et al.* The conundrum of the high-affinity NGF binding site formation unveiled? *Biophys J* **108**, 687-697, (2015).
203 Wehrman, T. *et al.* Structural and mechanistic insights into nerve growth factor interactions with the TrkA and p75 receptors. *Neuron* **53**, 25-38, (2007).
204 Hartman, D. S., McCormack, M., Schubenel, R. & Hertel, C. Multiple trkA proteins in PC12 cells bind NGF with a slow association rate. *J Biol Chem* **267**, 24516-24522, (1992).
205 Grimes, M. L. *et al.* Endocytosis of activated TrkA: evidence that nerve growth factor induces formation of signaling endosomes. *J Neurosci* **16**, 7950-7964, (1996).
206 Zhang, K. *et al.* Defective axonal transport of Rab7 GTPase results in dysregulated trophic signaling. *J Neurosci* **33**, 7451-7462, (2013).
207 Wang, L., Liang, Z. & Li, G. Rab22 controls NGF signaling and neurite outgrowth in PC12 cells. *Mol Biol Cell* **22**, 3853-3860, (2011).

208 Saka, Y., Hagemann, A. I., Piepenburg, O. & Smith, J. C. Nuclear accumulation of Smad complexes occurs only after the midblastula transition in Xenopus. *Development* **134**, 4209-4218, (2007).
209 Shyu, Y. J., Liu, H., Deng, X. & Hu, C. D. Identification of new fluorescent protein fragments for bimolecular fluorescence complementation analysis under physiological conditions. *Biotechniques* **40**, 61-66, (2006).
210 Jensen, E. C. Quantitative analysis of histological staining and fluorescence using ImageJ. *Anat Rec (Hoboken)* **296**, 378-381, (2013).
211 Zhou, X. X., Chung, H. K., Lam, A. J. & Lin, M. Z. Optical control of protein activity by fluorescent protein domains. *Science* **338**, 810-814, (2012).
212 Ueda, Y. *et al.* Protein kinase C activates the MEK-ERK pathway in a manner independent of Ras and dependent on Raf. *J Biol Chem* **271**, 23512-23519, (1996).
213 Mauro, A. *et al.* PKCalpha-mediated ERK, JNK and p38 activation regulates the myogenic program in human rhabdomyosarcoma cells. *J Cell Sci* **115**, 3587-3599, (2002).
214 Lee, D. *et al.* Temporally precise labeling and control of neuromodulatory circuits in the mammalian brain. *Nat Methods* **14**, 495-503, (2017).
215 Wang, W. *et al.* A light- and calcium-gated transcription factor for imaging and manipulating activated neurons. *Nat Biotechnol* **35**, 864-871, (2017).
216 Chen, S. *et al.* Near-infrared deep brain stimulation via upconversion nanoparticle-mediated optogenetics. *Science* **359**, 679-684, (2018).
217 Zhang, K. *et al.* Single-molecule imaging of NGF axonal transport in microfluidic devices. *Lab Chip* **10**, 2566-2573, (2010).
218 Watkins, L. P. & Yang, H. Detection of intensity change points in time-resolved single-molecule measurements. *J Phys Chem B* **109**, 617-628, (2005).
219 Montiel, D., Cang, H. & Yang, H. Quantitative characterization of changes in dynamical behavior for single-particle tracking studies. *J Phys Chem B* **110**, 19763-19770, (2006).
220 Khan, S. *et al.* Charge-Driven Fluorescence Blinking in Carbon Nanodots. *J Phys Chem Lett* **8**, 5751-5757, (2017).
221 Shimizu, K. T. *et al.* Blinking statistics in single semiconductor nanocrystal quantum dots. *Phys Rev B* **63**, (2001).
222 Frantsuzov, P., Kuno, M., Janko, B. & Marcus, R. A. Universal emission intermittency in quantum dots, nanorods and nanowires. *Nat Phys* **4**, 519-522, (2008).